AD-A174 140 POWER LINE NOISE MODELS AND ENERGY DETECTION IN THE HIGH FREQUENCY RADIO BAND(U) NAVAL POSTGRADUATE SCHOOL MONTEREY CA J M O'DWYER 20 JUN 86 NPS62-86-004 1/2

UNCLASSIFIED F/G 10/2 NL

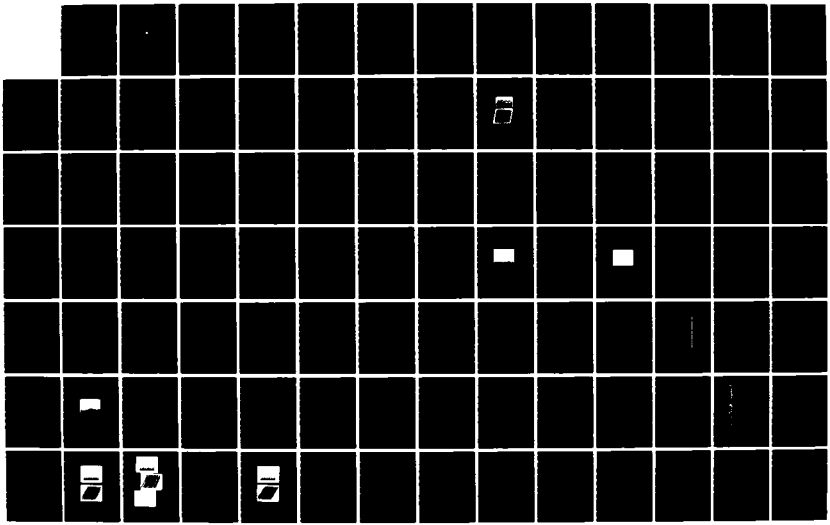

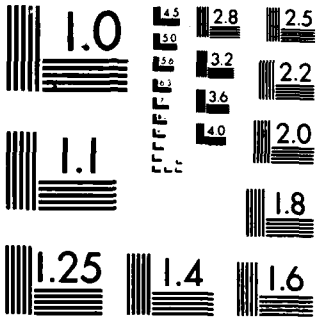

MICROCOPY RESOLUTION TEST CHART
NATIONAL BUREAU OF STANDARDS-1963-A

(2)

NPS62-86-004

AD-A174 140

NAVAL POSTGRADUATE SCHOOL

Monterey, California

DTIC
ELECTE
NOV 20 1986
S D
B

THESIS

POWER LINE NOISE MODELS AND
ENERGY DETECTION IN THE HIGH FREQUENCY
RADIO BAND

by

John Mark O'Dwyer

June 1986

Thesis Advisor: S. Jauregui

DTIC FILE COPY

Approved for public release; distribution is unlimited

Prepared for: Commander
Space and Naval Warfare Systems Command
Washington, D.C. 20363

86 11 19 008

NAVAL POSTGRADUATE SCHOOL
Monterey, CA 93943

Rear Admiral R. H. Shumaker
Superintendent

D. A. Schrady
Provost

This thesis is prepared in conjunction with research sponsored in part by Space and Naval Warfare Command under N0003985WRDJ539.

Reproduction of all or part of this report is authorized.

Released By:

David A. Schrady
Provost and Academic Dean

QUALITY INSPECTED 4

Accession For
NTIS
DTIC
Unannounced
Justification
By
Distribution
Availability Codes
Dist
A-1

SECURITY CLASSIFICATION OF THIS PAGE

REPORT DOCUMENTATION PAGE

1a. REPORT SECURITY CLASSIFICATION UNCLASSIFIED	1b. RESTRICTIVE MARKINGS
2a. SECURITY CLASSIFICATION AUTHORITY	3. DISTRIBUTION/AVAILABILITY OF REPORT Approved for public release; distribution is unlimited.
2b. DECLASSIFICATION/DOWNGRADING SCHEDULE	
4. PERFORMING ORGANIZATION REPORT NUMBER(S) NPS62-86-004	5. MONITORING ORGANIZATION REPORT NUMBER(S)
6a. NAME OF PERFORMING ORGANIZATION Naval Postgraduate School 6b. OFFICE SYMBOL (If applicable) 62	7a. NAME OF MONITORING ORGANIZATION Naval Postgraduate School
6c. ADDRESS (City, State, and ZIP Code) Monterey, California 93943-5000	7b. ADDRESS (City, State, and ZIP Code) Monterey, California 93943-5000
8a. NAME OF FUNDING/SPONSORING ORGANIZATION SPAWARSYSCOM 8b. OFFICE SYMBOL (If applicable)	9. PROCUREMENT INSTRUMENT IDENTIFICATION NUMBER N0003985WRDJ539
8c. ADDRESS (City, State, and ZIP Code) Washington, D.C. 20363	10. SOURCE OF FUNDING NUMBERS PROGRAM ELEMENT NO. / PROJECT NO. / TASK NO. / WORK UNIT ACCESSION NO.

11. TITLE (Include Security Classification)
POWER LINE NOISE MODELS AND ENERGY DETECTION IN THE HIGH FREQUENCY RADIO BAND

12. PERSONAL AUTHOR(S)
John Mark O'Dwyer

13a. TYPE OF REPORT	13b. TIME COVERED	14. DATE OF REPORT (Year, Month, Day)	15. PAGE COUNT
PhD Dissertation	FROM _____ TO _____	1986 June 20	169

16. SUPPLEMENTARY NOTATION

17. COSATI CODES			18. SUBJECT TERMS (Continue on reverse if necessary and identify by block number)
FIELD	GROUP	SUB-GROUP	Man-made Radio Noise; Power Line Noise; Radio Frequency Interference; Energy Detection Receiver; Gap Discharge; Corona Noise

19. ABSTRACT (Continue on reverse if necessary and identify by block number)

Electromagnetic interference from power lines is one of the main sources of man-made interference to communications in the high frequency (HF) radio band. Two types of radio interference generated by power lines are gap-type noise caused by electric discharges across line hardware and corona noise caused by the partial breakdown of the air due to the high electric fields around transmission line conductors. Using original data, this research has developed a parameter based model of gap-type and corona noise, that allows the fundamental noise mechanisms to be mathematically or physically simulated. An expression for the power spectral density (PSD) of gap-type noise and corona is derived. The energy detection problem is formulated,

20. DISTRIBUTION/AVAILABILITY OF ABSTRACT ☒ UNCLASSIFIED/UNLIMITED ☐ SAME AS RPT. ☐ DTIC USERS	21. ABSTRACT SECURITY CLASSIFICATION UNCLASSIFIED
22a. NAME OF RESPONSIBLE INDIVIDUAL Professor S. Jauregui	22b. TELEPHONE (Include Area Code) (408)646-2753 22c. OFFICE SYMBOL 62Ja

DD FORM 1473, 84 MAR — 83 APR edition may be used until exhausted. All other editions are obsolete.

SECURITY CLASSIFICATION OF THIS PAGE

and using analytical results based on the Hall model for radio noise, a robust energy detection receiver is developed. Tests of this receiver using actual and simultaed data are described.

Approved for public release; distribution is unlimited.

Power Line Noise Models and Energy Detection in the High Frequency Radio Band

by

John Mark O'Dwyer
Lieutenant, United States Navy
B.S.E.E., United States Naval Academy, 1978
M.S.E.E., Naval Postgraduate School, 1984

Submitted in partial fulfillment of the requirements for the degree of

DOCTOR OF PHILOSOPHY

from the

NAVAL POSTGRADUATE SCHOOL
June 1986

Author: John Mark O'Dwyer

Approved by:

P.H. Moose
Associate Professor of Electrical and Computer Engineering

G.A. Myers
Associate Professor of Electrical and Computer Engineering

R.H. Franke
Professor of Mathematics

M.J. Zyda
Assistant Professor of Computer Science

S. Jauregui
Adjunct Professor of Electrical and Computer Engineering
Dissertation Supervisor

Approved by: H.B. Rigas, Chairman, Department of Electrical and Computer Engineering

Approved by: David A. Schrady, Academic Dean

ABSTRACT

Electromagnetic interference from power lines is one of the main sources of man-made interference to communications in the high frequency (HF) radio band. Two types of radio interference generated by power lines are gap-type noise caused by electric discharges across line hardware and corona noise caused by the partial breakdown of the air due to the high electric fields around transmission line conductors. Using original data, this research has developed a parameter based model of gap-type and corona noise that allows the fundamental noise mechanisms to be mathematically or physically simulated. An expression for the power spectral density (PSD) of gap-type noise and corona is derived. The energy detection problem is formulated, and using analytical results based on the Hall model for radio noise, a robust energy detection receiver is developed. Tests of this receiver using actual and simulated data are described.

TABLE OF CONTENTS

I. INTRODUCTION ---------- 8

A. PURPOSE ---------- 8

B. BACKGROUND ---------- 8

C. CONTENT ---------- 10

II. IMPULSIVE NOISE ---------- 12

A. INTRODUCTION ---------- 12

B. GENERALIZED SCENARIO ---------- 12

C. EMPIRICAL MODELS ---------- 23

D. FILTERED IMPULSE NOISE MODELS ---------- 31

E. HALL MODEL EXTENSIONS ---------- 36

F. SUMMARY ---------- 42

III. GAP NOISE MODEL ---------- 44

A. INTRODUCTION ---------- 44

B. GAP NOISE MECHANISM ---------- 44

C. OBSERVED TIME-DOMAIN CHARACTERISTICS ------- 46

D. MODEL DEVELOPMENT ---------- 58

E. COMPARISON OF CALCULATED AND OBSERVED DATA - 65

F. SUMMARY ---------- 73

IV. CORONA NOISE MODEL ---------- 75

A. INTRODUCTION ---------- 75

B. CORONA NOISE THEORY ---------- 75

C. TIME DOMAIN CHARACTERISTICS ---------- 77

D. CORONA NOISE MODEL ---------- 84

E. PARAMETER ESTIMATION ---------- 92

F. SUMMARY ---------- 95

V. ENERGY DETECTION RECEIVERS ---------- 98

A. INTRODUCTION ---------- 98

B. ENERGY DETECTION ---------- 98

C. SQUARE AND SUM RECEIVER ---------- 101

D. LOCALLY OPTIMUM RECEIVER ---------- 106

E. ADAPTIVE LIMITER ---------- 116

F. SUMMARY ---------- 126

VI. CONCLUSION ---------- 128

A. RESULTS ---------- 128

B. FURTHER RESEARCH ---------- 129

APPENDIX A: INSTRUMENTATION ---------- 131

APPENDIX B: FILTERED IMPULSE PROCESS ---------- 135

APPENDIX C: SIGNAL PLUS NOISE DENSITY ---------- 138

APPENDIX D: SPECTRUM OF A RENEWAL PROCESS ---------- 141

APPENDIX E: SPECTRUM OF A BRANCHING RENEWAL PROCESS --- 146

APPENDIX F: NON-HOMOGENEOUS POISSON PROCESS ---------- 151

APPENDIX G: AUTOCORRELATION OF CORONA NOISE ---------- 154

APPENDIX H: LOCALLY OPTIMUM ENERGY RECEIVER ---------- 158

LIST OF REFERENCES ---------- 161

INITIAL DISTRIBUTION LIST ---------- 166

ACKNOWLEDGEMENT

I owe a great debt to Dr. Stephen Jauregui. Without his constant encouragement and support this work would not have been completed. I would like to take this opportunity to thank him.

I would also like to thank the members of my Doctoral Committee. In particular, I wish to express my gratitude to Professor P.H. Moose who spent many hours reviewing the initial results and suggesting profitable avenues of inquiry, and to Professor Myers and Professor Franke for their careful reading of this dissertation.

Professor W. Ray Vincent also contributed substantially to this work. Working with him in instrumenting the experiments was an education in its own right. His experience and insight into to practical aspects of communications engineering added much to my understanding of the subject.

Finally, I must thank my wife, Sally, without whose support and encouragement this thesis would not have been possible.

I. INTRODUCTION

A. PURPOSE

Observations of radio interference at high frequency (HF) receiver sites have indicated that existing models of man-made radio noise are inadequate to describe the observed time- and frequency-domain behavior of the noise. The data also shows that quite often a specific noise source predominates in a particular location. These observations led to the objectives of this dissertation:

1. to develop specific models for certain man-made noise sources in the HF radio band and
2. to apply this model to the analysis of energy detection receivers.

B. BACKGROUND

Studies conducted over the past few years have indicated that one of the primary sources of man-made radio noise in the HF band are alternating current (AC) transmission and distribution lines [Refs. 1,2]. Two of the primary sources of power line noise are gap noise, also known as micro-sparking, and corona. Gap noise is caused by a sparking process between hardware points on utility poles and corona is caused by the partial breakdown of air due to high electric fields around high voltage conductors. Both of these noise types are non-Gaussian noise processes.

The majority of the models of man-made and atmospheric noise to date have assumed the high amplitude impulses driving the receiver have either a Poisson arrival rate or a variation of Poisson arrivals. This assumption has allowed the derivation of first order envelope statistics: the amplitude probability distribution (APD) function and the density function of the phase of received noise for various amplitude distributions of the driving impulses. Observations of man-made noise from power lines, however, has indicated that the assumption of interpulse independence (Poisson arrival times) is not valid. There exists a definite time domain correlation of the impulses driving the receiver. This is due to the underlying deterministic mechanism of the fundamental frequency of the power line voltage. Consequently, this research has concentrated on the statistics of the impulse arrivals which are manifest in the autocorrelation function and the spectrum of the observed noise process. Accordingly, the models developed are specific rather than general and are more suited to source identification by spectrum analysis and robustness evaluation of systems rather than to generic specification of optimum receiver structures.

The performance of energy detection receivers for stochastic signals in non-Gaussian noise has received relatively little study. Actual implementation of algorithms for signal detection has been based on heuristics.

The advent of digital signal processing techniques that allow for complex post-detection algorithms suggests a careful, statistical analysis of the noise performance of these systems may help develop more efficient and robust receivers.

C. CONTENT

A brief outline of the rest of the thesis will now be presented. Chapter II develops a general model for bandpass impulsive phenomena using a filtered impulse model and complex envelope theory. Well known empirical models and physical models of radio noise are presented and their relationship to the generalized model discussed. Particular attention is paid to the Hall model for atmospheric radio noise [Ref. 3]. Some useful extensions to it are derived that will be used for simulations in Chapter V.

In Chapter III, field observations from sources of gap noise interference are presented and analyzed. Three cases of actual interference are used and a probabilistic model based on a statistical analysis of the data and the filtered impulse model developed in Chapter II is specified. The power spectral density (PSD) of gap type noise as predicted by the model is derived and compared to the data.

Using an actual case of corona noise from a 500 kV power line, the same type of analysis is carried out for corona noise. The corona noise model is based on the same filtered

impulse framework as the gap noise model of Chapter III however, the specifications differ substantially.

Using the Hall model for atmospheric noise discussed in Chapter II, a locally optimum receiver for detection of unknown signals in HF atmospheric noise is derived. A practical modification to this receiver shows it to be an adaptive limiter. The performance of this receiver is then examined in simulated man-made noise and in recorded HF signal and noise data.

Appendix A presents a brief description of the instrumentation that was used to collect much of the data for this thesis. The dissertation concludes with a brief summary of results and some suggestions for future research.

II. IMPULSIVE NOISE AND RECEIVER MODEL

A. INTRODUCTION

In this chapter a general set of specifications for an impulsive noise interference process will be developed and the results of previous work in the field explained in terms of the specifications. This generalized scenario will be used in later chapters to specify complicated sources of man-made radio interference. In attempting to describe atmospheric radio noise, two general types of models have been developed: empirical models designed to fit first order statistical data, and physical models directly related to the underlying physical mechanisms. The Hall empirical model for atmospheric radio noise has been shown to fit atmospheric noise data very well and will be used in this dissertation. Some extensions to the Hall model will be developed in this chapter.

B. GENERALIZED SCENARIO

In order to provide a framework for the discussion of the impulsive noise models, a general interference scenario for impulsive noise will be described [Ref. 4,5]. A typical interference scenario consists of the following elements:

1. a source of interference,
2. a transmission medium to the receiver and

3. the receiver where the interference manifests itself.

For this study the noise process at the receiver is modeled as the sum of a high density (in time), low amplitude Gaussian component and a low density, high amplitude impulsive term.

These elements are shown below, where $e'(t)$ in Fig. 1 is the impulsive interference, $L'(\omega)$ is the frequency response of the transmission medium, $z'(t)$ is white Gaussian noise and $H'(\omega)$ is the combined response of the RF and IF filters of the receiver.

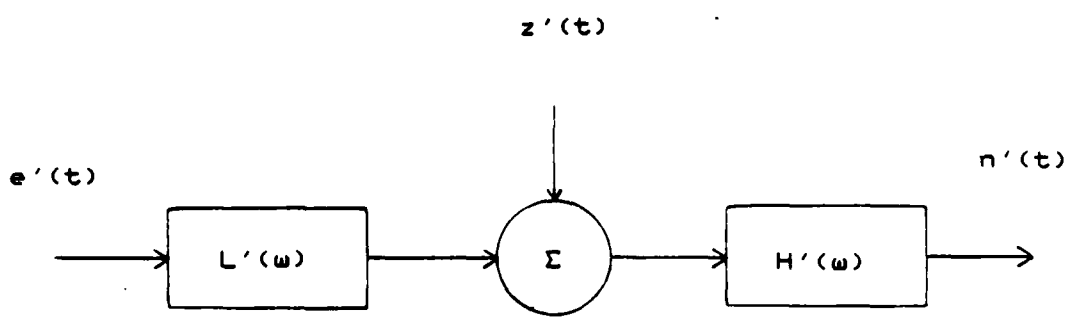

Figure 1. Interference Scenario

The source of impulsive noise is specified by the equation

$$e'(t) = \sum_{i=1}^{N(t)} e_i \delta(t-t_i) \qquad (2\text{-}1)$$

where e_i is the real amplitude of the ith pulse and N(t) is a unit counting process that generates arrival times, the t_i's. Using this representation, the impulsive interference source is described by the probability density function (PDF) of each e_i, given by $p_i(e)$, and the impulse arrival times generated by the unit counting process, N(t).

In order to simplify later analysis the interference scenario will be expressed in terms of its complex envelope. The interference process at the receiver detector is n'(t) and will be replaced by its complex envelope equivalent, n(t), where

$$n'(t) = \mathrm{Re}[n(t)e^{j\omega_0 t}] \qquad (2\text{-}2)$$

and

$$n(t) = n_c(t) + jn_s(t). \qquad (2\text{-}3)$$

The term $n(t)e^{j\omega_0 t}$ is known as the analytic signal representation of n'(t), and n(t) is the complex envelope representation of n'(t). The reference frequency for the complex envelope representation is ω_0. When n'(t) is a bandpass process, $n_c(t)$ and $n_s(t)$ are the lowpass inphase and quadrature modulation components of n(t) respectively.[Ref. 6:p. 75]

Specifying a filtered impulse model in complex envelope form requires deriving an expression for the driving impulse function given in Eqn. 2-1. Two equivalent approaches may be taken and they are both outlined below. In the first approach a bandpass impulse may be postulated where the spectrum of the impulse is assumed flat from $\omega_0 - W$ to $\omega_0 + W$ where ω_0 is the reference frequency and W is an arbitrary bandwidth. For this case the analytic signal representation is easily found in the frequency domain. Using the frequency domain definition, the analytic signal associated with $e'(t)$ in Eqn. 2-1 is

$$e_A(t) = (1/\pi)\int_0^\infty E'(\omega)e^{j\omega t}\,d\omega. \qquad (2\text{-}4)$$

Inserting the definition of the bandpass impulse defined above and using Eqn. 2-1

$$e_A(t) = \sum_{i=1}^{N(t)} (2/\pi)\, e^{j\omega_0(t-t_i)} \sin(W(t-t_i))/(t-t_i). \qquad (2\text{-}5)$$

The complex envelope of $e'(t)$ is defined as

$$e(t) = e_A(t)e^{-j\omega_0 t} \qquad (2\text{-}6)$$

and

$$e(t) = \sum_{i=1}^{N(t)} (2/\pi)\, e^{-j\theta_i} \sin(W(t-t_i))/(t-t_i) \qquad (2\text{-}7)$$

where $\omega_0 t_i = \theta_i$. As W becomes large, e(t) will asymptotically approach [Ref. 7]

$$e(t) = \sum_{i=1}^{N(t)} 2e^{-j\theta_i} \delta(t-t_i). \qquad (2\text{-}8)$$

The second approach [Ref. 8] is to consider the impulse as ideal and constant in the frequency domain. The analytic signal representation of $e'(t)$ is then directly determined from the time domain definition of an analytic signal. The analytic signal is defined as

$$e_A(t) = e'(t) + j\hat{e}'(t) \qquad (2\text{-}9)$$

where $\hat{e}'(t)$ is the Hilbert transform of $e'(t)$. The analytic signal representation of Eqn. 2-1 using the above definitions is

$$e_A(t) = \sum_{i=1}^{N(t)} \delta(t-t_i) + j/(\pi(t-t_i)) \qquad (2\text{-}10)$$

since $1/\pi t$ is the Hilbert transform of the delta function. The complex envelope of $e'(t)$ is then

$$e(t) = \sum_{i=1}^{N(t)} \delta(t-t_i)e^{-j\theta_i} + je^{-j\omega_0 t}/(\pi(t-t_i)) \qquad (2\text{-}11)$$

using Eqn. 2-6.

Although apparently different, when the complex impulse trains described by Eqns. 2-8 and 2-11 are convolved with a complex filter impulse response, the filter output is identical for both representations. If $h(t)$ is the complex envelope of the filter impulse response, then the filter output with the input given by Eqn. 2-8 is

$$\sum_{i=1}^{N(t)} e^{-j\theta_i} h(t-t_i) \tag{2-12}$$

where complex convolution is defined as

$$h(t) * e(t) = (1/2)\int_{-\infty}^{\infty} h(\tau)e(t-\tau)d\tau. \tag{2-13}$$

The filter output with the input defined by Eqn. 2-11 is

$$(1/2)\sum_{i=1}^{N(t)} h(t-t_i)e^{-j\theta_i} + je^{-j\omega_0 t} h_h(t-t_i) \tag{2-14}$$

where the convolution definition of the Hilbert transform was used [Ref. 6:p. 69]. Using Eqn. 2-6, the same result as derived in Eqn. 2-12 is then found. Due to its simplicity and for ease of use in programming simulations, Eqn. 2-8 will be used to represent the driving impulse function for the rest of this dissertation.

One further point to mention concerns the probability distribution of θ_i in Eqn. 2-8. For the processes we consider, t_i will have random arrival times and, as can be seen in Eqn. 2-7, θ_i is formed by multiplying t_i times the reference frequency, ω_0. Consequently, θ_i is the phase of the impulse time with respect to the reference frequency. It can be assumed to be uniformly distributed over 0 to 2π when the t_i's have a probabilistic interarrival distribution and ω_0 is much greater than the inverse of the interarrival times [Ref. 9: pp. 279, 10].

In an actual interference situation the received impulses are filtered by the radiating antenna, spreading losses, atmospheric attenuation, receiving antenna and cabling losses. These terms will be lumped together as an equivalent filter, $L'(\omega)$. Examples of this filtering term for various interference sources have been recorded by many researchers [Ref. 11,12]. The filter characteristic is specified in the frequency domain as $L'(\omega)$ since that is where it is most easily observed.

An example of this type of filtering is shown in Fig. 2 where the frequency spectrum of an impulsive noise source due to a gap discharge is shown from 0 to 200 MHz. The straight lines in the 3-Axis view are due to stations in the high frequency (HF) band from 2 to 30 MHz and the FM band from 88 to 106 MHz. The continuous envelope seen in the upper view is the magnitude of the frequency response of $L'(\omega)$. The solid line in the upper picture is the noise floor of the spectrum analyzer at -100 dBm.

The complex envelope of the impulse response of the attenuation term, $L'(\omega)$, is given in the frequency domain by

$$L(\omega) = L_p[L'(-\omega-\omega_0) + L'^*(\omega+\omega_0] \qquad (2\text{-}15)$$

where L_p denotes the lowpass part of the quantity in brackets.

A complex Gaussian component $z(t)$ will also exist in the observed noise process and is due to the combination of:

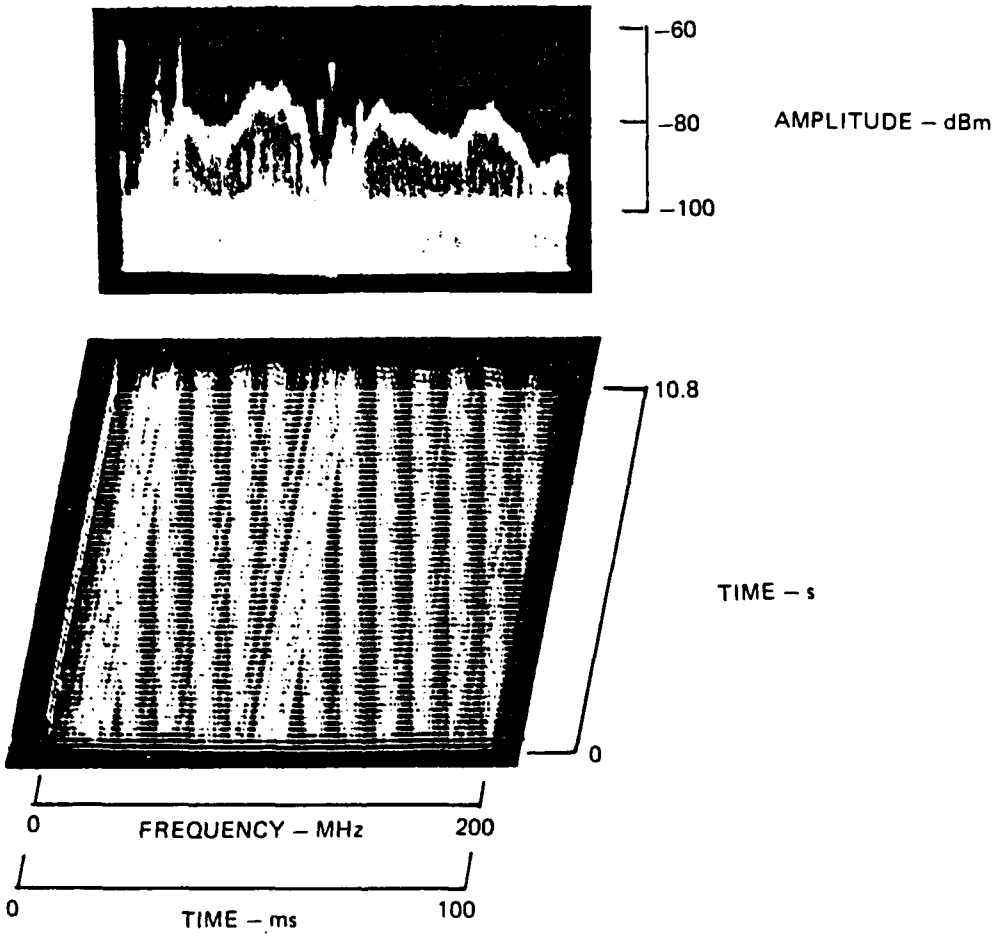

Figure 2. Gap Discharge in Frequency Domain

1. the thermal noise in the receiver, and

2. the combined sum of many low level atmospheric or man-made impulsive sources.

This term will be modeled by independent zero mean Gaussian noise processes for the inphase and quadrature terms with a power spectral density (PSD) in each component of $N_0/2$. The distinction between the Gaussian noise term and impulsive noise term is that many receiver responses overlap for the high density, low amplitude Gaussian case, satisfying the condition for the Central Limit Theorem. For the impulsive noise the receiver response to each impulse is discernible such that the probability of more than one or two pulses overlapping is negligible. Common sources of impulsive noise are man-made noise due to power lines and atmospheric noise due to lightning.

The time domain input to the receiver is now modeled by the expression

$$n(t) = (h(t)/2) * [z(t) + \sum_{i=1}^{N(t)} 2e_i e^{-j\theta_i} \int_{-\infty}^{\infty} e^{j\omega(t-t_i)} L(\omega)d\omega] \qquad (2\text{-}16)$$

where

$$h(t) = h_c(t) + jh_s(t).$$

The noise power bandwidth of $H(\omega)$ will be designated B_{eff}. In most situations $L'(\omega)$ will effectively be constant in comparison to the narrowband receiver filter $H(\omega)$. This makes $L(\omega)$ a constant that depends only on ω_0. Additionally, $g(t)$ will be defined by

$$g(t) = (h(t/2)) * z(t) \tag{2-17}$$

and is the low level Gaussian noise at the detector. The power in the inphase and quadrature components of the Gaussian noise will be $N_0 B_{eff}/2$. The complex lowpass noise process can now be written as

$$n(t) = g(t) + \sum_{i=1}^{N(t)} a_i e^{-j\theta_i} h(t-t_i) \tag{2-18}$$

where

$$a_i = e_i L'(\omega_0). \tag{2-19}$$

The parameter a_i is then a scenario dependent parameter that is a function of the reference frequency and the impulse amplitude. With the above simplifications, Fig. 1 can now be expressed in complex envelope form as shown in Fig. 3.

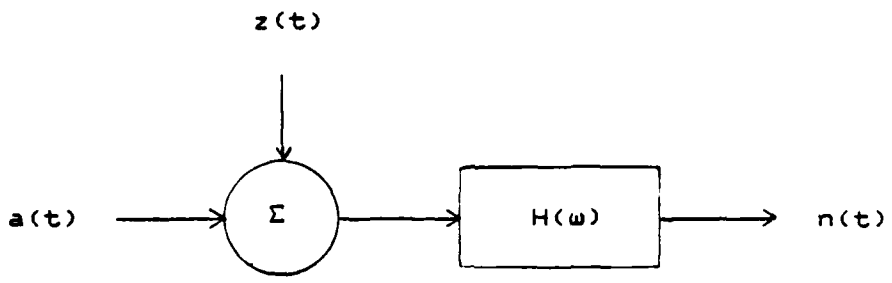

Figure 3. Complex Envelope of Interference Scenario

The terms from Fig. 1 have been replaced by their equivalent complex envelope representations and the prime is dropped to indicate this.

Some further simplifications will now be considered based on the characteristics of the $H'(\omega)$, the bandpass filter. If the impulse response $h(t)$ of the filter is real, $H'(\omega)$ has conjugate symmetry about the origin in the sense that $H'^{*}(\omega) = H'(-\omega)$. Furthermore, if $H'(\omega)$ is sym-metrical in the same way about the reference frequency, ω_0, then $h_s(t)$ will equal 0.

The envelope squared of the process defined in Eqn. 2-18 is

$$E^2(t) = n_c^2(t) + n_s^2(t). \qquad (2\text{-}20)$$

If the Gaussian noise term is assumed to equal 0 then

$$E^2(t) = \sum_{i=1}^{N(T)} \sum_{j=1}^{N(T)} a_i a_j h_c(t-t_i) h_c(t-t_j) \cos(\theta_i - \theta_j) +$$

$$\sum_{i=1}^{N(T)} \sum_{j=1}^{N(T)} a_i a_j h_s(t-t_i) h_s(t-t_j) \cos(\theta_i - \theta_j). \qquad (2\text{-}21)$$

If $N(T)$ defines a low density counting process such that there is negligible overlap between subsequent pulses and $h(t)$ is the complex envelope of the impulse response of a bandpass symmetrical filter, then the envelope of $n(t)$ can be simply written as

$$E(t) = \sum_{i=1}^{N(t)} a_i h(t-t_i) \qquad (2\text{-}22)$$

where $h(t)$ is equal to $h_c(t)$.

At this point of the analysis two avenues may be pursued. If there is a time dependency between pulses (non-

exponentially distributed interarrival times), then the correlation function and spectrum of the process can be examined. If the amplitude probability distribution (APD) of the envelope is the desired result, then the characteristic function of the envelope is most useful. The APD function is commonly used in radio noise research and is equal to one minus the cumulative distribution function (CDF). In general these two approaches are mutually exclusive since the assumption of time dependency between the pulses makes the envelope APD function difficult to calculate. If the impulse arrival times form a Poisson point process then the envelope APD may be calculated: however, the spectrum is constant. The remainder of this chapter will follow the envelope APD approach. Results obtained by previous researchers will be developed using the general noise model. Chapters III and IV will explain the other avenue and look at the spectrum of complicated man-made noise processes.

C. EMPIRICAL MODELS

Empirical models of atmospheric noise have been developed to provide a mathematical expression for the first-order statistics of the envelope of the received waveform. In particular, the APD has been emphasized. This type of model attempts to construct a mathematical expression that fits observed data without regard for the physics

of the interference scenario. Empirical models have the advantage that the resulting expressions are much simpler than those obtained from the filtered impulse models. One disadvantage of this class of model is that since only the first order statistics of the noise are considered in developing and fitting the model, the higher order statistics may not match the data well.

Variations of the Rayleigh distribution have been proposed by a number of authors to fit observed atmospheric noise data. The Rayleigh PDF is

$$p(r) = 2\alpha r e^{-\alpha r^2} \qquad r \geq 0 \qquad (2\text{-}23)$$
$$= 0 \qquad r < 0$$

and the APD or exceedance probability

$$Pr(r > r_o) = 1 - P(r_o) = e^{-\alpha r_o^2} \qquad r_o \geq 0 \qquad (2\text{-}24)$$
$$= 1 \qquad r_o < 0$$

How well the single parameter Rayleigh distribution fits observed atmospheric noise data can be seen in Fig. 4. The data points are exceedance probabilities plotted in decibels (dB) above the root-mean-squared (RMS) value of the received envelope. The data was measured on an ARN-2 receiver at a center frequency of 10 MHz at Boulder, Colorado [Ref. 13]. The high probability, low amplitude portions of the observed data approaches the slope of the Rayleigh distribution curve for α equal to 12. (α is defined in Eqn. 2-24) This value

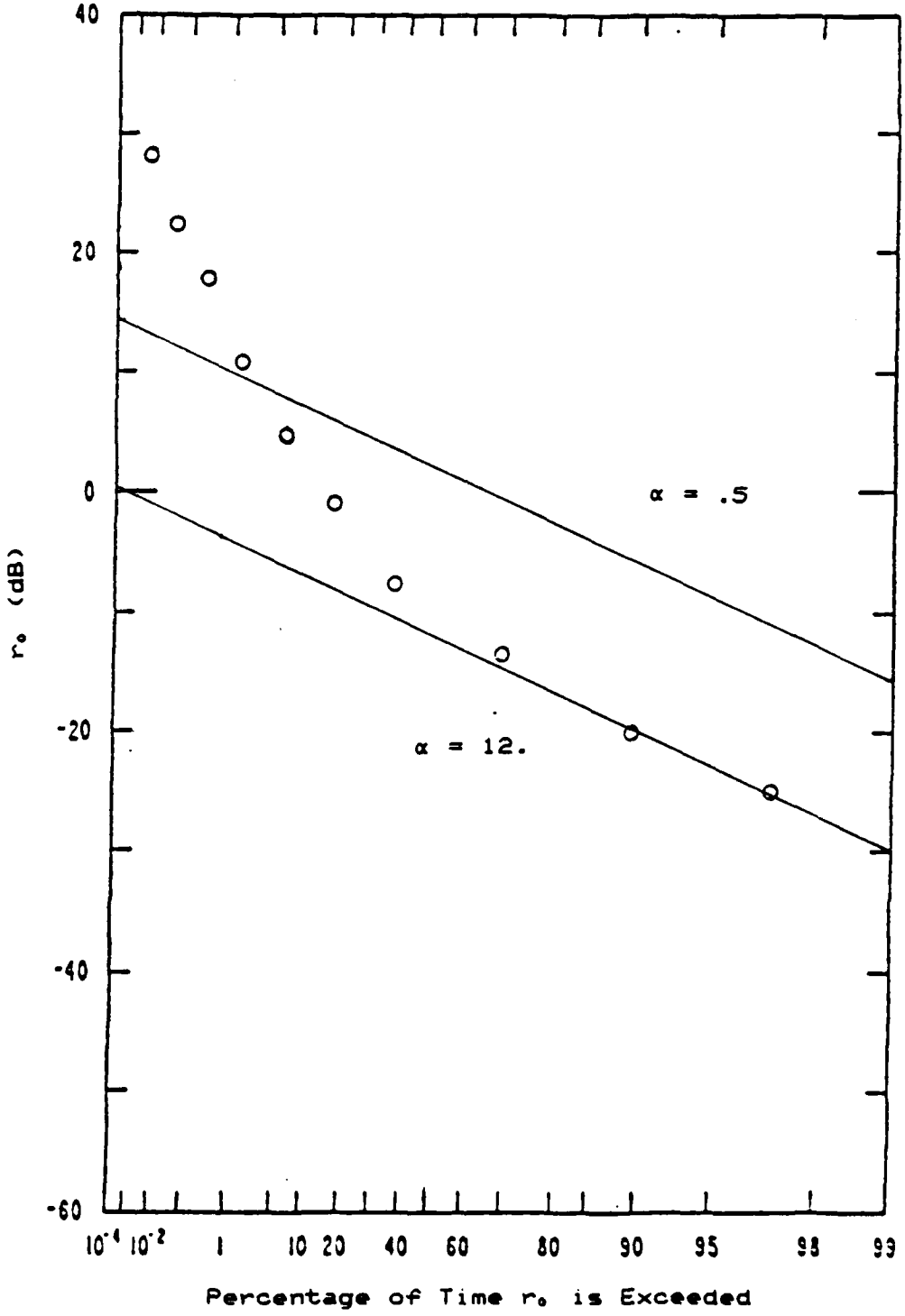

Figure 4. Atmospheric Noise and Rayleigh Distribution

of α was chosen to fit the high probability portion of the data. That the data approaches a Rayleigh distribution is due to the effect of the many small overlapping impulses occurring at low amplitudes whose quadrature Gaussian components will have a Rayleigh envelope. However, at the low probability, high amplitude part of the curve the Rayleigh distribution predicts far fewer values than actually occur. This is the distinguishing factor of the envelope distribution of impulsive noise: that its distribution contains a higher probability of high amplitude terms than is predicted by the Rayleigh distribution. The second curve in Fig. 4 where α is equal to .5 is the Rayleigh distribution with the same power as the observed data. It can be seen that this curve under estimates the high amplitude and over estimates the low amplitude values of the observed distribution. It should be noted that this type of plot emphasizes the low probability portion of distribution since that is where the deviation from the expected behavior occurs.

In an attempt to correct the poor fit of the Rayleigh distribution at high amplitude levels, Likhter [Ref. 14] proposed a combination of two Rayleigh distributions:

$$Pr(r > r_o) = (1 - c)e^{-\alpha r_o^2} + ce^{-\beta r_o^2} . \qquad (2\text{-}25)$$

This formula has been shown to agree poorly with practical results [Ref. 15].

Spaulding, Roubique and Crichlow [Ref. 16] combined the Rayleigh distribution with a "power" Rayleigh distribution to obtain a distribution that fit very well for atmospheric noise over a wide range of receiver bandwidths. This APD is

$$Pr(r > r_o) = e^{-\alpha r_o^2} \qquad r_o < \beta$$

$$Pr(r > r_o) = e^{-(\alpha r_o^2)^{1/s}} \qquad r_o \geq \beta \qquad (2\text{-}26)$$

where α, β and s are determined from measured statistical parameters of the noise.

Horner and Harwood [Ref. 17] proposed the two parameter log-normal distribution and found it gave a satisfactory fit to radio noise data in the VLF band. The log-normal was chosen since it has a more impulsive tail and fits the high amplitude, low probability data better than the Rayleigh distribution. The PDF for the log-normal distribution is

$$p(r) = \frac{1}{r\sigma(2\pi)^{1/2}} e^{-(\ln(r) - \alpha)^2/2\sigma^2} \qquad (2\text{-}27)$$

Two examples of the APD of the log-normal distribution are shown in Fig. 5 where the curve with α equal to -.24 and σ^2 equal to .24 is the log-normal distribution with the same mean and mean square parameters as the curve with α equal to .5 in Fig. 4. Comparing the two curves the log-normal distribution provides an intrinsically better fit to

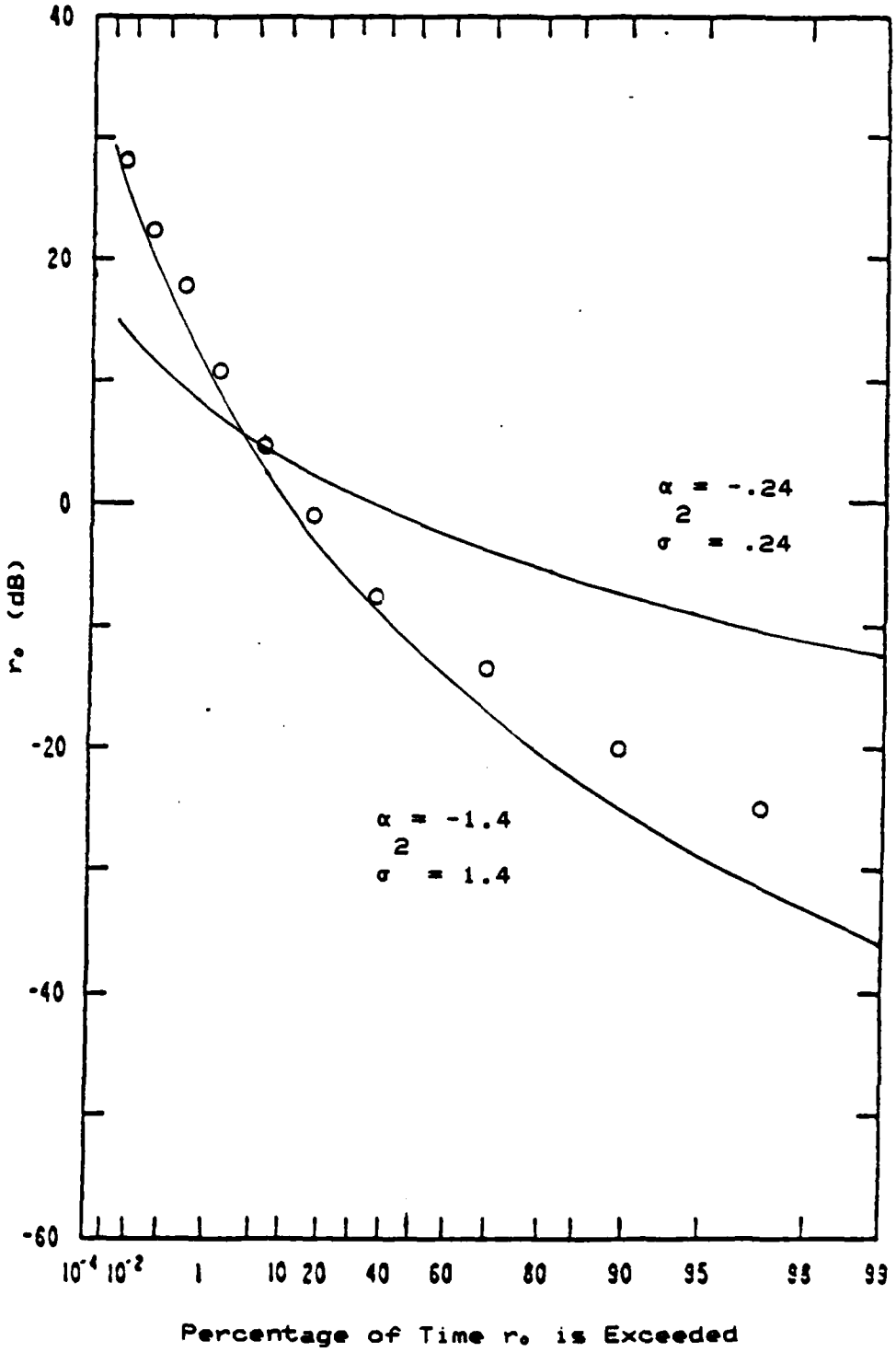

Figure 5. Atmospheric Noise and Log-Normal Distribution

impulsive noise data at both the high and low amplitude values. When the log-normal density has both parameters chosen to match the mean and mean square values of the observed data an excellent fit to this particular data is obtained. This is seen in the curve with α equal to -1.4 and σ^2 equal to 1.4.

Another model that has been successfully used to fit the observed APD of atmospheric radio noise is Hall's generalized "t" distribution [Ref. 3]. This model is unique in that it is not of the filtered impulse type; however, in contrast to the strictly empirical models it does postulate a random process.

One of the problems of Gaussian models of atmospheric noise is that the dynamic range of the model is less than the observed dynamic range of the noise. To achieve a greater dynamic range starting with a Gaussian process, Hall proposed a model which considered the received noise to be of the form

$$n(t) = a(t)s(t) \tag{2-28}$$

where a(t) is a slowly varying stationary random process and s(t) is an independent, narrowband Gaussian process. An analytically tractable distribution was selected for a(t) which was chosen to give good agreement between the model and measured atmospheric noise data. The distribution for a(t) is:

$$p(a) = \frac{(m/2)^m}{\sigma^m \Gamma(m/2)} \frac{1}{|a|^{m+1}} e^{-(m/2a^2\sigma^2)} \tag{2-29}$$

where m and σ are the two parameters used to fit the model to the data. The distribution of $s(t)$ is Gaussian;

$$p(s) = \frac{1}{(2\pi\sigma_1^2)^{1/2}} e^{-(s^2/2\sigma_1^2)} . \tag{2-30}$$

Hall calculated the density function of $n(t)$ to be

$$p(n) = \frac{\Gamma(\theta/2)}{\Gamma((\theta-1)/2)} \frac{\gamma^{\theta-1}}{\pi^{1/2}} \frac{1}{(n^2 + \gamma^2)^{\theta/2}} \tag{2-31}$$

where

$$\gamma = m^{1/2} (\sigma_1/\sigma),$$

$$\theta = m = 1,$$

and Γ is the gamma function. For the case where $\sigma_1 = \sigma$, Eqn. 2-31 is the density function for Student's "t" distribution which is the basis for describing the density as a generalized "t" distribution.

Hall then calculated the envelope distribution for $n(t)$ based on the above assumptions and obtained

$$p(r) = (\theta - 1) \gamma^{\theta-1} \frac{r}{(r^2 + \gamma^2)^{((\theta+1)/2)}} \tag{2-32}$$

with the phase uniformly distributed between 0 and 2π.

For atmospheric radio noise, values of θ in the range 2 to 5 have been found to give excellent agreement with the data [Ref. 18,19]. (Models with integer values of the parameter θ will be abbreviated to Hall2, Hall3, etc.)

Fig. 6 shows the Hall3 fit to the same atmospheric noise data used in Figs. 3 and 4. An excellent fit to this data is obtained. The Hall model has some disadvantages. The higher moments only exist for orders greater than $\theta-1$ and the parameters θ and γ must be determined for each interference scenario and are not easily related to the physical source of the interference.

D. FILTERED IMPULSE NOISE MODELS

The filtered impulse models differ fundamentally in concept from the empirical models described previously. This class of model will be explained in terms of the generalized interference scenario presented at the beginning of the chapter. The filtered impulse models have the advantage of being based on the underlying physics of the process but suffer from the disadvantage of being analytically complex. Interestingly, some of the results obtained from the filtered impulse models have retroactively justified the expressions that were derived from the empirical models.

To determine the APD of the envelope of a filtered impulse process, the joint characteristic function of the

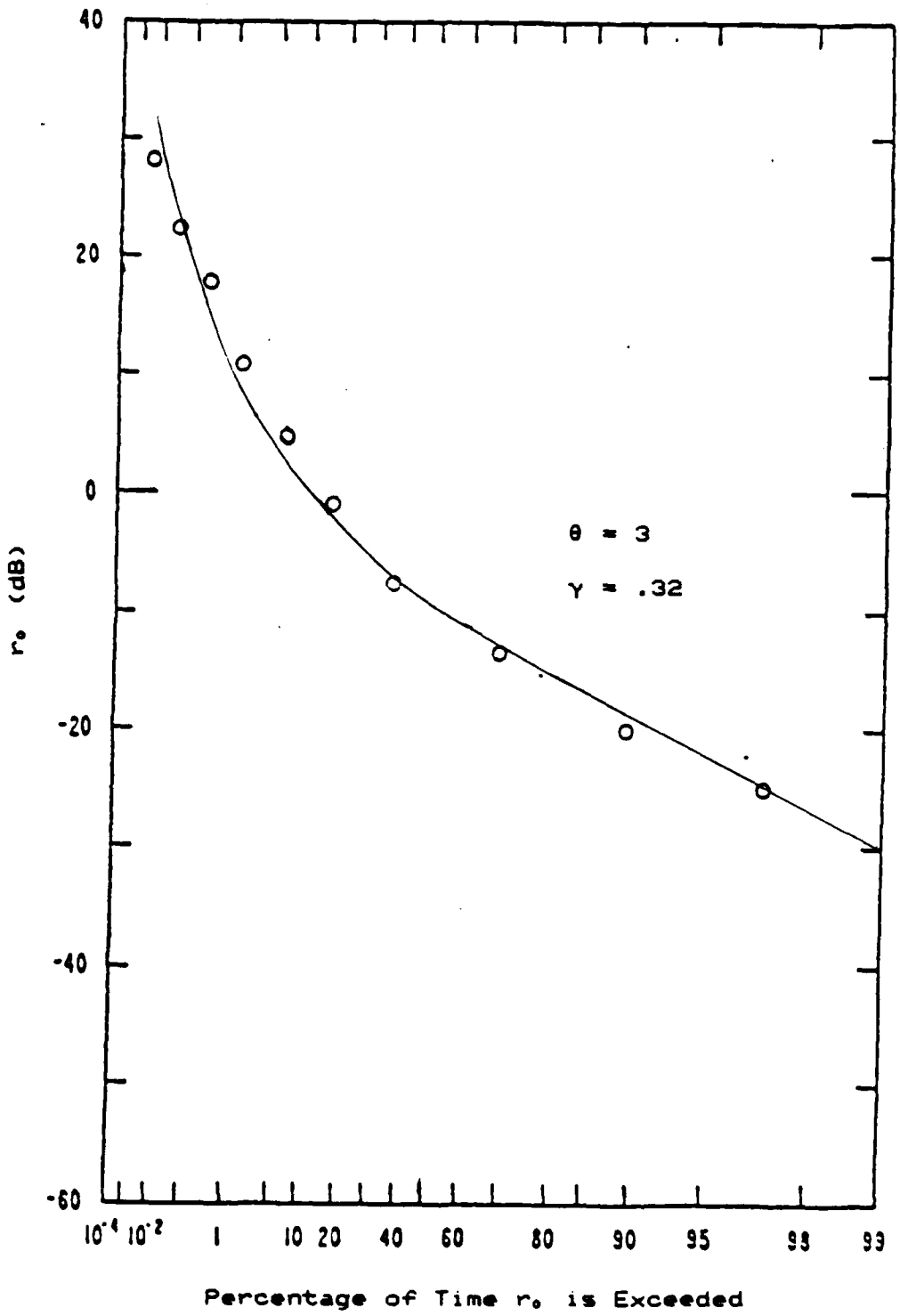

Figure 6. Atmospheric Noise and Hall Distribution

inphase and quadrature components is determined. Since the noise is narrowband it will be circularly symmetrical and the 2-D Fourier transform will become a Hankel transform [Ref. 20,21]. This characteristic function is transformed to polar coordinates, then inverted to determine the APD. Starting with the complex noise process described in Eqn. 2-18, the joint characteristic function of the inphase and quadrature components is

$$\emptyset(\omega_1, \omega_2) = E[e^{j(\omega_1 n_c(t) + \omega_2 n_s(t))}]. \qquad (2\text{-}33)$$

It is shown in Appendix B that the characteristic function of the envelope due to the Gaussian term is

$$\emptyset_g(\omega_r) = e^{-N_0 B(\omega_r^2)/2} \qquad (2\text{-}34)$$

and the characteristic function of the envelope due to the impulsive term is

$$\emptyset_I(\omega_r) = e^{\lambda \int_0^\infty p(a) \int_0^T [J_0(\omega_r a h_c(\tau)) - 1] d\tau da} \qquad (2\text{-}35)$$

where p(a) is the impulse amplitude density function, λ, the Poisson rate function, $h_c(t)$, the inphase component of the filter impulse response and J_0 is the ordinary Bessel function of the first kind. The density function of the envelope is then the inverse Hankel transform given by

$$p(r) = \int^\infty r\omega_r J_0(r\omega_r)\emptyset_g(\omega_r)\emptyset_I(\omega_r) d\omega_r . \qquad (2\text{-}36)$$

$-\infty$

This equation for the PDF is difficult to evaluate; however, a number of researchers have examined special cases to obtain results.

Furutsu and Ishida [Ref. 22] derived an equation of the same form as Eqn. 2-36 with no Gaussian term. They obtained many approximate results by considering the equation for specific source density functions. If p(a) is exponential they found that the resulting envelope density was approximately Rayleigh for small amplitude values. If p(a) was uniformly distributed, the log-normal density was found to be a good approximation over most of the range of interest. If a strong local source of interference was present, Furutsu and Ishida showed that a function involving the confluent hypergeometric function was a good approximation. They also considered one special case were the unit counting function N(T) was modified to be a Poisson - Poisson branching process and showed that for low amplitudes the resulting density function was approximated by the simple Poisson case.

Giordano [Ref. 23] evaluated Eqn. 2-36 for various distributions of p(a) which he determined from assumed propagation laws and spatial distributions of impulse sources. In one particular case he adopted the following assumptions:

1. No Gaussian component

2. Uniform spatial distribution of impulse sources

3. Inverse distance law for received field strength

4. Arbitrary receiver envelope response

and showed that the APD of the envelope function was approximated by

$$Pr(r > r_o) = \frac{K}{(r_o^2 + K^2)^{1/2}} \tag{2-37}$$

where

$$K = c \int_0^T h(t)\, dt \ ,$$

T is the observation interval, h(t) the filter response, and c is a scenario dependent constant. This result is significant because it has the same form as the APD of the Hall2 model and physically justifies what had heretofore been an empirical model.

Middleton [Ref. 24] included the Gaussian noise term in Eqn. 2-36 and expanded the characteristic function without taking the expectation. Then by inverting the characteristic function term by term, a canonical form of the envelope density function can be obtained. The exceedance probability was then shown to be

$$Pr(r > r_o) = e^{-r_o^2 \left[1 - r_o^2 \sum_{m=0}^{\infty} \frac{(-1)^m}{m!} A_o^m \Gamma(1 + \frac{m\alpha}{2}) {}_1F_1(1 - \frac{m\alpha}{2};\ 2;\ r_o)\right]} \tag{2-38}$$

where ${}_1F_1$ is a confluent hypergeometric function, and α and A_0 are two parameters that are determined by the source distributions and the propagation law.

E. HALL MODEL EXTENSIONS

For later work in this dissertation a model for atmospheric noise statistics is required. This section will further describe the Hall model as applied to HF atmospheric noise and will derive some extensions to it that will be used to digitally simulate atmospheric radio noise.

The Hall model for the envelope statistics of radio noise is

$$p(r) = (\theta - 1)\,\gamma^{\theta-1} \frac{r}{(r^2 + \gamma^2)^{((\theta-1)/2)}} \qquad (2\text{-}39)$$

and was chosen for a number of reasons. The most important are: the Hall model is analytically tractable and shows a good fit to the data. It can be obtained for certain values of the parameter θ, starting from the physically based filtered impulse models. This was shown by both Giordano [Ref. 23] and Middleton [Ref. 24]. Additionally, Schonhoff [Ref. 18] has related the Hall models to CCIR Report 332 [Ref. 25], the standard reference of first order statistics of atmospheric noise. In the CCIR report the APD curves are shown as a function of V_b. The parameter, V_b, is a commonly used measure of the impulsiveness of atmospheric radio noise and is defined as

$$V_b = 20\log \frac{E[r^2]^{1/2}}{E[r]} \qquad (2\text{-}40)$$

where r is the amplitude of the received envelope. For quadrature Gaussian noise V_b = 1.05 dB and as the noise envelope becomes more impulsive, V_b will increase.

One problem in relating the Hall model to V_b is that the moments of the Hall model only exist for orders greater than θ-1. This means that for the Hall2 and Hall3 models, V_b is undefined unless the model is modified. Two methods have been proposed to do this. Hall's method [Ref. 3] adds another term to the envelope density function and multiplies by a negative exponential term to reduce the tail of the density function and give finite moments. The advantage of this method is that the density function exists from 0 to infinity; however, the resulting density function is complicated. The method proposed by Schonhoff [Ref. 18] truncates the Hall2 and Hall3 distributions above a set level, T_p, and renormalizes the density function by picking k such that

$$\int_0^{T_p} k\, p(r)dr = 1. \qquad (2\text{-}41)$$

The level, T_p, is chosen to set a desired V_b for the distribution. The constant k will be a function of D where

$$D = (1 + (T_p/\gamma)^2)^{1/2}. \qquad (2\text{-}42)$$

The existence of the first and second moments for these two distributions is then assured. Using this procedure Schonhoff generated a family of distributions parameterized by θ that can be used to represent a wide range of measured data. By matching the V_b ratio of the data to the distribution, a close fit to the APD is found.

An extension to the basic Hall model to be used in a later chapter is the density function of a constant amplitude sinusoid plus the assumed noise. This density is analogous to the Rician density in Gaussian noise theory. It will be used in simulating the performance of energy detection receivers for the signal plus noise case. It was derived in [Ref. 26] for the Hall2 model and it is derived for the Hall3 and Hall5 models in Appendix C. For the Hall3 model the density function is

$$p(r) = \frac{(r^2 + A^2 + \gamma^2)\, 2\gamma^2 rD}{(r^4 - 2A^2 r^2 + 2A^2\gamma^2 + 2\gamma^2 r^2 + A^4 + \gamma^4)(D^2 - 1)} \qquad (2\text{-}43)$$

where A is the signal amplitude, γ is a Hall3 noise parameter and D is defined in Eqn. 2-42. Likewise the density function for the Hall5 model is

$$p(r) = \frac{2\gamma^4 r(b^2 + 2a^2)}{(a^2 - b^2)^{5/2}} \qquad (2\text{-}44)$$

where

$$a = r^2 + A^2 + \gamma^2$$

and

$$b = -2Ar.$$

Fig. 7 is an example of the APD for a sinusoid plus Hall3 noise with the RMS value of the noise set to 1 and the signal to noise ratio at -26, -6 and 14 dB. For the -26 dB SNR case the APD is very similar to the Hall3 noise only density shown in Fig. 6.

Commonly used functions relating to the Hall models are shown in Table I. These are the envelope density function, the 1st and 2nd moments of the envelope, the inverse of the CDF, the quadrature marginal density function and the Hall noise plus random sinusoid density. The parameter D in Table I is defined by Eqn. 2-42 and the function $E[\cdot]$ is the complete elliptic integral of the second kind. The quadrature components can be derived by transforming the envelope density to rectangular co-ordinates and integrating with respect to one component. The inverse of the envelope CDF is also included since it provides an easy method to generate random deviates.

Also useful for simulation purposes are the values of the Hall parameters, θ and γ, for different values of V_b normalized to a unit root mean square value. The truncation point T_p was found for a desired V_b using an iterative technique. These parameters are shown in Table II.

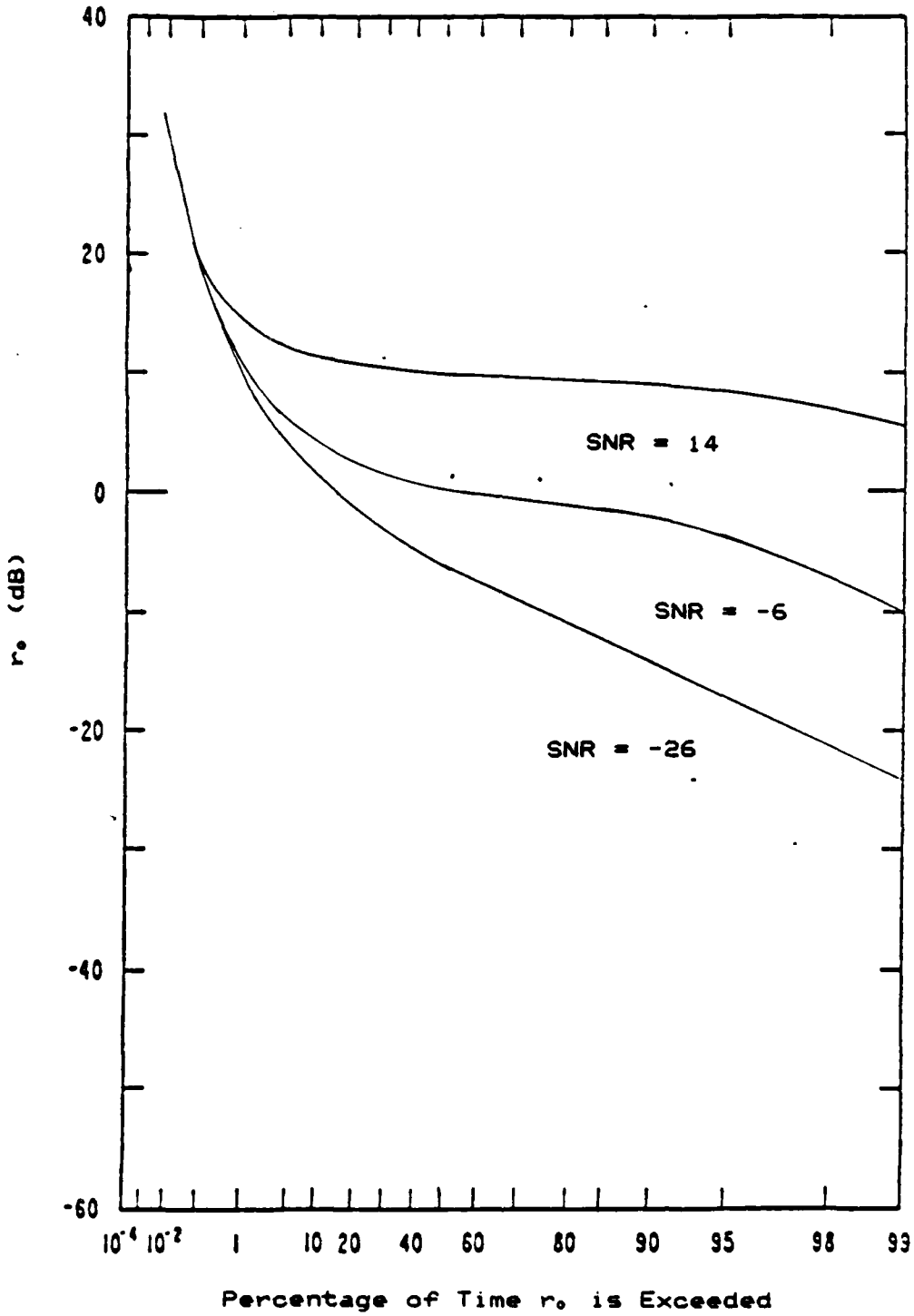

Figure 7. Hall Noise plus Signal Distribution

	Hall5	Hall4	Hall3	Hall2
Envelope PDF $p(r)$	$\dfrac{4\gamma^4 r}{(r^2+\gamma^2)^3}$	$\dfrac{3\gamma^3 r}{(r^2+\gamma^2)^{5/2}}$	$\dfrac{D^2\, 2\gamma^2 r}{(D^2-1)\,(r^2+\gamma^2)^2}$ $\quad 0 < r < T_0$ $0 \quad r > T_0$	$\dfrac{D\,\gamma r}{(D^2-1)\,(r^2+\gamma^2)^{3/2}}$ $\quad 0 < r < T_0$ $0 \quad r > T_0$
1st Moment	$\dfrac{\gamma\pi}{4}$	γ	$\gamma\left\{\dfrac{D^2\,\mathrm{atan}((D^2-1)^{1/2})-(D^2-1)^{1/2}}{(D^2-1)}\right\}$	$\dfrac{\gamma D}{D-1}\left\{\dfrac{-(D^2-1)^{1/2}}{D}+\ln(D+((D^2-1)^{1/2})\right\}$
2nd Moment	γ^2	$2\gamma^2$	$\gamma^2\left\{\dfrac{2D\ln(D)}{(D^2-1)}-1\right\}$	$\gamma^2(D-1)$
Inverse of Envelope CDF $r = P^{-1}(u)$	$\gamma((1-u)^{-1/2}-1)^{1/2}$	$\gamma((1-u)^{-2/3}-1)^{1/2}$	$\gamma\left\{\dfrac{D^2}{(u-D^2u+D^2)}-1\right\}^{1/2}$	$\gamma\left\{\dfrac{D^2}{(u-Du+D)^2}-1\right\}^{1/2}$
Quadrature PDF $p(x)$	$\dfrac{3\gamma^4}{(x^2+\gamma^2)^{5/2}}$	$\dfrac{2\gamma^3}{\pi(x^2+\gamma^2)^2}$	—	$\dfrac{(\gamma^2D^2-(x^2+\gamma^2)^2)^{1/2}}{(D-1)\pi(x^2+\gamma^2)^2}$ $\quad \lvert x\rvert < T_0$ $0 \quad \lvert x\rvert > T_0$
Signal + Noise PDF	$\dfrac{2\gamma^4 r(b^2+2a^2)}{(a^2-b^2)^{5/2}}$ $a = r^2+A^2+\gamma^2$ $b = -2Ar$	—	$\dfrac{2\gamma^2 rD^2}{(a^2-b^2)^{3/2}(D^2-1)}$ $\quad 0 < r < T_0-A$ $0 \quad r > T_0-A$ $a = r^2+A^2+\gamma^2$ $b = -2Ar$	$\dfrac{2\gamma rDE((2b/(a+b))^{1/2})}{\pi(a-b)(a+b)^{1/2}(D^2-1)}$ $\quad 0 < r < T_0-A$ $0 \quad r > T_0-A$ $a = r^2+A^2+\gamma^2$ $b = -2Ar$

TABLE I.

V_b	Hall No.	$E[n^2(t)]$	$E[n(t)]$	T_p	γ	D
2.1	5	1	.785	-	1.01	-
3	4	1	.708	-	.708	-
4	3	1	.631	11.66	.420	27.76
5	3	1	.562	25.90	.364	71.05
6	3	1	.501	67.71	.321	211.1
8	2	1	.398	11.77	.085	137.6
10	2	1	.316	17.08	.058	291.0
12	2	1	.251	24.25	.041	587.1
14	2	1	.199	33.81	.029	1141.9

TABLE II

F. SUMMARY

Both empirical and analytical filtered impulse models have been successful in explaining the first order envelope statistics of bandpass radio noise processes. However, in obtaining these results the assumption has to be made that the impulse arrival times due to the noise process form a Poisson point process. In general this will not be true for man-made impulsive noise and for some types of atmospheric noise [Ref. 27]. In most cases of man-made noise the underlying deterministic mechanism of the device causing the noise will modulate or regulate the impulse distribution. The Hall model for atmospheric noise has been examined in

detail and some useful extensions to it have been derived that will allow noise and signal plus noise environments to be simulated.

III. GAP NOISE MODEL

A. INTRODUCTION

In this chapter a specific source of man-made radio noise will be modeled and specified in terms of the counting process, N(t), and the probability density function (PDF) of the impulses, p(a). These specifications were introduced in the previous chapter to define the impulsive noise model. The noise source that will be examined is gap type discharges and is commonly found on electric power distribution and transmission lines. Gap noise is one of the major types of interference from power lines and is frequently observed as the primary interference to communication systems operating in the high frequency (HF) radio band.

B. GAP NOISE MECHANISM

At least two mechanisms have been found by which a gap discharge process can occur on a power line. The resistance in the line insulators can be degraded allowing current to flow through the insulator base and creating a potential gradient across any gaps or defects in the insulator mounting hardware. A second way in which a potential can be created across an air gap is by an electro-static coupling of the line potential to isolated hardware on the pole. In both cases the potential across the gap is discharged by the

voltage breakdown of the gap and the resulting rapid current flow or spark. This process generates a radio frequency (RF) noise impulse with spectral components extending into the hundreds of MHz. During a single discharge, the potential across the gap is temporarily diminished. However, while the fundamental 60-Hz waveform is still greater than a threshold voltage, the process can occur again. The spark will discharge across the gap repeatedly until the alternating current waveform drops below the breakdown threshold potential. [Ref. 28:p. 78,29]

The spark discharge and recharging of the gap potential indicates that this type of process is regenerative and can be modeled as a renewal process where the renewal points are associated with the sparks. One feature of gap noise that complicates the modeling is the 120-Hz on-off-on modulation imposed on the renewal points by the alternating current (AC) waveform. One way to account for this effect is to consider the turn on times as another renewal process driving the spark discharge process. This type of model is known as a branching renewal process [Ref. 30].

The noise processes that were used to develop this model were short term stationary in that the statistics of the process did not change over the observation interval. Not all sources of power noise are stationary even over a short observation interval. Physical effects such as wind, solar heating and varying line loads can act to make certain types

of power line noise highly variable from observation to observation. Although these types of noise were observed during data collection, the data used to develop the model was taken from noise sources that were stationary for the length of the ten minute data records.

C. OBSERVED TIME-DOMAIN CHARACTERISTICS

The gap noise sources for this study were observed on utility distribution lines in the vicinity of the Naval Postgraduate School and were chosen to illustrate parameters of the noise model. Fig. 8 is a typical time-domain observation of a gap discharge process observed at 3 MHz and envelope demodulated with a 10-kHz Gaussian bandpass filter. The important characteristics to note are:

1. the process has an on-off-on modulation at a 120-Hz rate related to 60-Hz waveform of the power line, and

2. the pulse groups that result from the modulation have a probabilistic number of impulses occurring in each group and a probabilistic interarrival time between pulses in a group.

In the first pulse group, 9 pulses occur with varying amplitudes and interpulse arrival times. In the second pulse group starting approximately 8.33 msec later, 8 pulses occur, again with varying amplitudes and interarrival times. One group of pulses is associated with either the positive or negative polarity of the line voltage waveform and the other group with the opposite polarity. Identification of

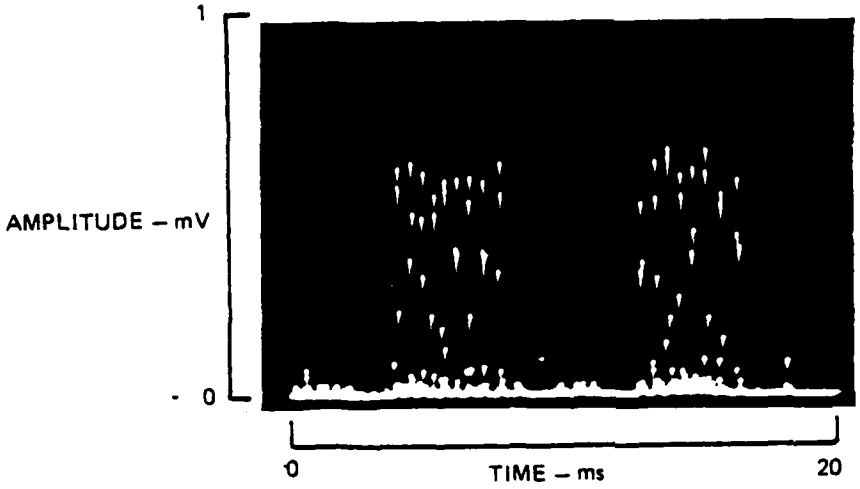

Figure 8. Envelope of Demodulated Gap Noise

the polarity is impossible without physically locating the source.

The average amplitude of the impulses will be one of the parameters for the model. An estimate of this parameter can be made from the above presentation. It is important to note that for this highly impulsive type of noise that the observed amplitude is a function of the shape and width of the effective bandpass filter and the detector characteristics.

At this point it should be noted that the model can be approached at two levels of complexity. In the simple version the data from both the positive and negative phases is considered as a whole and averaged over the two phases to determine a set of average parameters. In the more complex, but more accurate model, two sets of model parameters are determined - one for each phase. For the remainder of this work the more complex case will be considered. The results for the simple case are presented in Moose and O'Dwyer [Ref. 31] and can easily be determined from the complex case by setting the parameters equal for both phases and simplifying the resulting equations.

In order to better characterize the interpulse arrival times, which will be used to determine two model parameters, the rising raster capability described in the instrumentation section was used to generate the display of a different gap noise source which is shown in Fig. 9. In

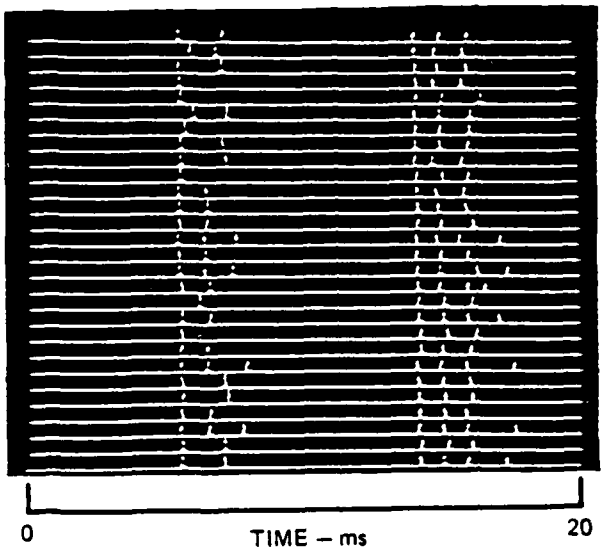

Figure 9. Multiple Scans of Gap Noise Interference

this picture the amplitude of each individual record was reduced and thresholded so that all that essentially remains is the time of impulse arrival data for 28 time records. The time base of the display was intentionally synchronized to the power line to facilitate taking data and this accounts for the regularity of the pulse groups from observation to observation. In this view the interarrival times for 56 pulse groups (28 groups of one polarity and 28 of the opposite polarity) can be determined along with the number of pulses in each of the 56 successive pulse groups. The average number of pulses per group considered separately for each phase will also be used as estimates of two model parameters.

Fig. 10 is a histogram of the distribution of the interarrival times between the observed impulses for the same noise process shown in Fig. 9. To use this data to generate parameters for the noise model, the histogram will be approximated by a continuous density function. The gamma density function [Ref. 32:p. 18]

$$p(t) = \lambda(\lambda t)^{r-1} e^{-(\lambda t)} / (r-1)! \qquad (3\text{-}1)$$

was chosen because it showed a close fit to the data, and its characteristic function, which will be used in later derivations, was particularly simple. The characteristic function of the gamma density is

$$\emptyset(j\omega) = (1 - j\omega\lambda)^{-r} . \qquad (3\text{-}2)$$

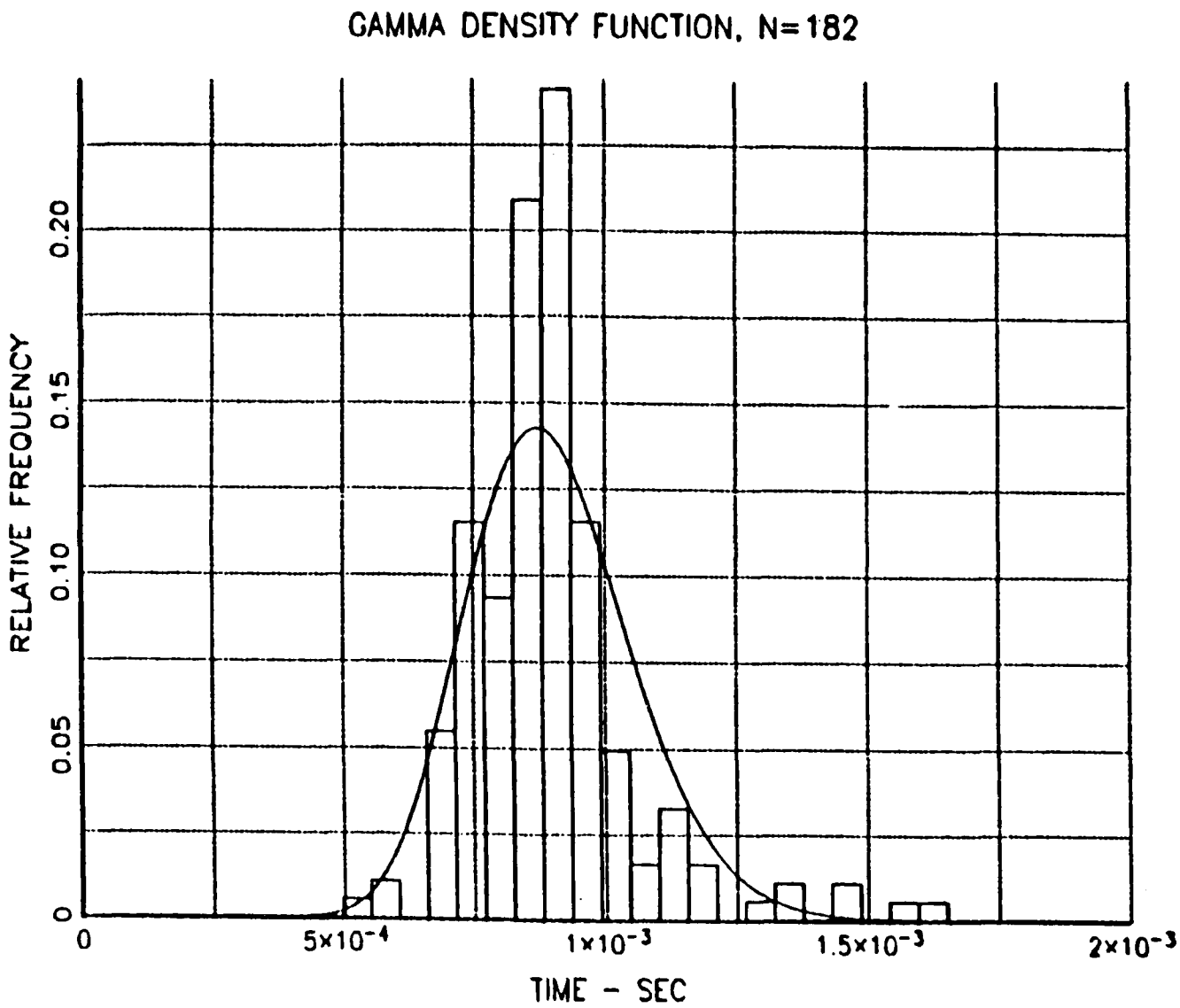

Figure 10. Histogram of Impulse Interarrival Times (Case 1)

The r and λ parameters are simply interpreted in terms of an underlying Poisson process as the time to the rth point of a Poisson process of intensity λ. If μ is the random variable assigned to the observed interarrival times then the unbiased estimate of the mean of μ is

$$\text{est}(\bar{\mu}) = (1/N) \sum_{i=1}^{N} \mu_i \tag{3-3}$$

and the unbiased estimate of the variance is

$$\text{est}(\sigma_\mu^2) = \{ \sum_{i=1}^{N} \mu_i^2 - N\, \text{est}(\bar{\mu})^2 \}/(N-1). \tag{3-4}$$

The unknown parameters of the desired gamma density function are estimated using the method of moments [Ref. 33:p. 250] using the following relations;

$$r = \text{est}(\bar{\mu})^2/\text{est}(\sigma_\mu^2) \quad \text{and} \quad \lambda = \text{est}(\bar{\mu})/\text{est}(\sigma_\mu^2). \tag{3-5}$$

Using this approach, the gamma density function used to approximate the interarrival time histogram is also plotted on Fig. 10. Figs. 11 and 12 are based on the same data as Fig. 10. However, they are separated according to different phases. It can be seen from the r and λ parameters in Table III that there is a significant difference between phases of the same gap noise process shown in the histogram even though the mean value of each data set was almost the same. The data in Fig. 11 was more clustered than the Fig. 12 data. This results in a higher r and lower λ parameter for

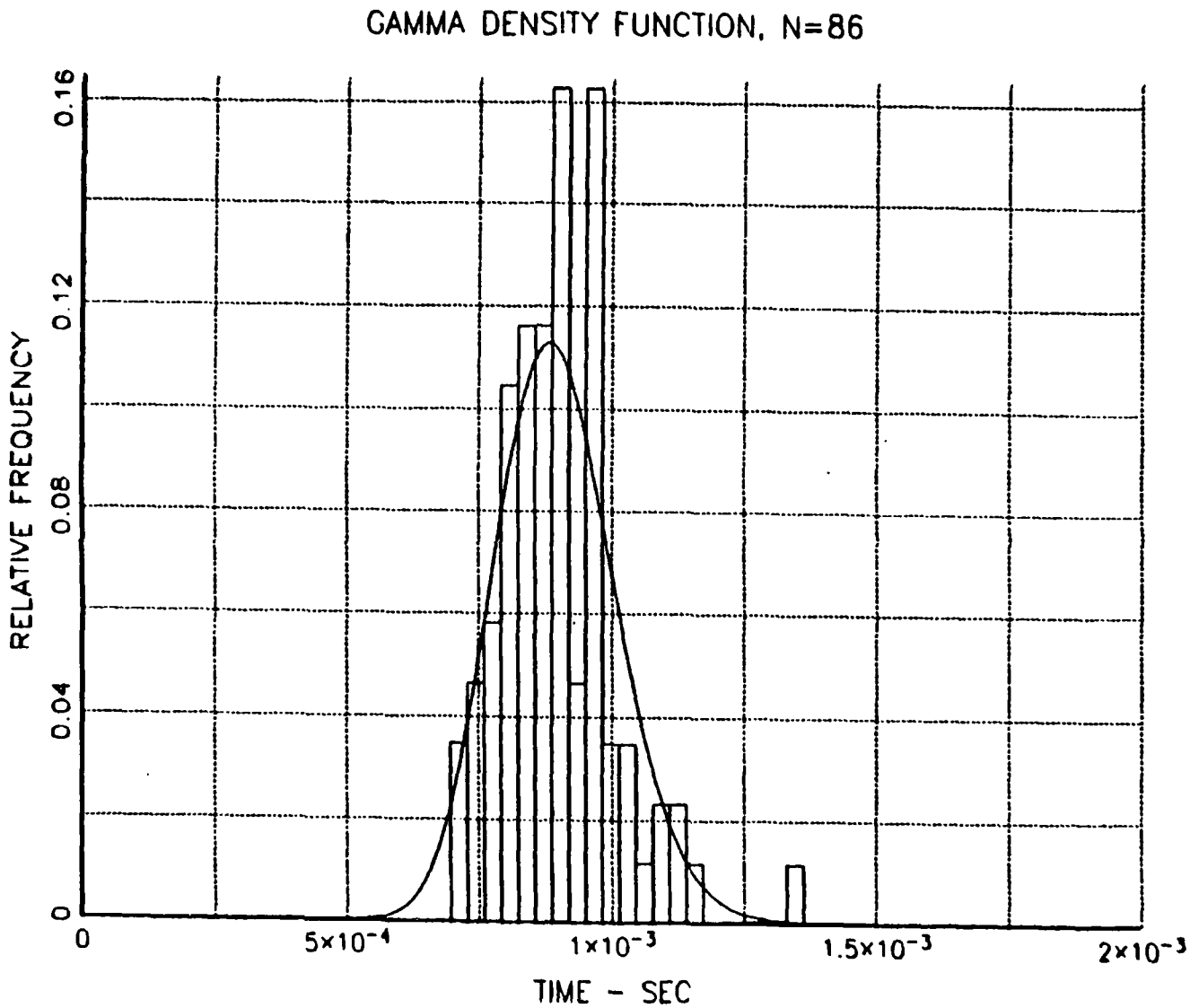

Figure 11. Histogram of Interarrival Times (Case 1 - Phase A)

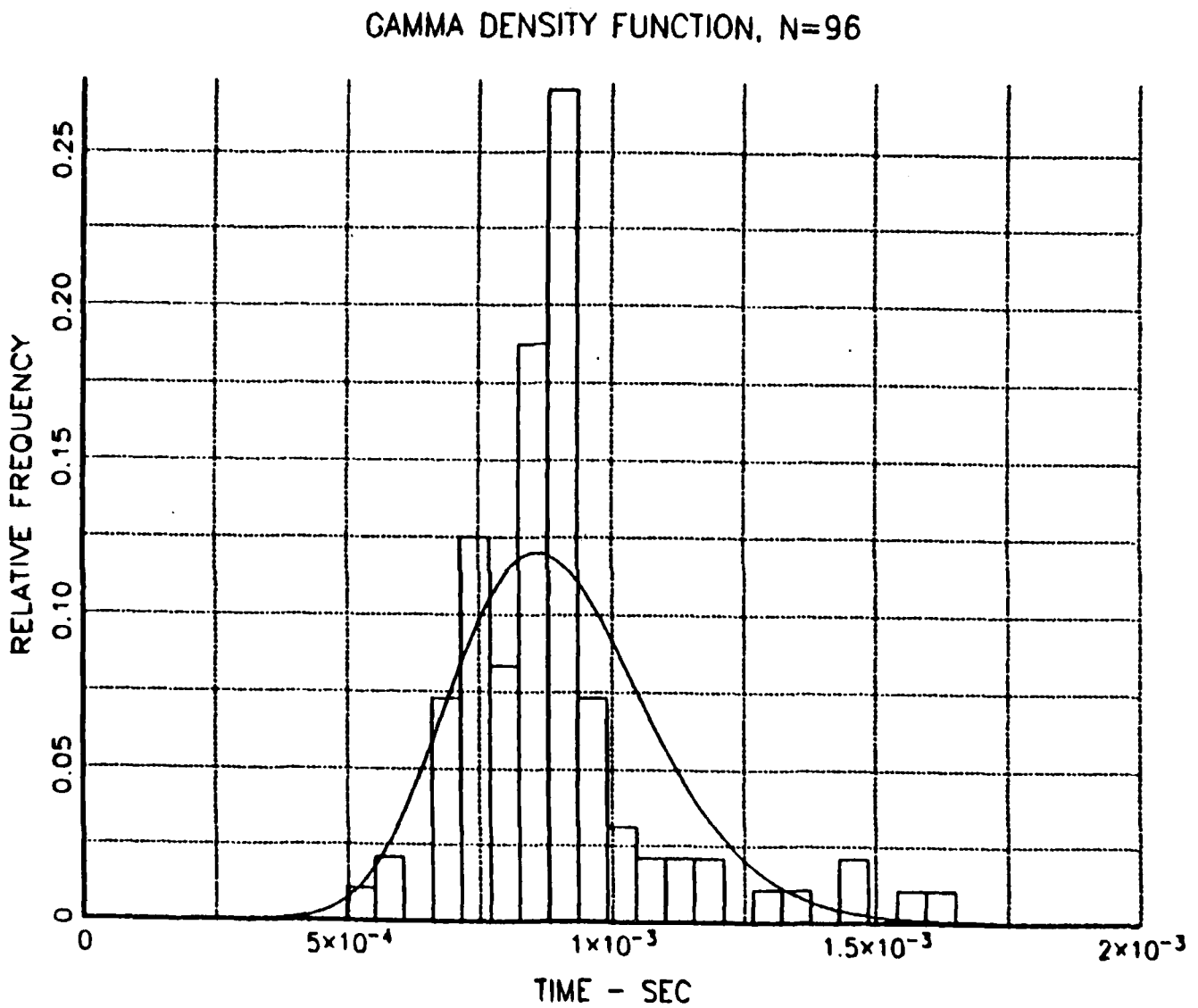

Figure 12. Histogram of Interarrival Times (Case 1 - Phase B)

the same mean value. Figs. 13 and 14 are additional sets of gap noise data that were observed during the research.

Table III summarizes the r and λ parameters fitted to the data described above.

	r	λ
Case 1	33.2	37,000
Case 1 Phase A	63.4	71,400
Case 1 Phase B	23.3	25,900
Case 2	44.3	74,600
Case 3	14.1	19,200

TABLE III

A final model parameter will be called T_0 and is a constant delay or offset of every second pulse group that exists with respect to the fundamental voltage waveform.

In summary the inputs to the model based on time-domain data are;

1. An estimate of the average amplitude of all observed pulses.
2. An estimate of the average number of pulses per group for each phase.
3. An estimate of the mean of the interarrival time of the pulses for each phase.
4. An estimate of the variance of the interarrival time between pulses for each phase.
5. An estimate of the delay in the start time of the pulse groups of one phase with respect to the fundamental voltage waveform.

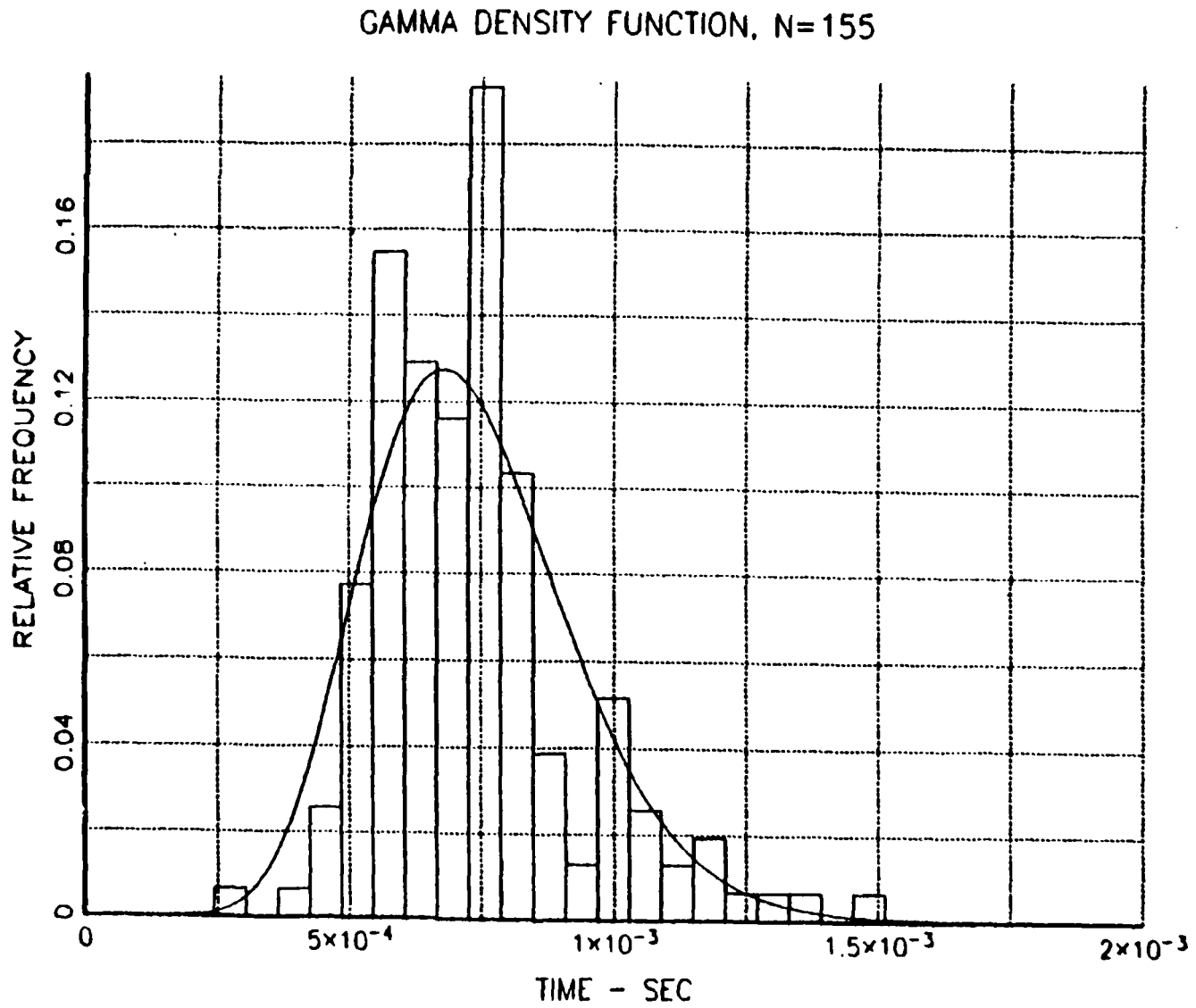

Figure 13. Histogram of Interarrival Times (Case 2)

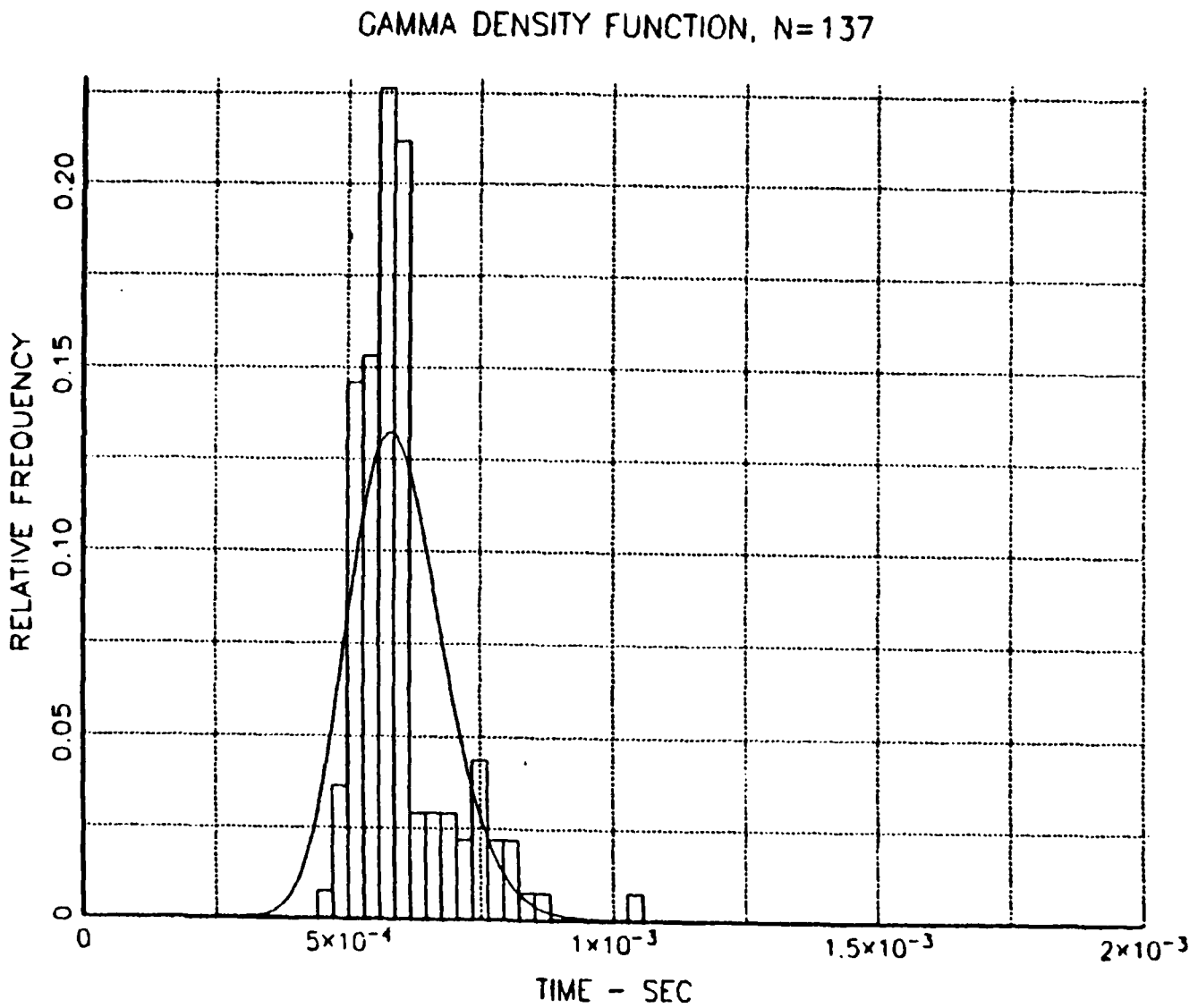

Figure 14. Histogram of Interarrival Times (Case 3)

The average amplitude of pulses from different gap noise sources is highly variable, ranging from the instrumentation noise floor to higher than any observable signal in the HF band. The average number of pulses per group has been observed to vary from 1 to greater than 20. The mean of the interarrival times ranges from .1 to 1 ms and the coefficient of variation (standard deviation divided by the mean) of the interarrival times has ranged from approximately .1 to .3 for the gap noise processes we have observed.

D. MODEL DEVELOPMENT

The principal goal of this chapter is to describe a noise model that, with suitable choice of parameters, provides an adequate simulation of the actual physical noise mechanism of gap noise. In this section the time-domain data and parameters derived in the previous section will be integrated into the filtered impulse model developed in Chapter II. Recalling from Chapter II, a filtered impulse noise process is given in complex envelope notation by

$$n(t) = g(t) + \sum_{i=1}^{N(t)} a_i e^{-j\theta_i} h(t-t_i) \qquad (3\text{-}6)$$

where p(a) is the amplitude distribution of the impulses, N(t) is a unit counting process whose statistics determine the impulse arrival times, θ is a random variable uniformly

distributed between 0 and 2π and $h(t)$ is the impulse response of the receiver filter.

In order to physically justify a filtered impulse model, the impulse duration must be small compared to the inverse bandwidth of the receiver filter. This condition is easily met in the case of gap discharges. Laboratory analysis of temporal characteristics of gap discharges for various geometries shows that the impulse durations range from 10 to 100's of nano-seconds [Ref. 34]. Therefore, for filter bandwidths up to 1 MHz the output noise process will only be a function of the incident time of the impulse and the filter response, not the waveform of the impulse.

The specification of the statistics of $N(t)$, the counting process that drives the model is then crucial to obtaining an accurate representation of the physical noise process. Based on the electrical characteristics of a gap discharge and the observed time-domain characteristics, the following assumptions are made;

1. A primary series of event times separated by an interval $T_0/2$ exists. T_0 is the fundamental period of the power line voltage waveform. The distribution of the time to the first primary event is uniform over 0 to T_0.

2. A subsidiary process commences at the primary event times i.e. $T_0/2$, T_0 , $3T_0/2$ ... The subsidiary process is a renewal process that continues for N1 or N2 renewals alternating between N1 and N2 renewals at successive primary points.

3. The interarrival times to the first and subsequent points of the subsidiary renewal process for each phase are all independent and identically distributed (IID) within a pulse. Each phase has its own set of parameters.

4. The weighting or amplitude distribution of all impulses in the subsidiary process is a constant.

5. A constant offset or delay designated by T_D may exist at every second primary renewal point.

The first assumption is supported by the periodicity in the data that is related to the fundamental frequency of the power line. The large majority of observed gap noise sources had pulse groups on both the positive and negative phases of the fundamental waveform. This accounts for the $T_0/2$ periodicity.

The second assumption addresses the differences between the sparking phenomenon on the positive and negative phases of the fundamental. It is frequently observed that the $E[N_{Pos}]$ is different than $E[N_{Neg}]$ where N_{Pos} and N_{Neg} are the random number of discharges in the pulse groups. This can be due to two effects; an asymmetrical gap geometry and the fundamental physical difference between the sparking mechanisms for positive to ground and negative to ground sparks. Two deterministic integer constants; N1 and N2 nearest to $E[N_{Pos}]$ and $E[N_{Neg}]$ respectively are assumed as the approximation to the variable number of sparks per half cycle of the fundamental waveform.

The third assumption is based on the fact that the "inception of gap discharges in natural air and the development of electron avalanche are fundamentally probabilistic processes that depend on atmospheric pressure, humidity, presence of natural ions, electrode surface and so on" [Ref. 34]. In view of the above statement and considering the empirical data, the justification for developing the gap discharge as a probabilistic process is well founded. The assumption of independence from discharge to discharge is not as well justified. Effects such as electrode heating after the initial discharge in a cycle could act to make the average interarrival time vary from pulse to pulse within a pulse group. However, to develop a tractable model the assumption of independence between arrival times is made. The gamma density function determined by the estimate of the mean and variance of the interarrival times for each phase is used to define the PDF of the interarrival times.

The fourth assumption concerns the amplitude of the impulses. In most cases the amplitude of the impulses within a pulse was nearly constant. In some cases there was a difference in the average amplitude from negative phase to positive phase, however to keep the model tractable the amplitude of all impulses is assumed constant.

The fifth assumption incorporates an effect that will explain one of the features observed in the power spectral

density (PSD) of the observed process. The physical rationale behind this assumption is that there may exist a difference in the threshold between the positive and negative phases, thus consistently delaying or offsetting the start of the renewal process on one of the phases.

The above assumptions place this model in a class of processes known as branching processes with the main process being a degenerate renewal process with an interarrival PDF of

$$p(t) = \delta(t-T_0/2) \tag{3-7}$$

The subsidiary process is a renewal process of N1 or N2 points. Consequently, the impulse source for the gap noise model is completely specified by the following parameters:

a - Amplitude of the impulses,

N1,N2 - Number of impulses in the subsidiary process,

μ_1, μ_2 - Mean value of impulse interarrival time,

$Var(\mu_1), Var(\mu_2)$ - Variance of interarrival times,

T_0 - Offset on one phase.

To complete an interference scenario $N_0 B_{eff}/2$ and h(t) must also be specified. The expression for the branching renewal process is then

$$n(t) = g(t) + \sum_{m=1}^{M(T)} \sum_{n=1}^{N_m} a_{mn} e^{-j\theta_{mn}} h(t-t_{mn}-T_m) \tag{3-8}$$

Fig. 15a,b shows sample realizations of the envelope, E(t), of the noise process defined above.

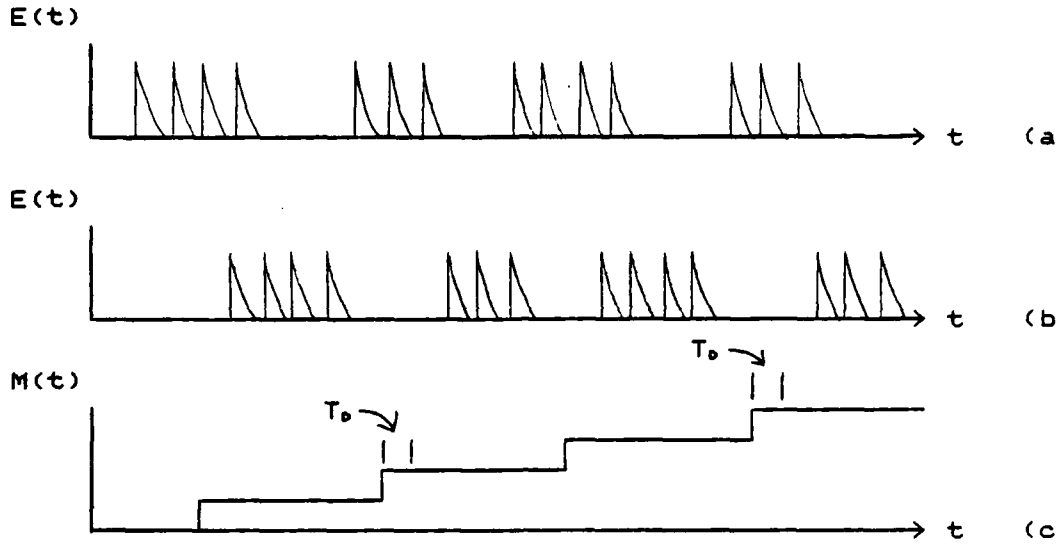

Figure 15. Envelope and Counting Function of n(t)

The Gaussian term was set to 0 and h(t) was approximated as a decaying exponential. Note that in comparison to an actual noise process illustrated in Fig. 8 the amplitude of the impulses is constant with a fixed number of impulses on the positive and negative polarity of the line voltage waveform. Fig. 15c is the primary counting process, M(T), driving the subsidiary process shown in Fig. 15b. Fig. 15b includes a non-zero T_D and its relationship to M(T) is shown in Fig. 15c.

Fig. 16 shows a realization of the envelope of this process for N1 and N2 = 3, T = 30 ms and gamma density function parameters r1 and r2 = 32 and $\lambda 1$ and $\lambda 2$ = 37,000. Random interarrival times with a gamma distribution were

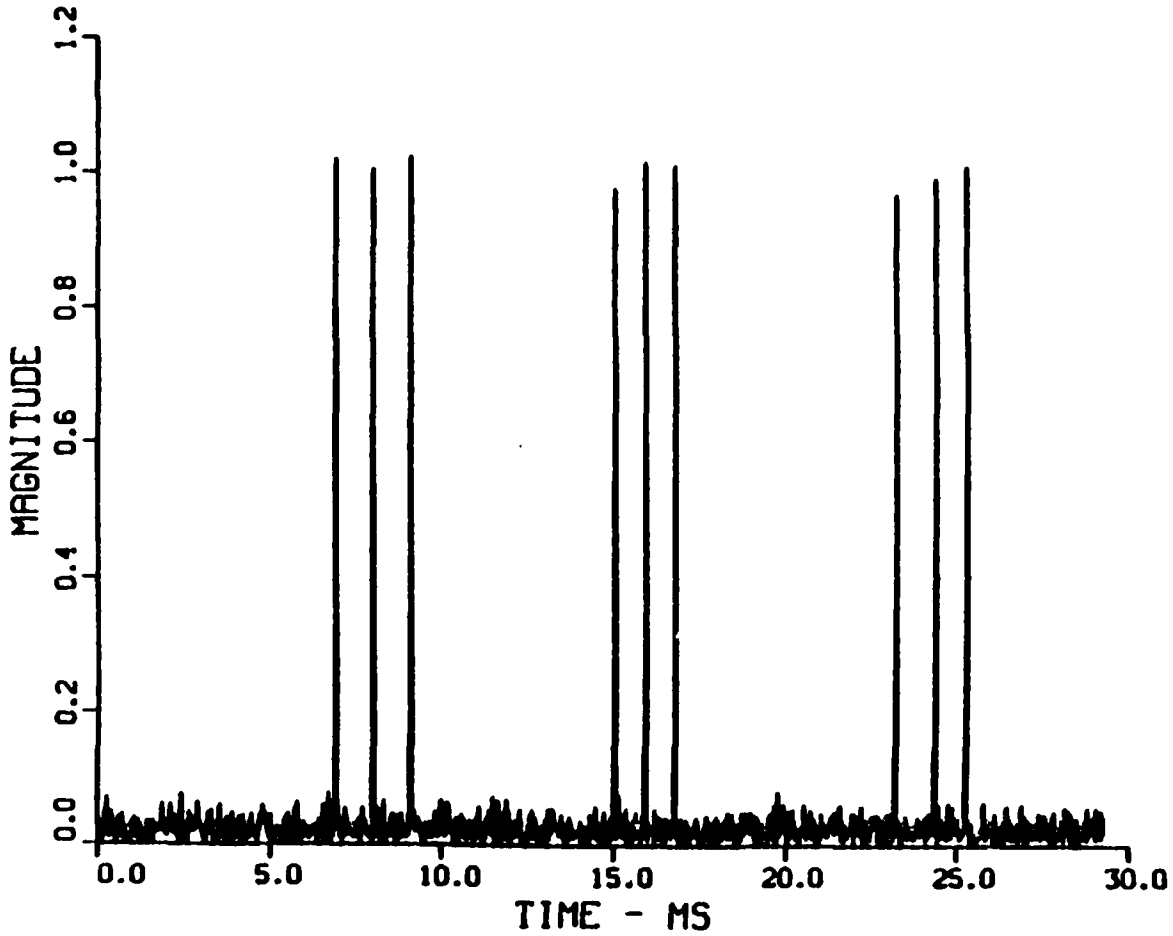

Figure 16. Synthetic Gap Noise

approximated by summing exponentially distributed random variables [Ref. 35]. The impulse amplitudes were normalized to one and a background level of quadrature Gaussian noise at $N_0B/2 = .0001$ was added which simulates either receiver noise or high density, low amplitude impulsive noise.

E. COMPARISON OF CALCULATED AND OBSERVED DATA

One partial description of a noise process is the amplitude probability distribution (APD) of the envelope. This description has been used extensively in the analysis of noise and in deriving optimum receivers. For the N(t) specified in the previous section this calculation would be difficult. A second noise process descriptor is the spectrum of the noise process. This descriptor is suited to our model where the structure of the noise is contained in the counting process that drives the impulse generation. In addition to receiver noise performance evaluation, spectral analysis can also be used for noise source identification and isolation [Ref. 36].

In order to determine the spectrum of the envelope squared of the branching renewal process defined by Eqn. 3-8, the spectrum of the envelope squared of a non-branching renewal process is determined in Appendix D. The results obtained in Appendix D are then used to derive the spectrum of the the branching renewal process which is postulated to model gap noise. Starting with the branching renewal

process given in Eqn. 3-8, and assuming g(t) is equal to zero, it is shown in Appendix E that the average of the Bartlett estimate of the PSD is:

$$S(\omega,T) = |H_e(\omega)|^2 / T \sum_{n=1}^{5} \text{Term } (n) \qquad (3\text{-}9)$$

where n is an index to the 5 Terms defined below. These five Terms involved in the summation in Eqn. 3-9 are defined as follows:

Term 1 - The inter-pulse group summations between pulses in pulse groups with N1 pulses

$$\text{Term } 1 = M2\ \Xi(\omega,N1) \qquad (3\text{-}9a)$$

Term 2 - The inter-pulse group summations between pulses in pulse groups with N2 pulses

$$\text{Term } 2 = M2\ \Xi(\omega,N2) \qquad (3\text{-}9b)$$

Term 3 - The intra-pulse group summations between pulses in groups with N1 pulses

$$\text{Term } 3 = \left\{ \frac{\cos(M2\ 2\pi\omega/\omega_o) - 1}{\cos(2\pi\omega/\omega_o) - 1} - M2 \right\} \Omega(\omega,N1) \qquad (3\text{-}9c)$$

Term 4 - The intra-pulse group summations between pulses in groups with N2 pulses

$$\text{Term } 4 = \left\{ \frac{\cos(M2\ 2\pi\omega/\omega_o) - 1}{\cos(2\pi\omega/\omega_o) - 1} - M2 \right\} \Omega(\omega,N2) \qquad (3\text{-}9d)$$

Term 5 - The intra-pulse group summations between pulses in groups with N1 pulses per group to pulses in groups with N2 pulses and vice versa

$$\text{Term 5} = 2\cos((\omega(T_o/2-T_D)))\left\{\frac{\cos(M2\ 2\pi\omega/\omega_o) - 1}{\cos(2\pi\omega/\omega_o) - 1}\right\}\psi(\emptyset_1, N1, \emptyset_2, N2) \tag{3-9e}$$

where $\emptyset_1$ and $\emptyset_2$ are the characteristic functions associated with the interarrival times for each phase. The parameters N1 and N2 are the number of renewals associated with each phase and Ξ, Ω, and ψ are defined below:

$$\Xi(\emptyset,N) = \frac{N - N|\emptyset(j\omega)|^2}{|1 - \emptyset(j\omega)|^2} - 2\,\mathrm{Re}\left\{\frac{\emptyset(j\omega)\ (1 - \emptyset(j\omega)^N)}{(1 - \emptyset(j\omega))^2}\right\}, \tag{3-10}$$

$$\Omega(\emptyset,N) = \frac{|\emptyset(j\omega) - \emptyset(j\omega)^{N+1}|^2}{|1 - \emptyset(j\omega)|^2}, \tag{3-11}$$

and

$$\psi(\emptyset_1, N1, \emptyset_2, N2) = \frac{(\emptyset_1(j\omega) - \emptyset_1(j\omega)^{N1+1})\ (\emptyset_2(-j\omega) - \emptyset_2(-j\omega)^{N2+1})}{(1 - \emptyset_1(j\omega))\ (1 - \emptyset_2(-j\omega))}. \tag{3-12}$$

As a test of the model the PSD of the gap noise process shown in Fig. 9 was determined using a spectrum analyzer and also analytically determined using only the model parameters from the time-domain data and the methodology of the previous section. Fig. 17 is a computer plot of the analytic estimate of the PSD which is compared with the observed PSD computed on a Wavetek UA500A spectrum analyzer shown in Fig. 18.

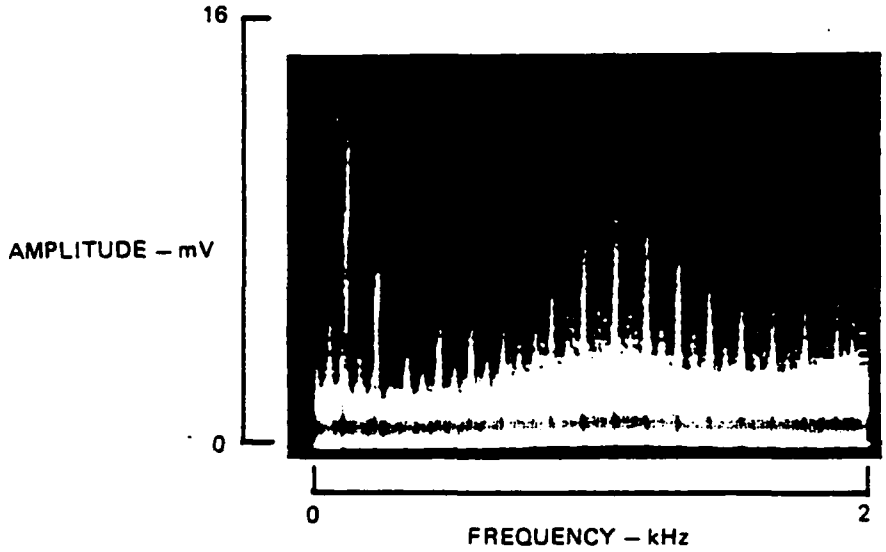

Figure 18. Observed Estimate of Power Spectral Density (PSD)

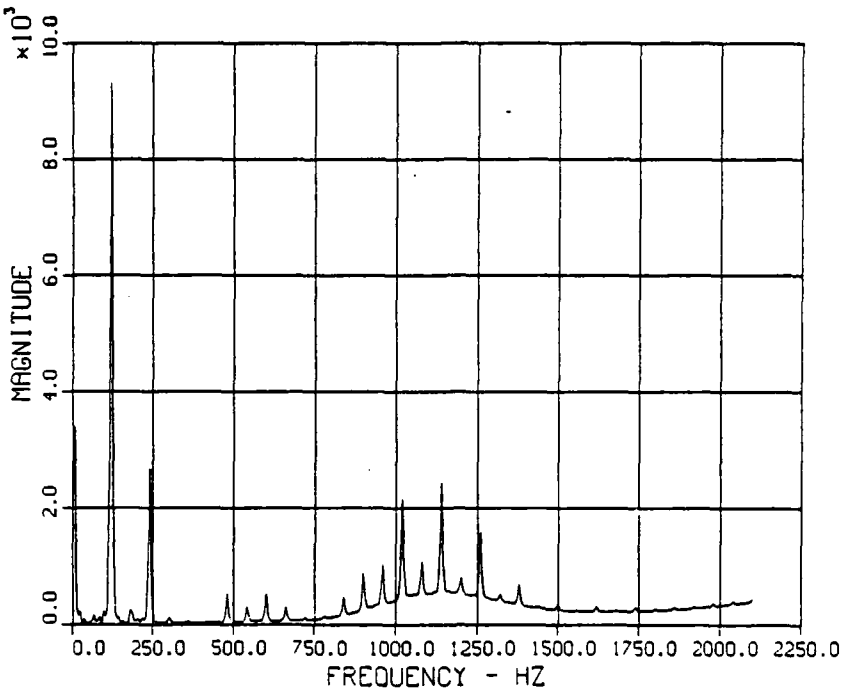

Figure 17. Predicted Power Spectral Density (PSD)

Comparing the two PSD's, it is seen that the analytical expression correctly predicted all of the significant features seen in the observed PSD.

The components of the spectrum due to the different terms is of interest and offers some insight into the origins of the features of the observed spectrum. The dominant feature of the observed spectrum are the periodic 120 Hz spectral lines. At 800 Hz the spectral lines change, and appear as odd harmonics of 60 Hz, however, still remaining at 120 Hz intervals. Terms 3 - 5 are responsible for the these spectral line features. Each of these terms is a comb function, determined by the fundamental frequency and observation interval, multiplied by an envelope determined

by the interarrival time distribution. Figs. 19 and 20 are Terms 3 and 4 respectively and clearly show the phase to phase difference. The more peaked behavior of Fig. 19 at 1100 Hz is due directly to the more clustered interarrival time behavior on one phase. This effect was observed in the time domain in Fig. 11. When the terms shown in Figs. 19 and 20 are added together, they form 60 Hz harmonic spectral lines and when Term 5, shown in Fig. 21, is added, positive reinforcement occurs at 120 Hz and negative at 60 Hz harmonics. This produces the observed 120 Hz harmonic spectral lines. When the cancellation is not complete due to differences in the characteristic function from phase to

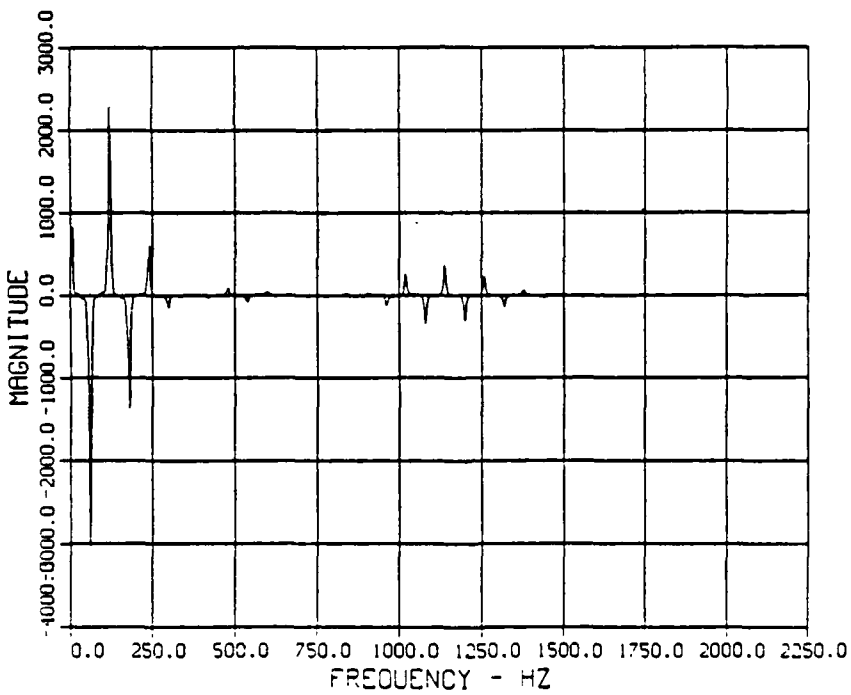

Figure 21. PSD Term due to Phase A to Phase B Intra-Pulse Group Correlations

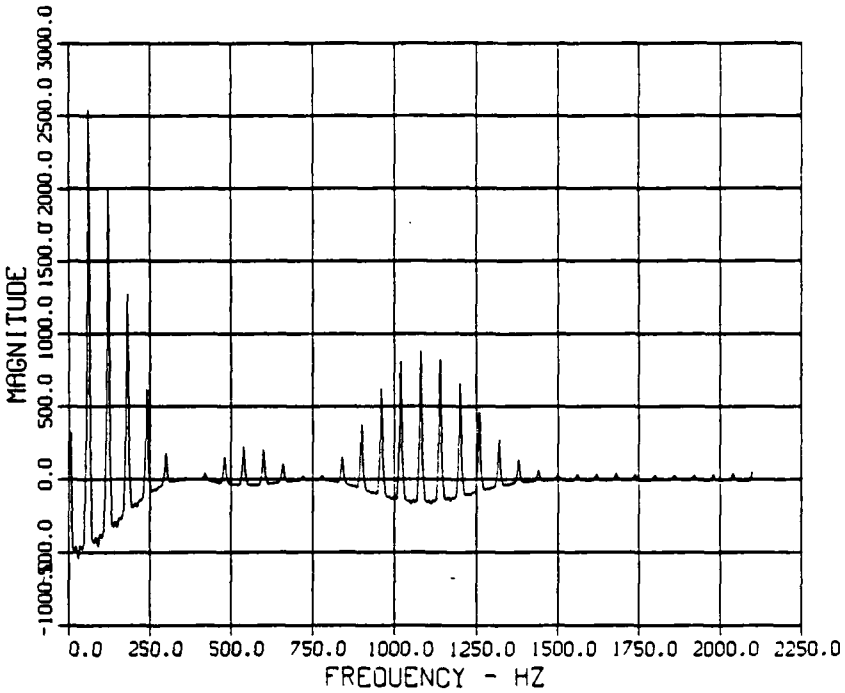

Figure 19. PSD Term due to Phase A Intra-Pulse Group Correlations

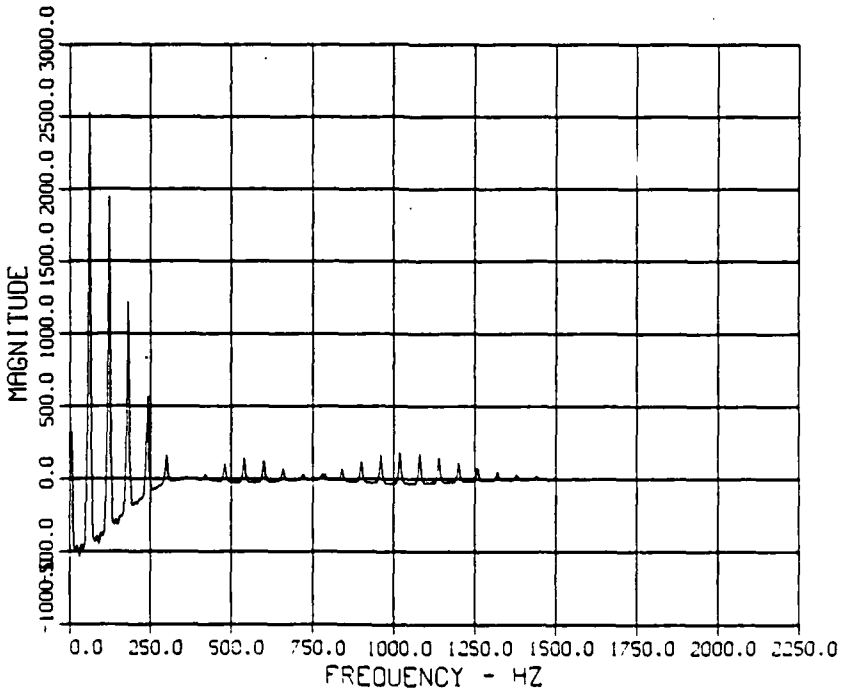

Figure 20. PSD Term due to Phase B Intra-Pulse Group Correlations

phase, small 60 Hz components can be present. This effect is seen in both the observed and predicted spectra.

The observed spectra changeover from 120 Hz harmonics to odd 60 Hz harmonics at 800 Hz is also correctly predicted by the model. This effect is due to the factor, T_b, appearing in Term 5 which causes the odd 60 Hz harmonics to be positively reinforced and the 120 Hz harmonics to be canceled out above 800 Hz. The final effect shown in the model and seen in the observed spectra is the presence of continuous spectral components. The continuous spectra due to Terms 1 and 2 is shown in Figs. 22 and 23 and also differs from phase to phase. The continuous spectra peaks markedly at 1100 Hz and this effect is apparent in the observed spectra as a rise in the noise floor. The continuous spectral term arises when Term 1 is added to Term 3 and Term 2 to Term 4. The peak value at 1100 Hz in Terms 1 and 2 is greater than the negative values in Terms 3 and 4 at the same frequency and when added together causes a continuous rise in the spectral floor. The reason for this is that the i to i+1 and i-1 interarrival times within a pulse group are more correlated than the corresponding interarrival times between different pulse groups. The more correlated arrivals appear in Terms 1 and 2 and cause the spectral peak to be larger.

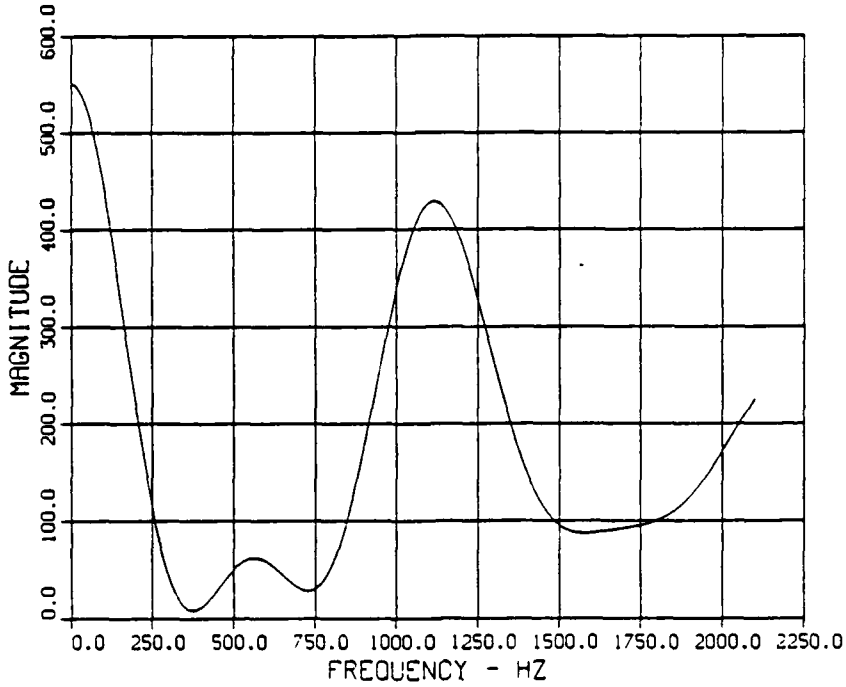

Figure 22. PSD Term due to Phase A Inter-Pulse Group Correlations

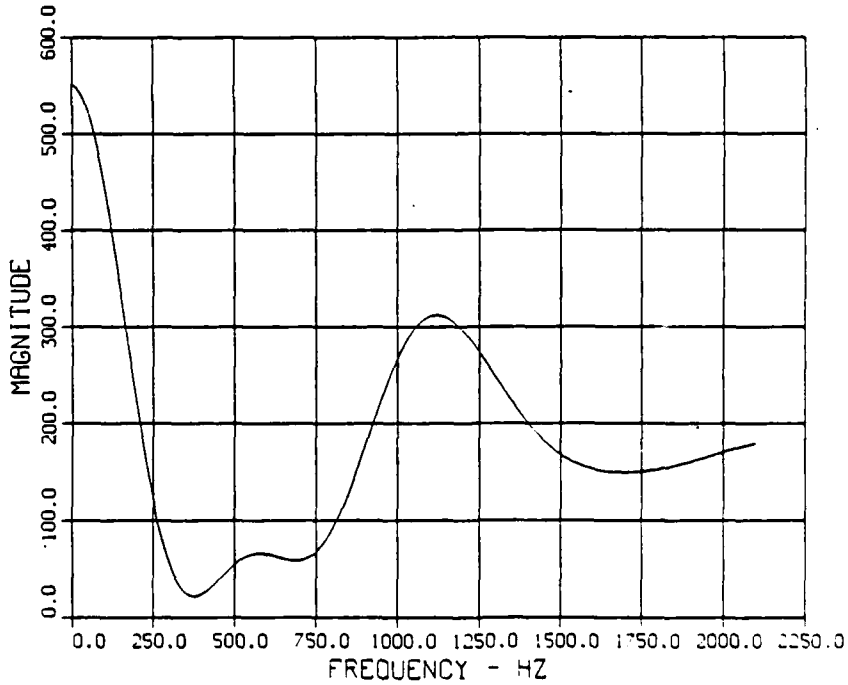

Figure 23. PSD Term due to Phase B Inter-Pulse Group Correlations

F. SUMMARY

A nine parameter model for a single source of gap noise interference was developed and shown to accurately predict the PSD of narrow bandwidth envelope demodulated gap noise interference. If less accuracy is desired, phase to phase differences can be neglected and the resulting model has only five parameters. The model was specified in terms of an impulse driving function, and techniques to estimate the model parameters from time domain data were described. Since the model specifies a complex driving impulse function it can be used as a simulated interference source for arbitrary filters and receivers.

IV. CORONA NOISE MODEL

A. INTRODUCTION

In addition to gap noise which was discussed in Chapter III, another major source of power line radio noise is corona noise. Corona is different in many respects from gap noise, and the model used to describe it will take a different approach. In contrast to gap noise, which is observed on both electric power transmission and distribution lines, corona noise is observed only on power transmission lines and generally has a fundamental frequency of 180 Hz corresponding to the three phases of a 60 Hz alternating current (AC) system. Corona noise is caused by a partial breakdown of air surrounding a conductor which is at a high potential. Consequently, the impulsive structure of corona noise is not as well defined as the highly impulsive structure of gap noise. Corona noise from AC sources appears somewhat like amplitude modulated Gaussian noise.

B. CORONA NOISE THEORY

When an increasing potential difference is applied between two electrodes, a breakdown voltage is reached that is characterized by the transition of air from a poor electrical conductor to a good conductor. If the field in the gap between the two electrodes exceeds the electric

strength of air, which is about 30 kV/cm for gaps over 1 cm in length, prior to the spark breakdown voltage, then corona will exist. Sharp points and small radius wires are avoided whenever possible on power lines, and corona generally does not become a significant source of radio interference until voltages exceed about 70 kV [Ref. 28:p. 84].

As the voltage on an AC line is increased, corona will appear and be associated with either the positive, negative or possibly both half-cycles of the fundamental waveform. For an aged, clean transmission line it appears that the threshold voltage for negative corona is less than that of positive corona. If the transmission line has any unusual characteristics, the threshold voltages of positive and negative corona become difficult to categorize [Ref. 37]. In particular, it has been observed that positive streamer corona, which is more disruptive of communications frequencies than negative corona, predominates on newly installed lines and during periods of precipitation. For modeling purposes, the important characteristics of corona noise are not a precise description of the physical mechanisms but the relationship between the observed interference waveform and the line voltage.

The procedure most commonly used for the prediction of interference due to corona noise gives the noise power as a function of the characteristics of the interference scenario. The random properties of the corona noise are

averaged out [Ref. 38]. These characteristics would commonly include distance from the line, the line voltage and a weather correction term. Each of these terms is experimentally verified and related to some physical process in the generation of corona noise. While this procedure gives an estimate of the noise power in a specified bandwidth, it does not incorporate the probabilistic nature or time-domain periodicity observed in the noise.

The approach taken in this chapter will continue with the filtered impulse theme of the dissertation. For corona noise, the counting process, N(T), will be modeled as a periodically modulated stream of impulses. This approach will have the advantage of being accurately able to simulate the time- and frequency-domain behavior of corona noise. However, as with the gap noise model it will suffer from the disadvantage that for each scenario, a set of parameters must be experimentally determined.

C. TIME DOMAIN CHARACTERISTICS

The time-domain data for corona noise was obtained using the instrumented van described in Appendix A. The antenna was a 3-meter whip mounted on the van (which was parked underneath a 3-phase 500-kV transmission line). The weather conditions at the time of measurement were clear and sunny. Records of the corona noise were obtained using the envelope detected output of the HP-141T described in Appendix A and

recording the data on a 20-kHz bandwidth, 85-dB dynamic range digital audio system. The recording process allowed subsequent analysis in the laboratory.

A 37-ms portion of a data record is shown in Fig. 24. The data was taken at a 300-kHz center frequency and 10-kHz intermediate frequency (IF). This particular picture was obtained by playing back the tape, re-digitizing the data and displaying it with a signal-analysis software package. One of the important features of the time-domain record in Fig. 24 is the periodicity. The fundamental frequency of 180 Hz can be determined from a periodic rise in the mean value of the noise and from a periodic increase in high-amplitude impulses. The fundamental noise frequency of 180 Hz on a three phase line indicates that the dominate noise is generated on one half-cycle of the fundamental 60-Hz waveform on each of the three phases of the line. This is consistent with low-level negative corona predicted for aged lines in clear weather.

The periodogram spectrum of the data record described above is shown in Fig. 25. The time-domain observations of the 180-Hz periodicity are confirmed and a 360-Hz harmonic of the fundamental is also present. At higher frequencies, no harmonics are observed and the spectrum becomes white. This is in distinct contrast to the gap noise described in Chapter III where the spectrum of gap noise has harmonics well into the kHz range. The periodicity can also be seen

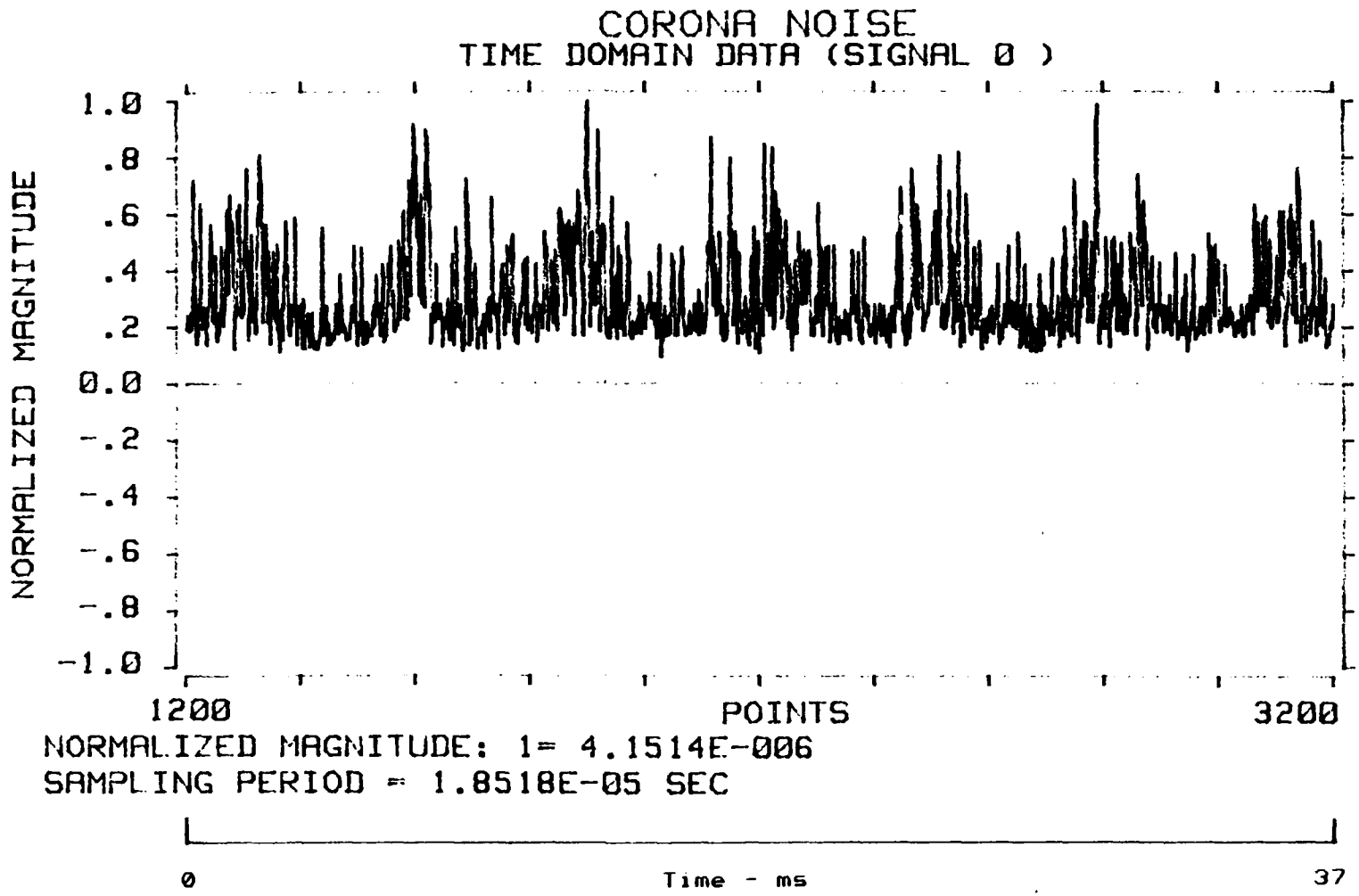

Figure 24. Corona Noise in Time Domain

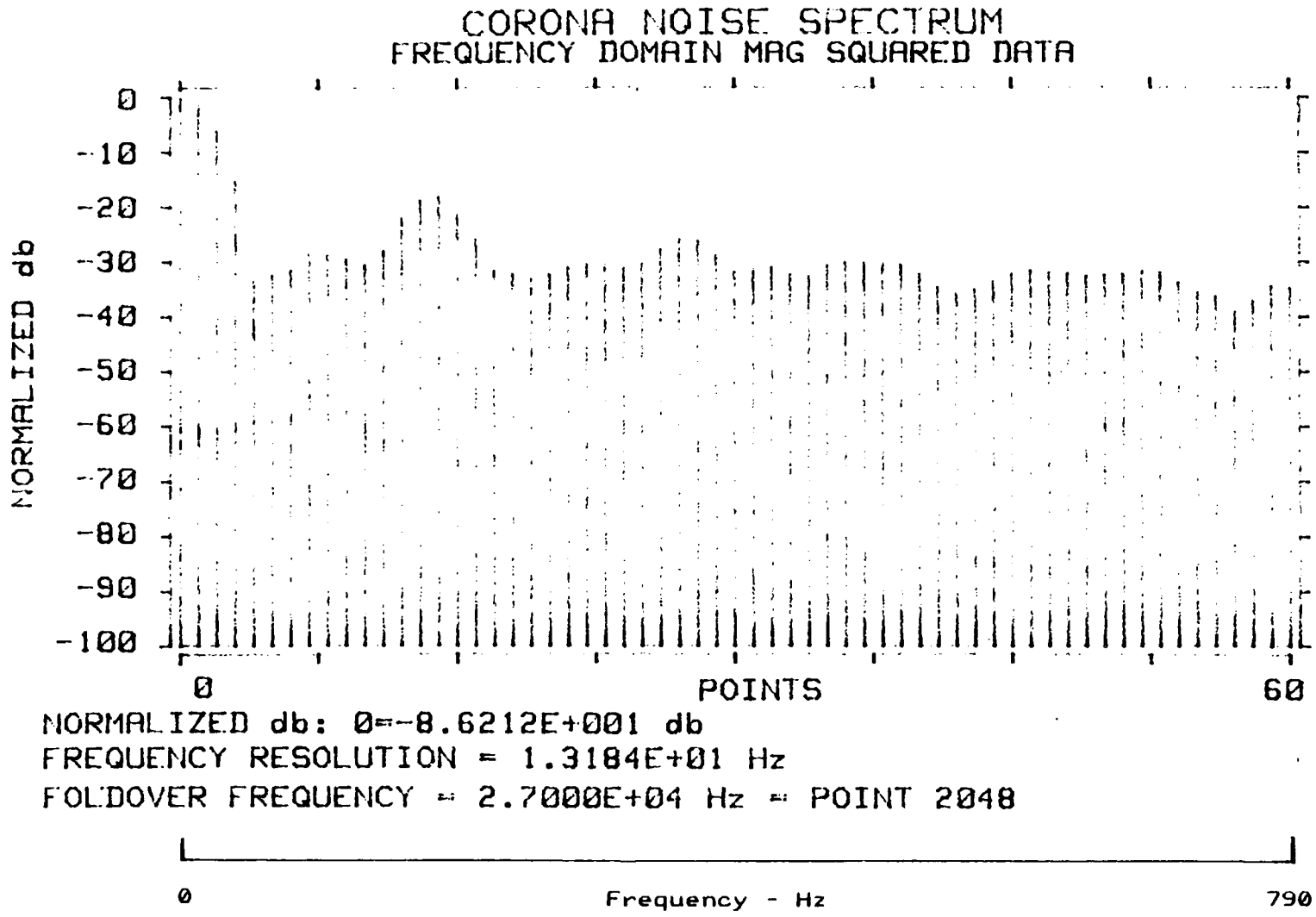

Figure 25. Corona Noise in Frequency Domain

in Fig. 26 (which is the same data recorded on the 3-Axis display). The contribution of each phase of the power line to the total corona noise process can be clearly seen in the lower picture in Fig. 26.

Another important feature of the data for modeling purposes is that the receiver response to an individual impulse overlaps with the response of preceding impulses. Although the noise is still impulsive, the simplifying assumption of non-overlapping pulses is not valid. It is seen in Fig. 24 that the amplitude of the impulses is random and there is no fine-grain interarrival time structure other than the periodicity discussed above. Both of these observations are in direct contrast to gap noise where the amplitude from impulse to impulse is almost constant, and there is a definite impulse interarrival time structure. These observations provide a method to distinguish between gap noise and corona noise.

An interesting aspect of noise from transmission lines was noted while taking measurements for the corona model. It was difficult to obtain a recording of power-line noise in the vicinity of high voltage transmission lines due only to corona noise. In many cases, a gap noise component was superimposed on the corona noise. This can be seen by comparing Figs. 26 and 27. Fig. 27 is a view of both gap and corona noise. The corona noise amplitude peaks at the 2 μV level, and the amplitude of the gap-noise impulses is

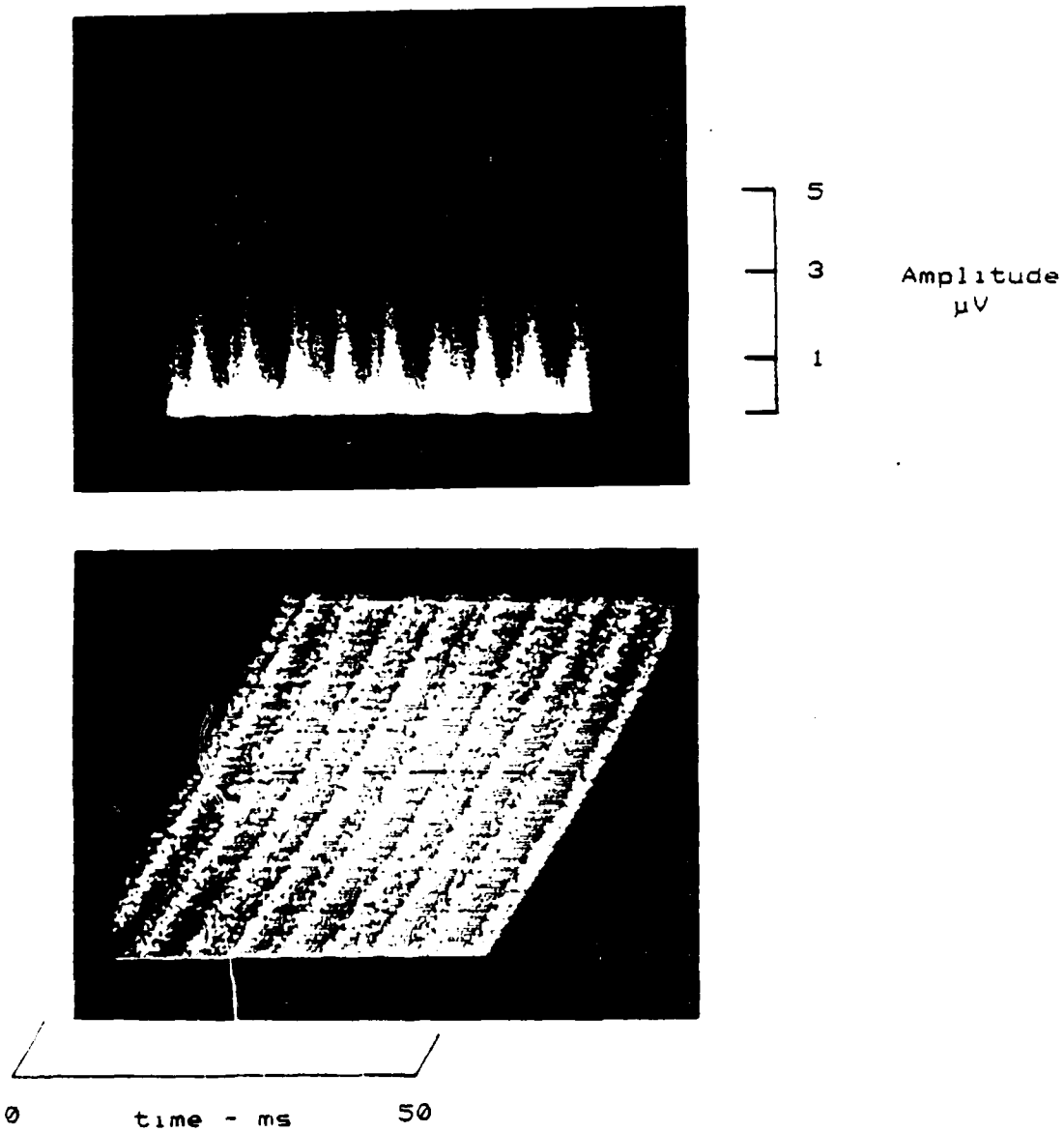

Figure 26. Corona Noise as shown on 3-Axis Display

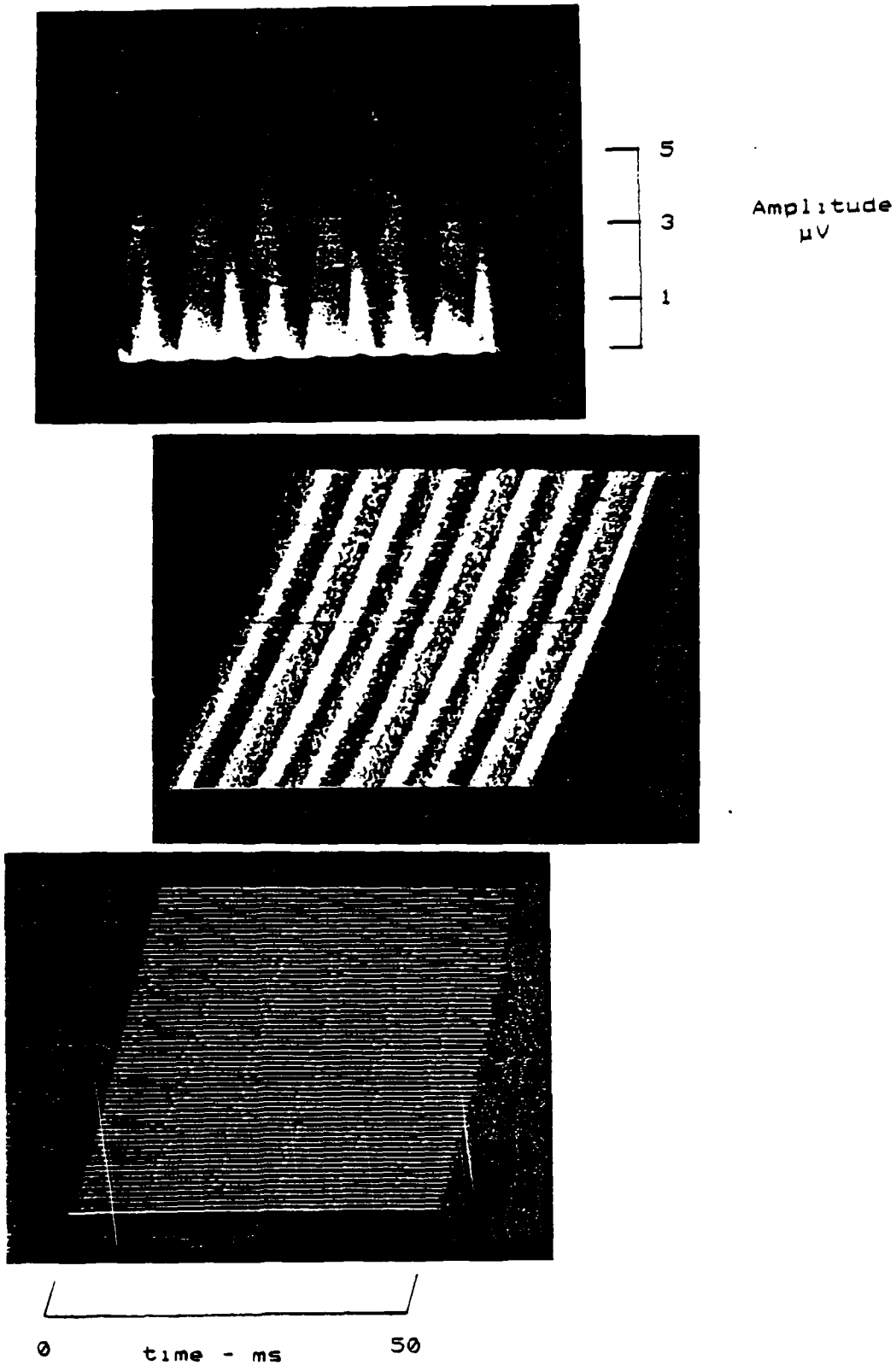

Figure 27. Gap and Corona Noise

about 3.5 μV. The two lower pictures are of identical data with the threshold varied to emphasize each noise type. The lower picture has the threshold set at about 3 μV eliminating the 180-Hz corona noise and showing the gap noise process occurring at a 120-Hz rate. This corresponds to a gap noise source sparking on the positive and negative half-cycle of a single phase of a 3 phase line. When the threshold is lowered to about 1 μV, the 180-Hz corona noise dominates as seen in the middle picture of Fig. 27. This phenomenon is due to corona discharge on the negative half-cycle of each phase of a 3-phase system. Without the ability to examine the time- and frequency-domain behavior of the noise using a scanning analyzer and 3-Axis display, it would be very difficult to differentiate between gap and corona noise and make accurate measurements of either.

Fig. 28 illustrates corona noise with different phase-to-phase characteristics. In this example the noise power due to the corona is unequal from phase to phase. The noise occurring on the dominant phase is approximately twice the peak voltage of the phase with the lowest amplitude.

D. CORONA NOISE MODEL

Based on the above observations of the demodulated envelope of corona noise, a specific filtered impulse model based on Eqn. 2-18 will be developed. This model is similar to models used in synthetic hydrology to account for

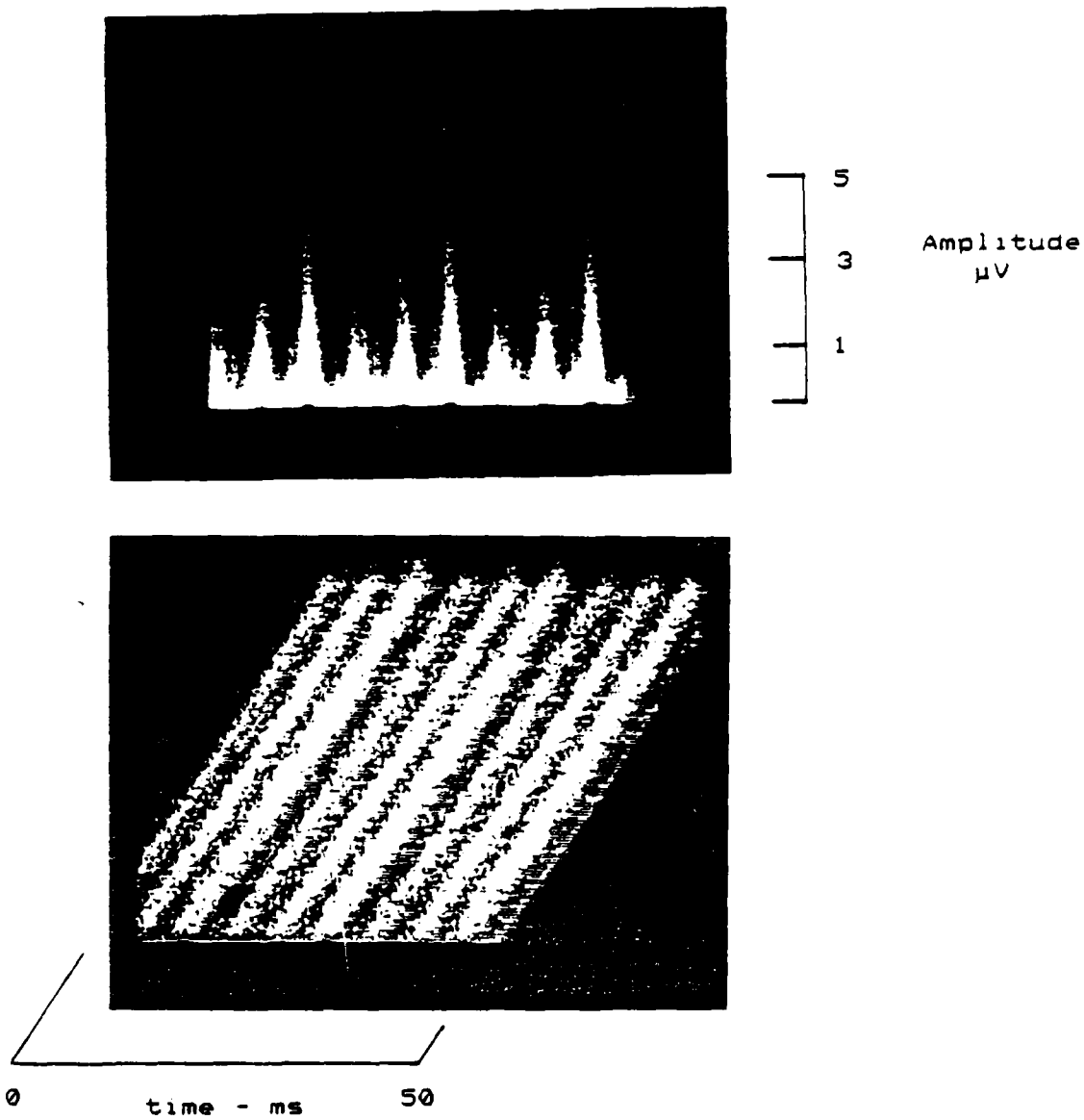

Figure 28. Corona Noise - Uneven Phase to Phase

seasonal variations in streamflow data [Ref. 39]. Assuming no Gaussian noise component, a lowpass complex filtered noise process can be written

$$n(t) = \sum_{i=1}^{N(t)} a_i e^{-j\theta_i} \delta(t-t_i). \tag{4-1}$$

Since corona noise is a high density process, the envelope cannot be simply defined as in Eqn. 2-22 since the response of the filter to adjacent pulses will overlap. To circumvent this difficulty it will be assumed that the envelope of n(t) can be modeled by

$$e(t) = \sum_{i=1}^{N(t)} a_i g(t-t_i) \tag{4-2}$$

where both e(t) and g(t) are real, positive and g(t) depends on h(t) and the process intensity.

The assumptions to define the model are as follows;

1. The rate parameter for the counting function N(t) is periodically modulated at frequency ω_0 and will be approximated by a finite number of terms in a Fourier series.

2. The amplitude distribution of successive pulses given by the a_i's are independent and identically distributed with density function p(a).

3. The start time of the periodic modulation is uniformly distributed over the period T_0 where $T_0 = 1/\omega_0$.

Assumption one is motivated by the periodicity observed in the data. In most cases the fundamental period, ω_0 will be 180 Hz. If the noise is more dominant on one phase of the line, as shown in Fig. 28, then 60 Hz components of the

noise will exist and for a more accurate model the fundamental period would be 60 Hz. The rate parameter is given by

$$\lambda(t) = \sum_{n=0}^{N_T} a_n \cos(\omega_0 nt) \qquad (4\text{-}3)$$

where N_T is the order at which the Fourier series is truncated.

The second assumption is arbitrary in terms of the distribution function chosen for the impulses. It is obvious that random impulse amplitudes are being generated by the cumulative effect of the corona noise sources. However, it would be difficult to accurately fit a density function to the data due to the time varying nature of the process. The independence of the amplitude bursts is also conjecture but facilitates the development of a tractable model. The Rayleigh density function is

$$\begin{aligned} p(a) &= (a/\beta)e^{-a^2/2\beta} && a \geq 0 \\ &= 0 && a < 0 \end{aligned} \qquad (4\text{-}4)$$

and was picked to model the random amplitudes. It is analytically tractable and can be justified by assuming the quadrature components of the impulse amplitudes are independent Gaussian events.

The final assumption is made because in most interference scenarios, the power line noise process will not be synchronized to the process being interfered with.

Thus the phase will be effectively randomized over one fundamental period. In some of the observations of corona noise (see Figs. 26-28) this assumption was clearly violated and the instrumentation was intentionally synchronized to the power line for clarity of presentation.

The model could be further generalized by allowing the amplitude density function p(a) to be a periodic function of time, p(a,t) independent of the rate parameter. This added complexity would make the model more accurate; however, more parameters would have to be estimated.

The above assumptions classify this process as a compound non-homogeneous filtered Poisson process. A convenient tool to study these processes is the cumulant generating function [Ref. 41:p. 117]

$$\psi(s) = \ln\{E[e^{se(t)}]\} \tag{4-5}$$

where ln is the natural logarithm. The joint cumulant generating function is

$$\psi(s_1, s_2) = \ln\{ E[e^{s_1 e(t_1) + s_2 e(t_2)}]\}. \tag{4-6}$$

For the noise process defined by the first two assumptions, it is shown in Appendix F that

$$\psi(s) = \int_{-\infty}^{\infty} p(a) \int_{-\infty}^{\infty} \lambda(\alpha) \left[e^{sah(t-\alpha)} - 1\right] d\alpha da \tag{4-7}$$

and

$$\psi(s_1, s_2) = \int_{-\infty}^{\infty} p(a) \int_{-\infty}^{\infty} \lambda(\alpha) \left[e^{s_1 a h(t_1 - \alpha) + s_2 a h(t_2 - \alpha)} - 1 \right] d\alpha da. \tag{4-8}$$

From the properties of the cumulant generating functions it can be shown that

$$E[e(t)] = \psi'(0), \tag{4-9}$$

$$Var[e(t)] = \psi''(0) \tag{4-10}$$

and

$$Cov(t_1, t_2) = \frac{\partial^2 \psi(0,0)}{\partial s_1 \partial s_2} . \tag{4-11}$$

It is straightforward to show that

$$E[e(t)] = E[a] \int_{-\infty}^{\infty} \sum_{n=1}^{N_T} a_n \cos(\omega_0 n\alpha) h(t-\alpha) d\alpha, \tag{4-12}$$

$$Var[e(t)] = E[a^2] \int_{-\infty}^{\infty} \sum_{n=1}^{N_T} a_n \cos(\omega_0 n\alpha) h^2(t-\alpha) d\alpha \tag{4-13}$$

and

$$Cov[t_1, t_2] = E[a^2] \int_{-\infty}^{\infty} \sum_{n=1}^{N_T} a_n \cos(\omega_0 n\alpha) h(t_1 - \alpha) h(t_2 - \alpha) d\alpha. \tag{4-14}$$

The autocorrelation function can be found in terms of the above functions as

$$R(t_1, t_2) = Cov(t_1, t_2) + E[e(t_1)]E[e(t_2)]. \tag{4-15}$$

The above equations, prior to the application of assumption 3, define a wide sense cyclostationary process [Ref. 40] where

$$E[e(t + mT_0)] = E[e(t)] \tag{4-16}$$

and

$$R(t_1 + mT_0, t_2 + mT_0) = R(t_1, t_2). \tag{4-17}$$

The statistics of the process are invariant to a shift of the time origin by integral multiples of the period, T_0. This characterization is particularly appropriate when the process is observed in synchronization with the fundamental power line frequency.

When assumption 3 is applied, the process start times are randomly shifted over one period, the process becomes wide sense stationary and the mean and autocorrelation become

$$\bar{E}[n(t)] = \frac{1}{T_0} \int_0^{T_0} E[n(t)]\, dt \tag{4-18}$$

and

$$\bar{R}(\tau) = \frac{1}{T_0} \int_0^{T_0} R(t+\tau, t)\, dt. \tag{4-19}$$

The power spectral density (PSD) of the process is

$$S(\omega) = \int_{-\infty}^{\infty} \bar{R}(\tau) e^{-j\omega\tau}\, d\tau. \tag{4-20}$$

The following algorithm is an example of how the noise process specified above can be digitally generated. For the algorithm specified below; N_0 is the number of samples in one period T_0, $\{n_i\}$ is the real sequence to be generated, i is the index variable for the sequence and j and k are dummy index variables.

1. $i = 0$
2. $n(i) = 0$
3. Generate a Rayleigh random variable, R, with parameter β and set $n(i) = n(i) + R$
4. Set intensity $\lambda = \sum_{n=0}^{N_T} a_n \cos(\omega_0 ni/N_0)$
5. Generate a Poisson random variable, P, and set $j = \text{trunc}(P/\lambda + .5)$
6. Set $n(k) = 0$ for $k = i + 1$ to j
7. $i = j$
8. Go to Step 3

The above algorithm will continuously generate a modulated Poisson impulse process that may be digitally filtered concurrent with the impulse process generation or subsequent to the generation of a complete time record.

Two additional points should be noted. A number of impulse amplitudes could stack up on each other if the truncation operation returns a zero value. This corresponds to the physical case where multiple impulses occur and are unresolved within one sampling period. Before a record of noise samples generated by the above process is used a

truncated uniform random variable between $\emptyset$ and N_o, the sampled period, should be subtracted from i. This ensures that the start time is uniformly distributed over one period.

E. PARAMETER ESTIMATION

Having specified the model, the task of determining the parameters for a given interference scenario remains. The parameters to be determined are the $\{a_n\}$, the Fourier Series coefficients of the periodically varying rate function and the β parameter in the probability density function of impulse amplitudes. As an example, the parameters for the noise process described in the time domain observations Section will be determined.

One method of estimating these parameters is by considering the predicted mean and variance of the process as given by Eqns. 4-12 and 4-13 and matching these parameters to the data. In order to do this analysis, the corona source has to be observed as a cyclostationary process. This requires synchronizing the data collection instrumentation to the line frequency so that the same point in each cycle can be examined. This is difficult to do for field measurements.

Another option for determining the model parameters is the predicted stationary mean, variance and PSD or auto-correlation function. The PSD as defined in Eqn. 4-20 is stationary so no line synchronization is required and

instrumentation is readily available to make a periodogram estimate of the PSD.

For the measurements taken in this research, the lowpass impulse response of the filter was approximately

$$h(t) = (\alpha/\pi)e^{-\alpha t^2} \qquad t \geq 0$$
$$= 0 \qquad t < 0. \qquad (4\text{-}21)$$

With the above definition the filter has unity gain at ω equal to 0. The effective filter response $g(t)$ was approximated by $h(t)$.

In Appendix G it is shown that

$$E[e(t)] \approx (\beta\pi/2)^{1/2} \sum_{n=0}^{N_T} e^{\frac{-\omega_0^2 n^2}{4\alpha}} a_n \cos(\omega_0 nt) \qquad (4\text{-}22)$$

where $(\pi\beta/2)^{1/2}$ is the first moment of $p(a)$, the probability density function of the impulse amplitudes. The stationary mean is

$$E[e(t)] \approx (\beta\pi/2)^{1/2} a_0 . \qquad (4\text{-}23)$$

The covariance of $e(t)$ is shown to be

$$\mathrm{Cov}(t_1, t_2) = (\alpha/\pi)2\beta e^{-\alpha(t_1-t_2)^2/2} \int_{|t_1-t_2|}^{\infty} \sum_{n=0}^{N_T} a_n \cos(\omega_0 n(u+(t_1+t_2)/2)) e^{-2\alpha u^2} du. \qquad (4\text{-}24)$$

Using Eqns. 4-15 and 4-19 and substituting the above results, the stationary autocorrelation function is

$$\bar{R}(\tau) = 2\beta \left[e^{-\alpha\tau^2/2} a_0 (\alpha/8\pi)^{1/2} + (1/4) a_0^2 + (1/8) \sum_{n=1}^{N_T} e^{\frac{-\omega_0^2 n^2}{4\alpha}} a_0^2 \cos(\omega_0 n\tau) \right]. \tag{4-25}$$

Taking the Fourier transform, the resulting PSD is

$$S(\omega) = 2\beta \left[(2)^{1/2} a_0 e^{-\omega^2/2\alpha} + (\pi/2) a_0^2 \delta(\omega) + (\pi/8) \sum_{n=1}^{N_T} e^{\frac{-\omega_0^2 n^2}{4\alpha}} a_n^2 \delta(\omega \pm n\omega_0) \right]. \tag{4-26}$$

The terms in the PSD in order are; (1) a white noise term multiplied by the frequency response of the Gaussian filter, (2) an impulse at $\omega = 0$ from the mean value of the process and (3) periodic components at harmonics of 180 Hz due to the modulation of the driving function.

To estimate the model parameters, the sample mean and mean square estimates were used in conjunction with Eqns. 4-23 and 4-24 to solve for a_0 and β. The periodogram estimate of the spectrum was used to determine the magnitude of the a_1 and a_2 co-efficients. The Fourier series was truncated

AD-A174 140 POWER LINE NOISE MODELS AND ENERGY DETECTION IN THE HIGH FREQUENCY RADIO BAND(U) NAVAL POSTGRADUATE SCHOOL MONTEREY CA J M O'DWYER 20 JUN 86 NPS62-86-004 2/2

UNCLASSIFIED F/G 10/2 NL

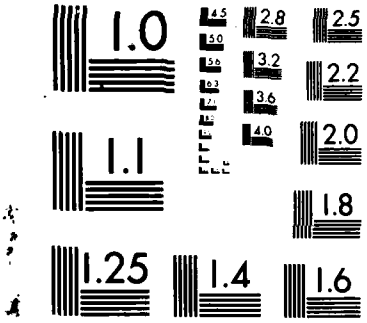

MICROCOPY RESOLUTION TEST CHART
NATIONAL BUREAU OF STANDARDS-1963-A

at $N_T = 2$ since no higher order terms were observed in Fig. 25. For the data taken in Fig. 24 and 25 the parameter α in Eqn. 4-21 was 7.11×10^{8}. Table IV lists the parameters of the assumed model.

Coefficient of Gaussian Filter	α	7.11×10^{8}
Amplitude Density Parameter	β	1.58×10^{21}
Fourier Co-efficients of Rate Function	a_0	22,900
	a_1	5,700
	a_2	2,500

TABLE IV

These parameters were inserted into the algorithm described previously for generating corona noise, and five cycles of the synthetic noise are shown in Fig. 29. Comparing the actual noise in Fig. 24 and the generated noise in Fig. 29, the generated noise correctly models the random, impulsive character of the actual noise and also its periodicity. The synthetic noise, however, does not incor-porate the constant bias above the 0 level seen in the actual noise.

F. SUMMARY

This chapter has presented a detailed analysis of the time- and frequency-domain behavior of corona noise. A model for synthetic corona noise was postulated based on a filtered non-homogeneous Poisson process. A methodology for

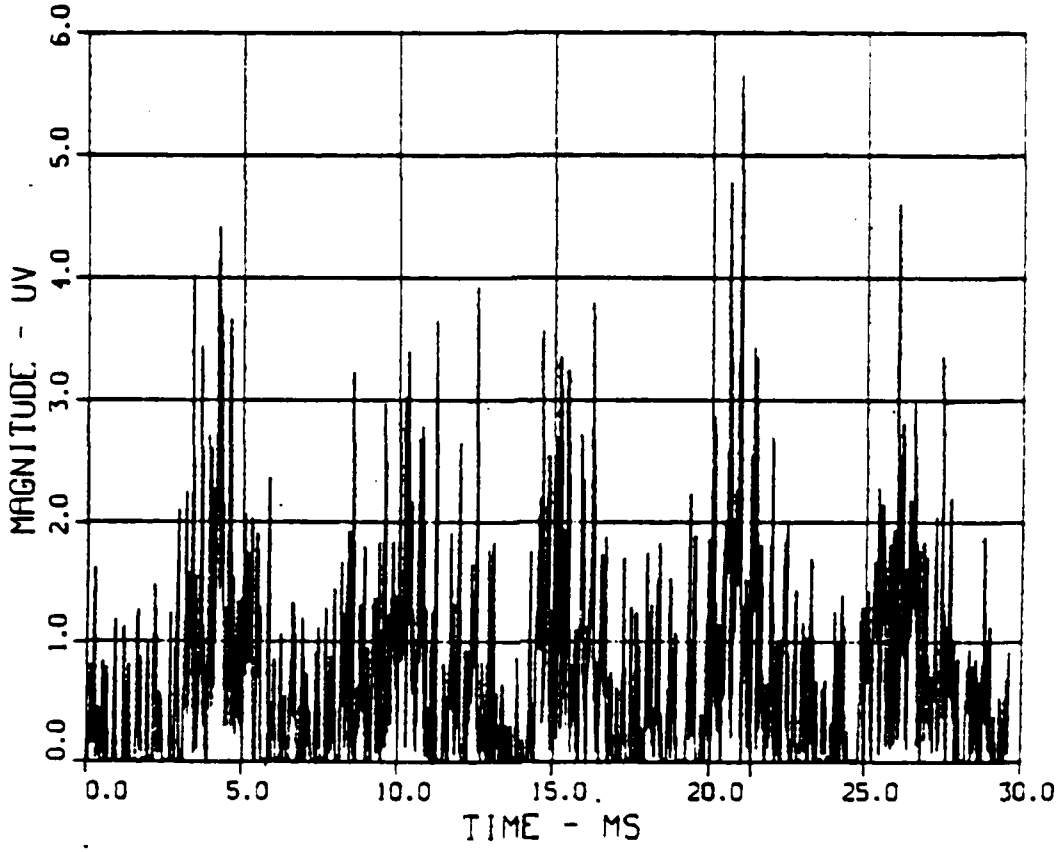

Figure 29. Synthetic Corona

estimating the model parameters was developed. The advantage of this model over previous work is that it allows an accurate representation of the time-domain behavior of corona. The disadvantage of this model is that it is scenario dependent and for each interference situation a new set of model parameters must be specified. One limitation was introduced into the model by the assumption leading to Eqn. 4-2. The lowpass equivalent filter is a function of the bandpass filter and the process intensity, and

consequently, the model is not as general or as accurate as the gap noise model.

V. ENERGY DETECTION RECEIVERS

A. INTRODUCTION

Energy detection receivers in the high frequency (HF) radio band operate in an impulsive radio noise environment. To predict and improve the performance of energy detection receivers, accurate models of the signal and noise environment must be used. The noise models developed in earlier Chapters will be used to simulate atmospheric and man-made radio noise environments. Two types of energy detection receivers will be considered: a fast Fourier transform (FFT) processing system and a compressive receiver. To improve the performance of these receivers the concept of the locally optimum receiver is introduced to suggest a robust post-detection processor.

B. ENERGY DETECTION

The energy detector receiver measures the energy in a signal over a specific time interval. For this chapter we will consider the signal to be a modulated sinusoid, of unknown frequency at the receiver. The signal is then represented as

$$s(t) = A\cos(\omega_o t + \theta(t)) \qquad (5\text{-}1)$$

where A and ω_o are random variables and $\theta(t)$ is a slowly varying function so that the signal power is effectively confined to a narrow bandwidth B.

Defining the problem as a hypothesis test

H_0 : $x(t) = n(t)$ noise alone

H_1 : $x(t) = n(t) + s(t)$ signal plus noise. (5-2)

The well known energy detection receiver [Ref. 42] uses t_{ED}, the received energy as the test statistic such that

$$\text{Under } H_0: \quad t_{ED} = \int_0^T n^2(t)dt$$

$$\text{Under } H_1: \quad t_{ED} = \int_0^T [n(t) + s(t)]^2 dt. \qquad (5\text{-}2)$$

For a sampled bandpass process the test statistic is

$$H_0: \quad t_{ED} = \sum_{i=1}^{N} [n_{c_i}^2 + n_{s_i}^2]$$

$$H_1: \quad t_{ED} = \sum_{i=1}^{N} [n_{c_i} + s_{c_i}]^2 + [n_{s_i} + s_{s_i}]^2 \qquad (5\text{-}3)$$

and

$$x_{c_i} = n_{c_i} + s_{c_i} \quad \text{or} \quad x_{c_i} = n_{c_i}$$

and likewise for the quadrature component.

Fig. 30 shows the block diagram of a receiver that calculates this statistic. This receiver will be called a square and sum receiver. The square and sum receiver is the optimum receiver for detecting random phase signals in Gaussian noise at small signal levels. At large signal to noise ratios (SNR) this detector is very close to optimum

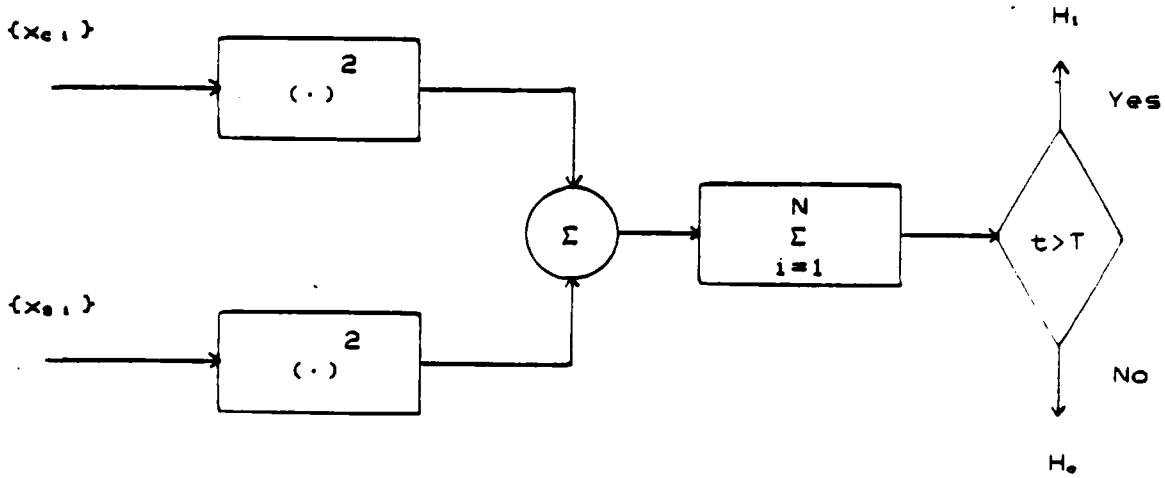

Figure 30. Square and Sum Receiver

[Ref. 9:p. 370]. When N = BT and the signal is sampled at the Nyquist rate, the test statistic is the energy in the signal in a period T.

When it is desired to implement the receiver shown in Fig. 30 over a wide frequency band relative to the target signal modulation bandwidth B, a number of options may be pursued. The channelized receiver approach in which an independent receiver operates at each frequency will often be too expensive. Two other possible methods for generating the test statistic are; (1) a compressive receiver as a spectrum analyzer [Ref. 43] and (2) a fast Fourier transform (FFT) signal processor.

It has been shown that an FFT signal processor exactly implements the test statistic given in Eqn. 5-3 for the assumed signal in a single FFT filter [Ref. 44]. Whether successive samples will be independent or not depends on the number of transforms per second relative to the signal bandwidth B. If the sample interval is greater than 1/B then successive samples will be independent.

In the compressive receiver, shown in Fig. 31, a fast sweeping local oscillator linearly scans the band of interest. Any narrow bandwidth signal in the band will appear at the mixer output as a linear, frequency modulated (FM), chirp signal. This chirp signal is passed through a weighting filter to reduce sidelobes and into a dispersive delay line (DDL) which is matched to the inverse of the linear FM sweep. The output of the DDL is envelope detected and, when referred to the sweep time, it provides an estimate of the spectrum of the input signal. It is easily shown that for a sinusoid, the detector output is proportional to the signal magnitude. Thus, the compressive receiver approximates the square root of the ith value of the test statistic in Eqn. 5-3. The samples will be independent if the scan revisit time is greater than 1/B.

C. SQUARE AND SUM RECEIVER

In this Section the energy detection performance of the square and sum receiver, shown in Fig. 30, will be examined

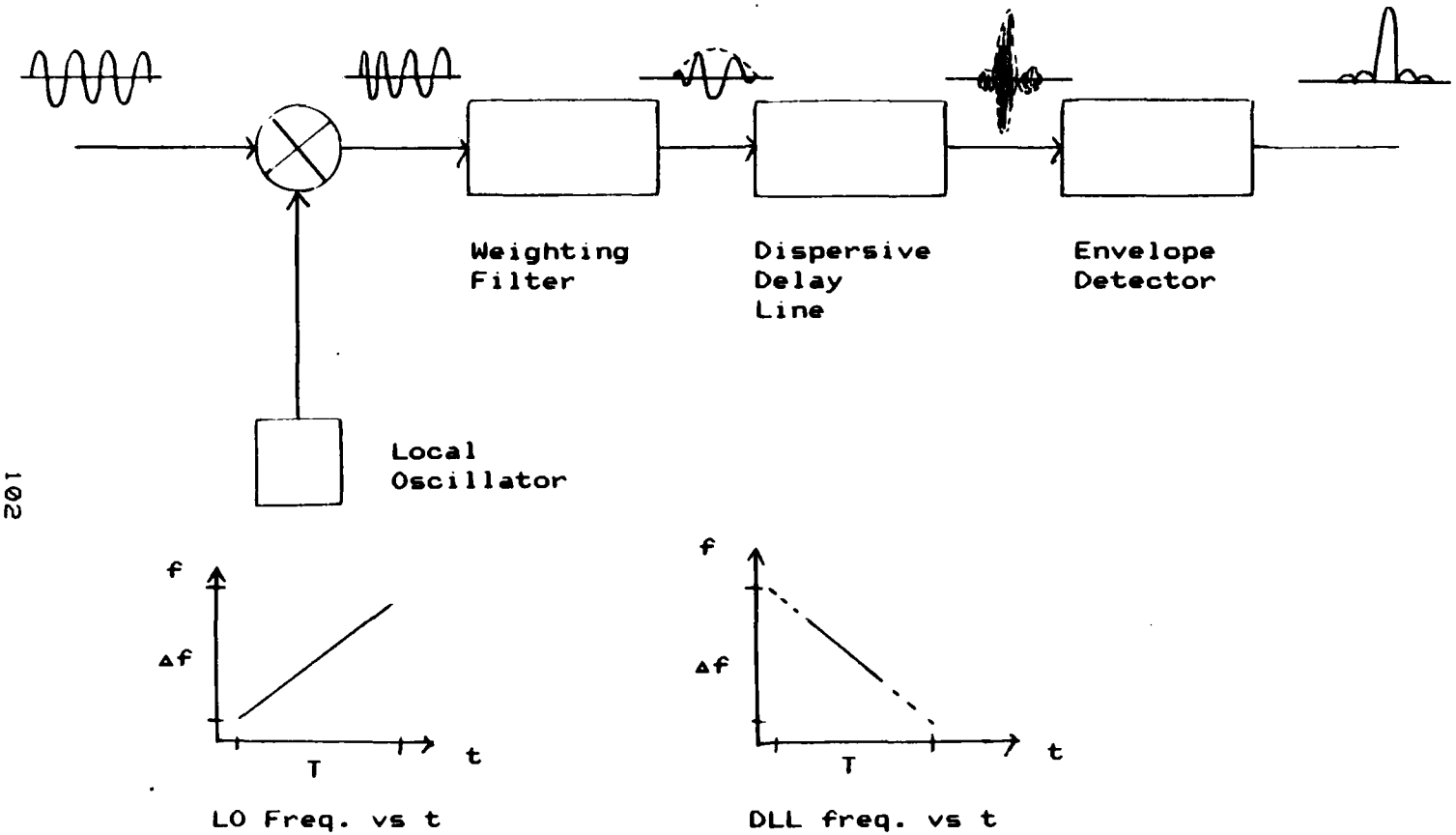

Figure 31. Block Diagram of Compressive Receiver

as the noise statistics depart from a Gaussian distribution. The square and sum receiver, which is optimum for small signals in Gaussian noise, will be used as the reference receiver so that the performance of improved receiver structures may be evaluated.

The number of samples, N, chosen for this study was 10. This is a small sample size and, for impulsive noise, the resulting test statistic will have a distinctly non-Gaussian distribution. In Fig. 32 the probability of false alarm (P_{FA}) is plotted for unit root-mean-square (RMS) Gaussian noise and the Hall models with V_D equal to 2.1, 3, 5 and 12. (see Table II). The normalized threshold is in reference to the unit RMS power of the noise.

A Monte Carlo simulation technique was used to obtain the data for the plot. Since the data are independent Bernoulli trials with a large number of trials, the normal approximation to the binomial was used to determine the confidence interval. For estimates of P_{FA} greater than 5×10^{-3} with 20,000 trials, the true value of P_{FA} will be within 20 percent of the estimate with a confidence of 95 percent [Ref. 55:p. 282]. The noise samples were generated using the inverse method [Ref. 45:p. 951] and the inverse cumulative distribution functions (CDFs) in Table I.

In Fig. 33 the probability of detection (P_D) curves are plotted for P_{FA} equal to 1×10^{-8}. A rejection method [Ref. 45:p. 952] was used to generate the random deviates since

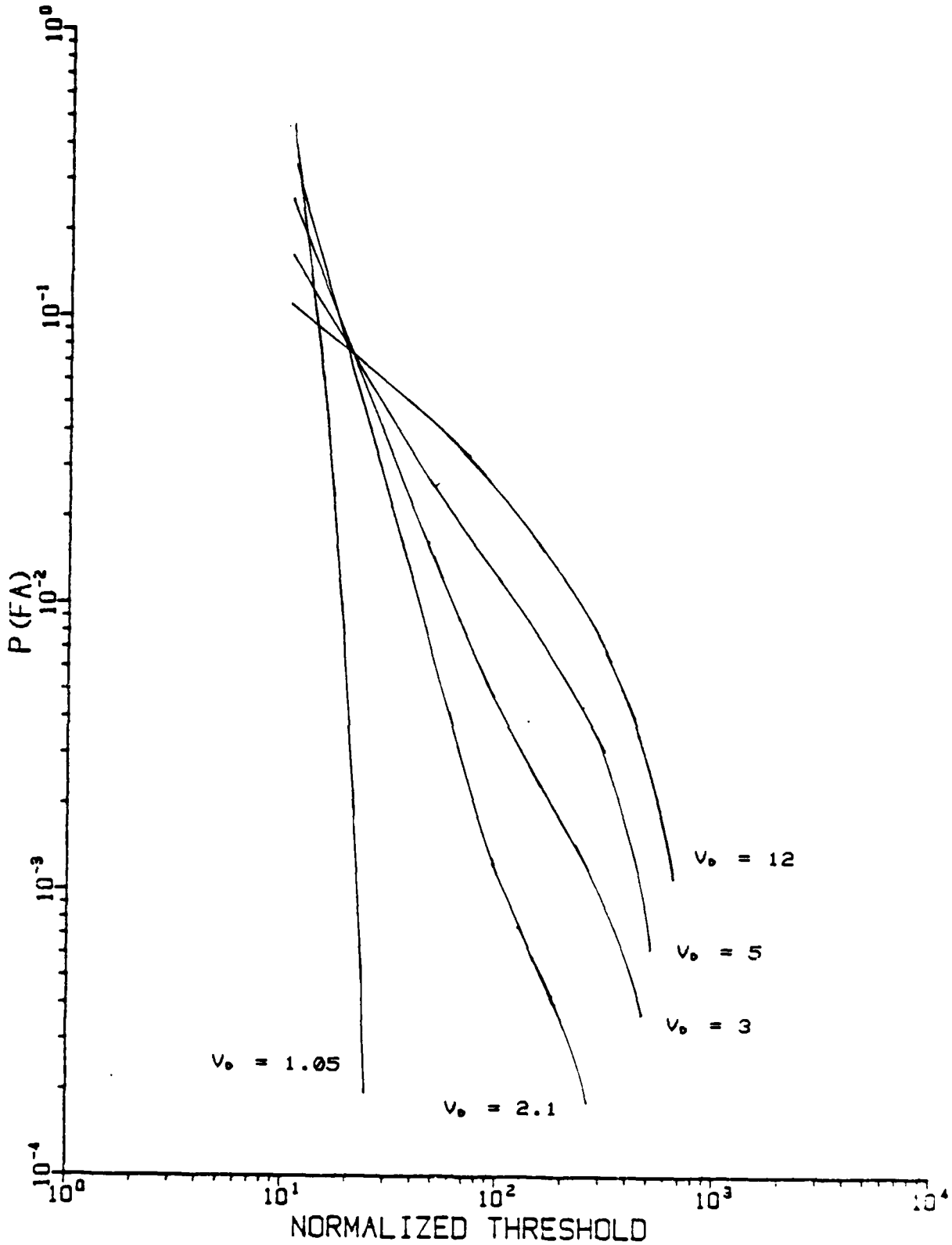

Figure 32. P_{FA} for Square and Sum Receiver in Gauss and Hall Noise

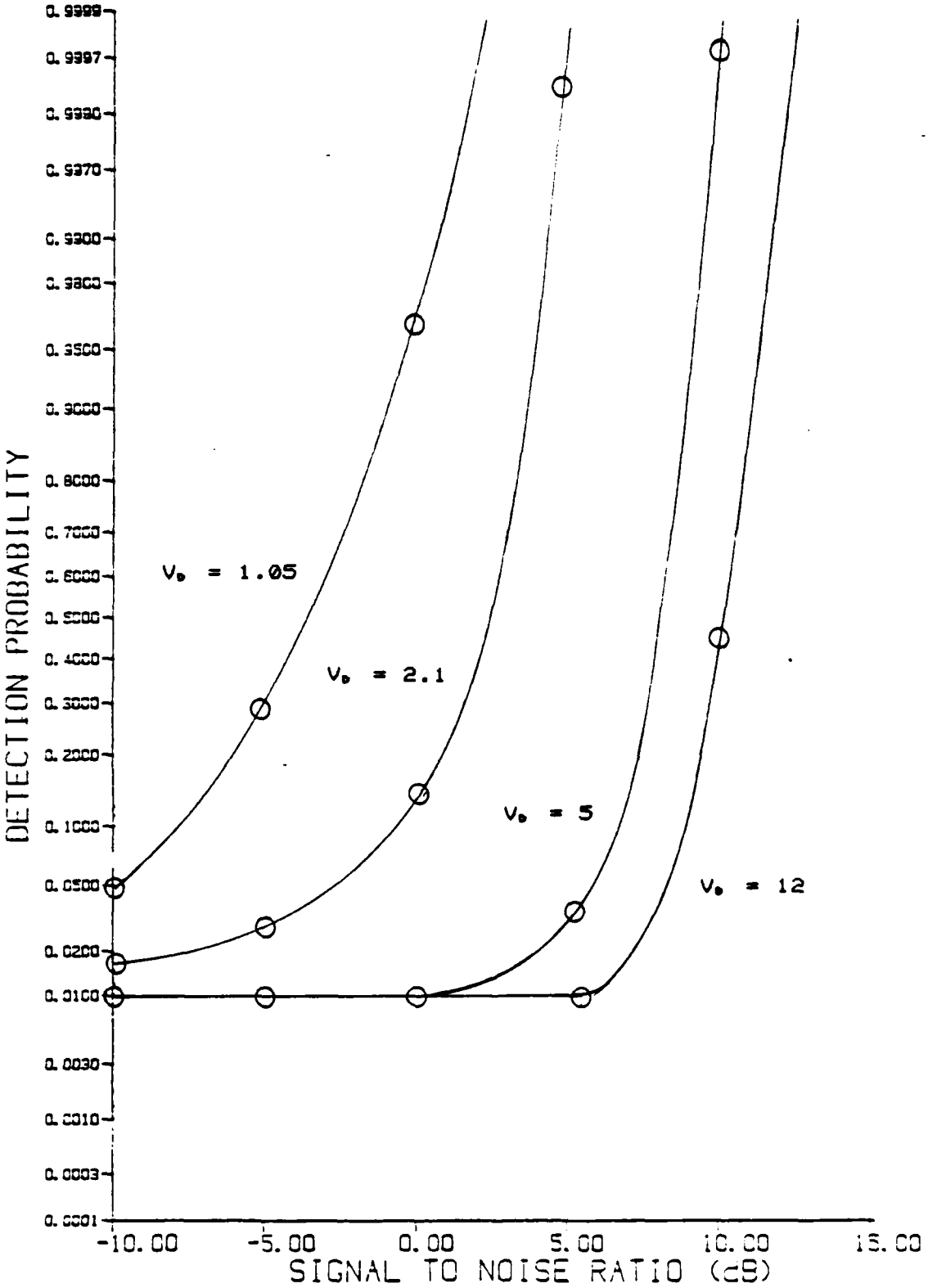

Figure 33. P_D for Square and Sum Receiver in Gauss and Hall Noise as Function of V_b for $P_{FA} = 1 \times 10^{-8}$

the CDFs of the signal plus noise densities were not found. The P_D is plotted as a function of SNR for the same parametric conditions as used in Fig. 32. As anticipated the P_D decreases dramatically as the noise becomes more impulsive. In the case where V_D equals 12, the P_D decreases from greater than 99 percent to 1 percent at a 5 dB SNR for the same P_{FA}.

A receiver that is optimum in Gaussian noise suffers a major degradation when the noise statistics become non-Gaussian. One possible approach to improving the performance is to design a receiver that is based on the statistical parameters of the noise. A parametric approach will be discussed in the next section.

D. LOCALLY OPTIMUM RECEIVER

The concept of a locally optimum receiver provides a general methodology for nonlinear receiver design in the presence of non-Gaussian noise. The approach is to determine a receiver structure that is optimized for the difficult small signal case and then examine, and if necessary, modify the structure for the large signal case. In this Section the locally optimum receiver for energy detection in the presence of Hall type impulsive noise will be determined under the assumption of weak signal levels. Previous work has considered known signal detection in Cauchy noise which is related to one of the Hall models

[Ref. 46]. After optimizing the design for weak signal levels the performance of the receiver will be examined for moderate to large signal levels. The receiver structure will be parametric; that is it will depend on the noise density function parameters.

To illustrate the method for deriving the locally optimum receiver, consider the following binary hypotheses test. We are given a sequence, x_i, of N samples. Under the null hypotheses H_0, we assume that the sequence consists only of independent and identically distributed noise observations with a common density p(n). Under the alternative hypothesis H_1, we assume that the sequence consists of an additive mixture of a small signal and noise. *The problem may be stated as*

H_0: $x_i = n_i$ noise alone

H_1: $x_i = n_i + As_i$ signal plus noise $i = 1,..,N$

with A an unknown small amplitude.

The optimum receiver, in terms of maximizing the probability of detection while keeping the probability of false alarm below a certain level is given by the Neyman-Pearson lemma. This receiver compares the likelihood ratio test statistic to a threshold which is chosen to achieve the desired probability of false alarm.

The liklihood ratio test is

$$\Lambda(\underline{x};A) = \frac{p_0(\underline{x}|H_0)}{p_1(\underline{x}|H_1)} \quad \begin{cases} > T \text{ decide } H_0, \text{ or} \\ < T \text{ decide } H_1 \end{cases} \qquad (5\text{-}4)$$

where $p_0(\underline{x}|H_0)$ and $p_1(\underline{x}|H_1)$ are the probability density functions for the observation vector x under H_0 and H_1 respectively. Since the noise samples are independent and identically distributed, $p_0(\underline{x}|H_0)$ and $p_1(\underline{x}|H_1)$ can be written as products of the univariate noise densities:

$$p_0(\underline{x}) = \prod_{i=1}^{N} p_1(x_i) \tag{5-5}$$

and

$$p_1(\underline{x}) = \prod_{i=1}^{N} p_1(x_i - As_i). \tag{5-6}$$

The test can then be written

$$\Lambda(\underline{x};A) = \frac{\prod_{i=1}^{N} p_1(x_i - As_i)}{\prod_{i=1}^{N} p_1(x_i)} \begin{cases} > T \text{ decide } H_0, \text{ or} \\ < T \text{ decide } H_1. \end{cases} \tag{5-7}$$

In deriving the locally optimum receiver several approaches have been used. Rudnick [Ref. 47] derived a form of the locally optimum receiver by expanding the likelihood ratio in a Taylor series about x and truncating after the second order terms. Capon [Ref. 48] showed that the locally optimum detector maximizes the slope of probability of detection versus signal strength function at the origin and employs a statistic based on the following test

$$t_{LO}(\underline{x}) = \left.\frac{\partial\Lambda(\underline{x};A)}{\partial A}\right|_{A \Rightarrow 0}. \tag{5-8}$$

In Appendix H it is shown that the locally optimum receiver for the detection of a random sinusoid is

$$t'_{LO}(\underline{r}) = \sum_{i=1}^{N} g(r_i) \tag{5-9}$$

where $g(\cdot)$ is the zero-memory nonlinearity (ZMNL) defined below

$$g(r) = \frac{f''(r)}{f(r)} + \frac{f'(r)}{rf(r)} \tag{5-10}$$

and $\underline{r}$ is a vector of envelope samples. The function, $f(r)$, for the Hall model of atmospheric noise discussed in Chapter II is

$$f(r) = \frac{K\gamma^{\theta-1}}{(r^2 + \gamma^2)^{(\theta-1)/2}} \tag{5-11}$$

where K is a constant. From Eqn. 5-10 the ZMNL of the test statistic is

$$g(r) = \frac{(\theta+1)(\theta+3)r^2}{(r^2 + \gamma^2)^2} - \frac{2(\theta+1)}{(r^2 + \gamma^2)}. \tag{5-12}$$

The receiver that implements this test is shown in block diagram form in Fig. 34. The ZMNL's for the unit root-mean-square Hall models (see Table II) parameterized by V_b are shown in Figs. 35 and 36. The ZMNL receiver characteristic for values of V_b equal 2.1, 3, 6, 10 and 14 are plotted.

Recalling that the nonlinearity is optimized for vanishingly small signals the ZMNL characteristic may be

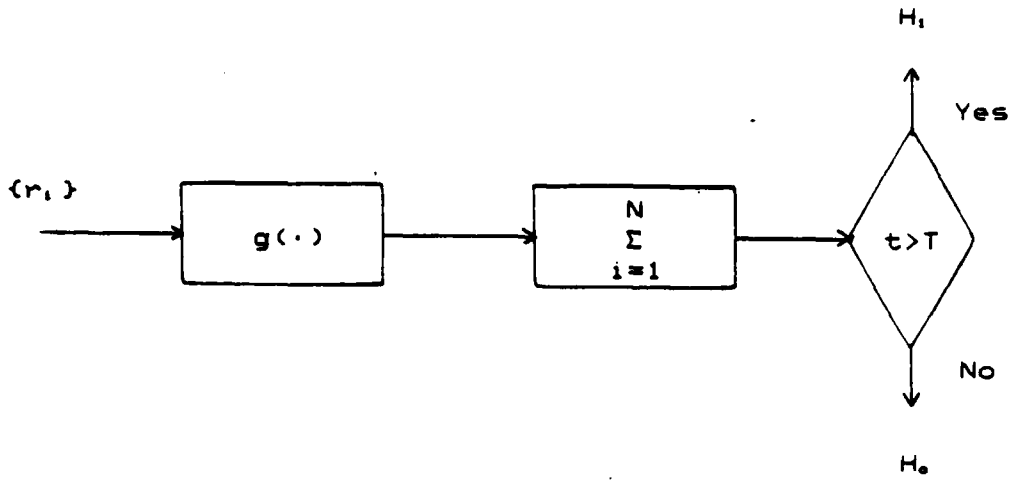

Figure 34. Locally Optimum Receiver for Energy Detection

intuitively analyzed. Small values of the sampled envelope will be given a negative weighting, intermediate values are emphasized and large values of the sampled envelope are effectively nulled. As the noise becomes more impulsive, which corresponds to a larger value of V_b and smaller θ, the above features become more pronounced. This is seen in Fig. 35 where the ZMNL has large negative values that extend off the plot for very small envelope values. The maximum value of the ZMNL occurs at

$$x = \gamma((\theta+5)/(\theta+1))^{1/2} \tag{5-13}$$

and the zero crossing at

$$x = \gamma(2/(\theta+1))^{1/2} . \tag{5-14}$$

Both of the points are proportional to the mean value of the underlying distribution for the same Hall model number.

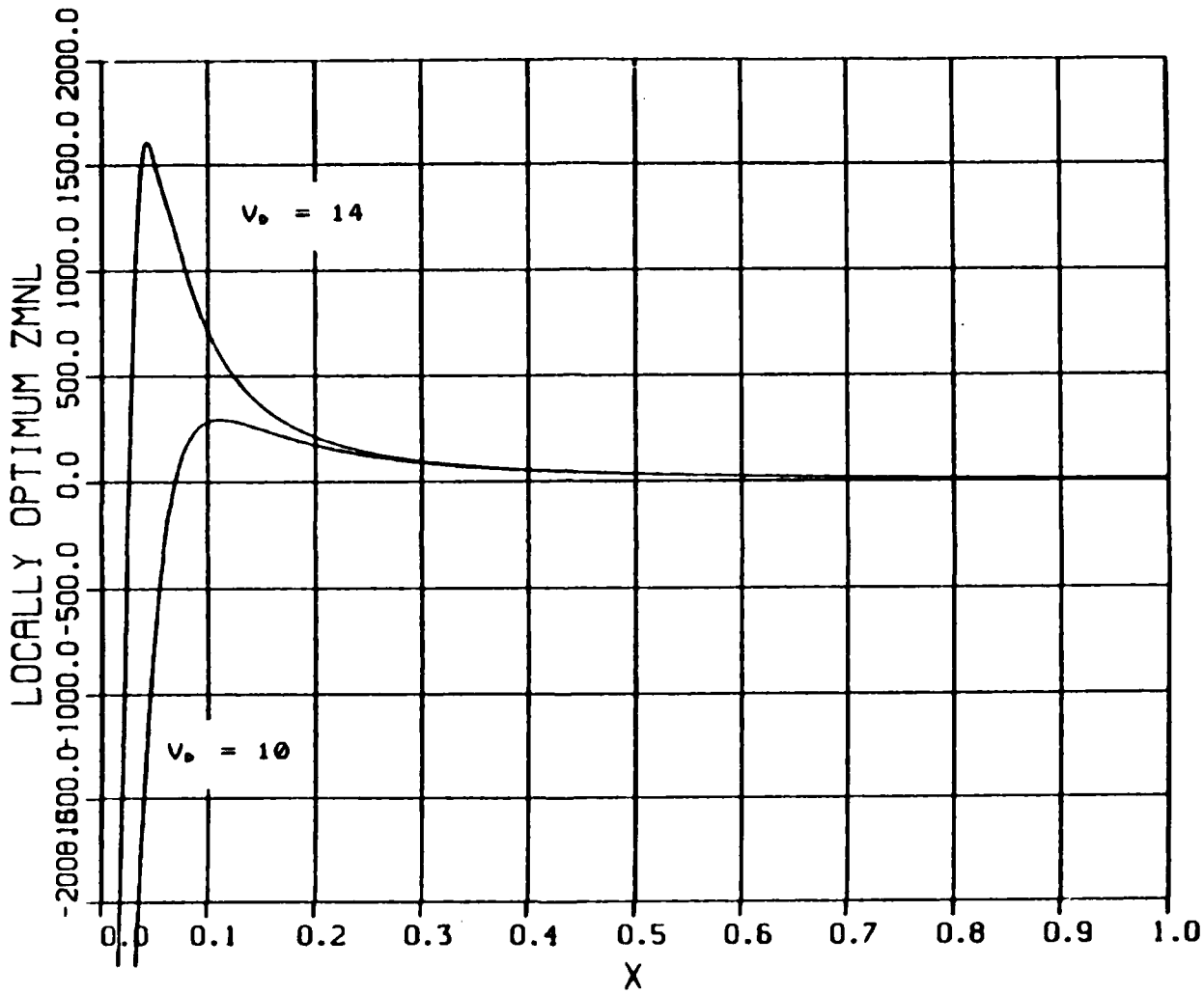

Figure 35. Zero Memory Nonlinearity (ZMNL) for Locally Optimum Receiver in Hall Noise for V_b = 10, 14

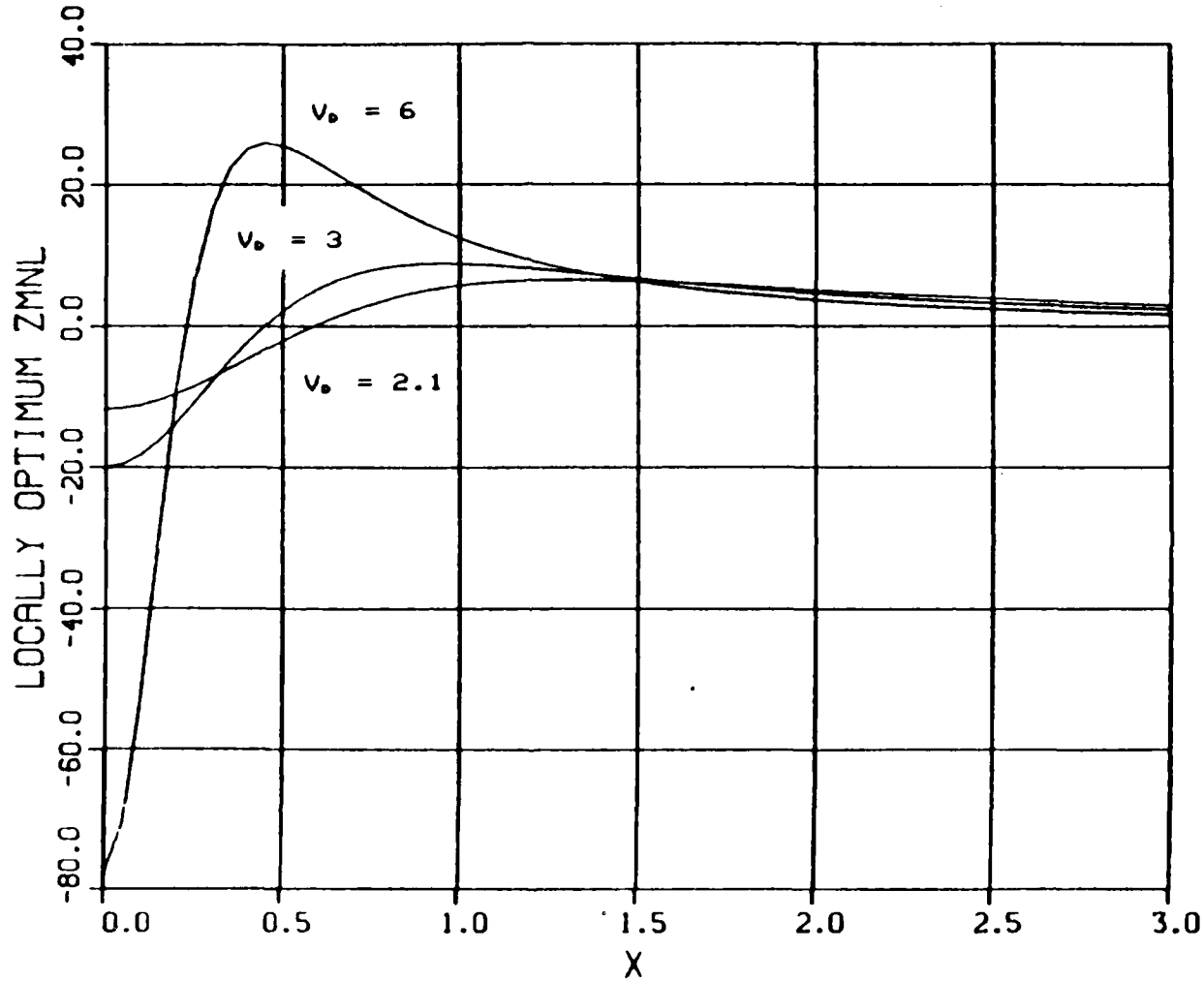

Figure 36. Zero Memory Nonlinearity (ZMNL) for Locally Optimum Receiver in Hall Noise for V_b = 2.1, 3, 6

Fig. 37 is the P_{FA} versus threshold for the locally optimum receiver shown in Fig. 34. The number N of samples is equal to 10. The Hall noise samples are parameterized with the same V_D values used in Fig. 32. The threshold data obtained from this plot was used to generate the P_D curves shown in Fig. 38. The only complete data set was obtained for the Hall2 case with V_D equal to 2.1. Some data was obtained for V_D equal to 5. The peaks in P_D for the more impulsive noise occur at smaller SNR levels, not shown on the plot. The data points are plotted on the graph since the dashed curves only approximate the true values.

It can be seen that the locally optimum receiver does improve the P_D (for the same P_{FA}) in the small signal case. In comparing the values with Fig. 33 for V_D equal to 2.1 the locally optimum receiver has a performance better than the square and sum receiver from -10 dB to 7 dB SNR. Above 7 dB SNR, the P_D for the locally optimum receiver drops to 0. This is due to the fact that the receiver is optimized for small signals. The Hall2 ZMNL in Fig. 36 shows the reason for this. It peaks at approximately 1.3 times the RMS value of the noise and approaches 0 as the input goes to infinity. This behavior of the ZMNL must be modified to obtain a receiver that will also work in the large signal case. In the next Section a robust receiver structure is proposed that does this. A robust receiver is differentiated from a parametric receiver in that the robust receiver does not

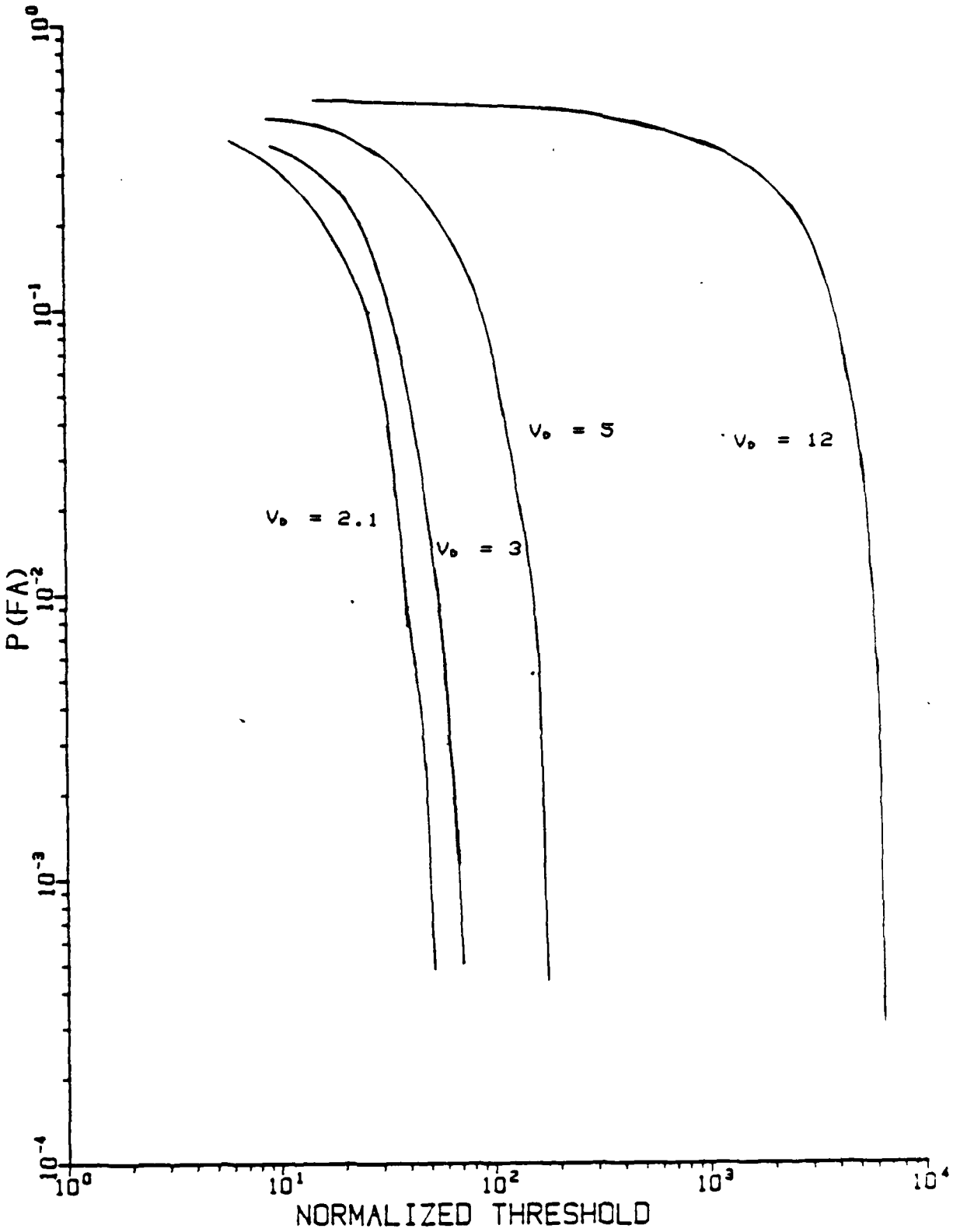

Figure 37. P_{FA} for Locally Optimum Receiver in Hall Noise

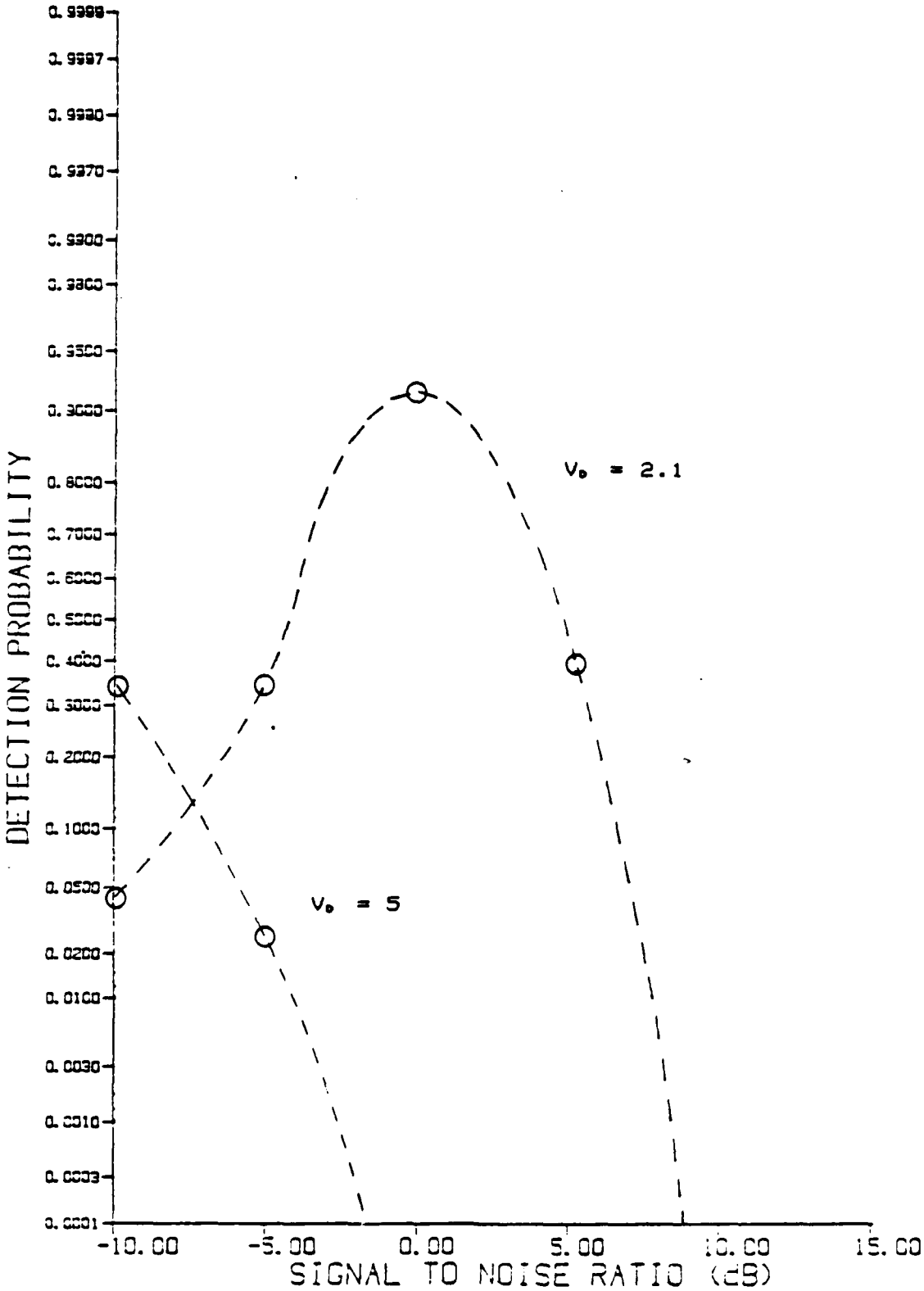

Figure 38. P_D for Locally Optimum Receiver in Hall Noise as Function of V_D for $P_{FA} = 1 \times 10^{-8}$

depend on the parameters of the noise density and it performs well, if suboptimally, over a class or even differing classes of noise densities.

E. ADAPTIVE LIMITER

The ZMNL derived in the previous Section is a relatively complex function. Furthermore, it does not work for large signal levels. In this section we consider a practical implementation of the ZMNL consisting of an adaptive limiter to approximate the ZMNL function with a modification to improve large signal performance. Although the locally optimum receiver was derived for Hall type impulsive noise, if the approximation to it is properly designed, it should show robust performance in the presence of many impulsive noise process.

Examining the P_D curves of the locally optimum receiver for the Hall2 model shows that it provides increased detection performance over the square and sum receiver from -10 dB to 7 dB SNR. Since this region is where the square and sum receiver suffered the worst performance degradation in impulsive noise, the Hall2 ZMNL was chosen to be modified to obtain a robust nonlinearity. The solid curve in Fig. 39 is the Hall2 ZMNL. To correct its performance at large signal levels, the ZMNL was first altered, as shown by the dashed line in Fig. 39, by extending its characteristic straight out from its maximum value. Furthermore, an

equivalent test statistic is obtained if $g'(x)$ is any linear function of $g(x)$ [Ref. 46] so

$$g'(x) = \alpha g(x) + \beta \qquad \alpha \neq 0. \tag{5-15}$$

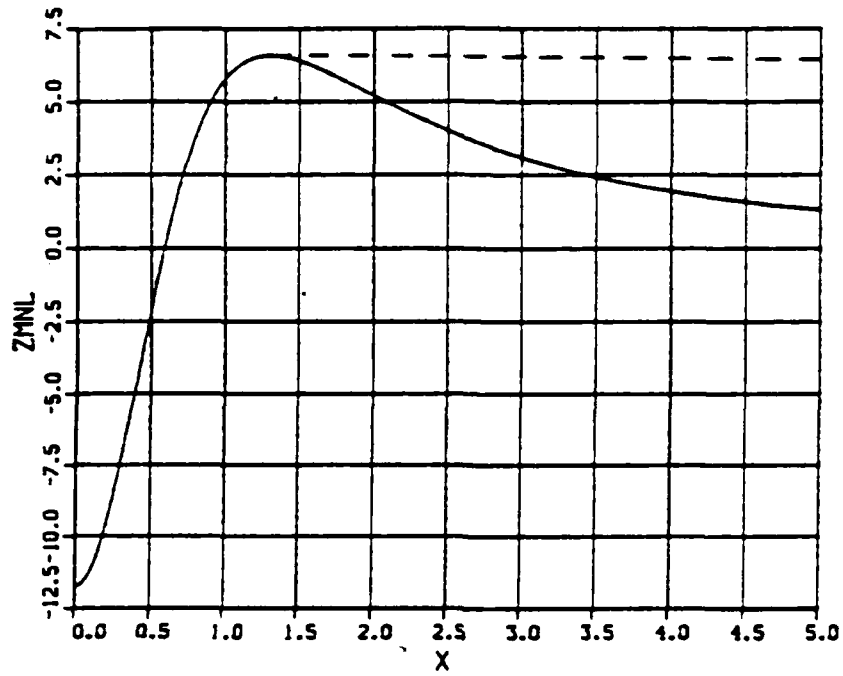

Figure 39. Modification to ZMNL

With suitable parameters α and β, the modified ZMNL is shown in Fig. 40. The level, α, remains to be determined.

Recalling Eqn. 5-13, the argument of the ZMNL characteristic at its maximum value is proportional to the mean value of the Hall distribution for which it was derived (see Table I). For the Hall2 distribution the proportionality constant is approximately 1.6. Therefore, in order to preserve the improvement in P_D in the same SNR region as the Hall2 ZMNL, the limiter level was set to equal 1.6 times the

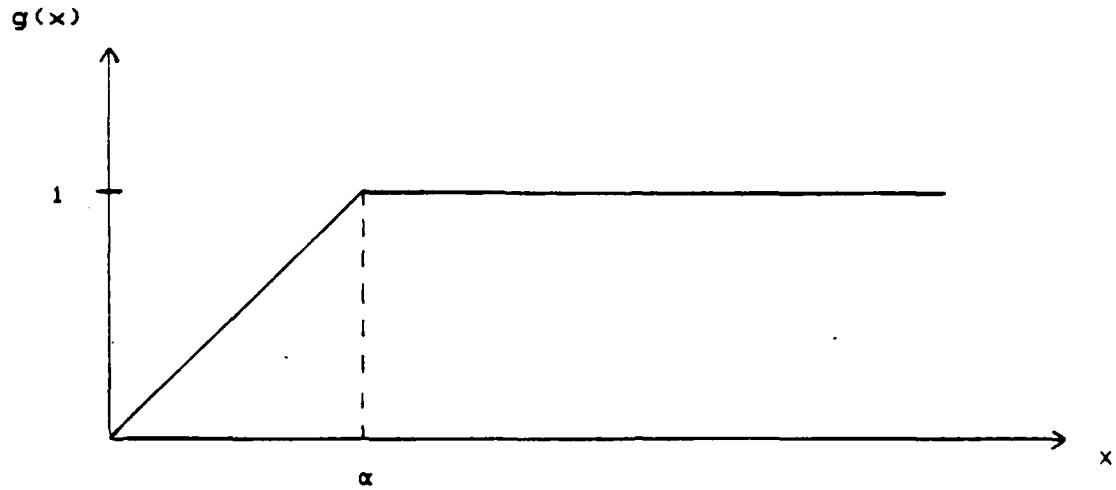

Figure 40. Linearized Modification to ZMNL

mean value of the assumed noise distribution.

A block diagram of the receiver is shown in Fig. 41.

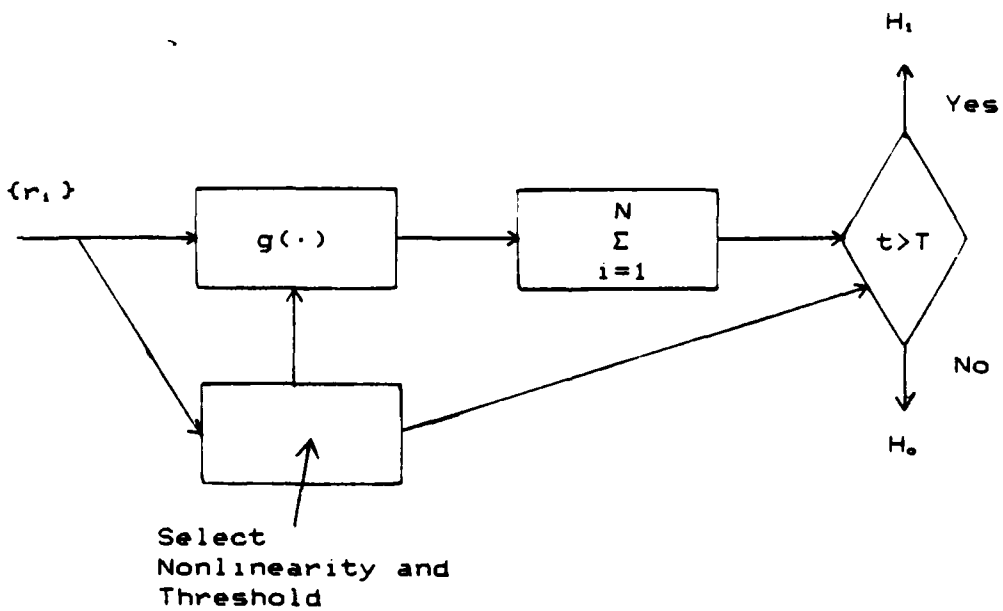

Figure 41. Receiver Structure for Adaptive Limiter

Note that the ZMNL must be adjusted. This information could be known a priori or, as symbolically shown in Fig. 41, determined from the statistics of the noise. Both cases will be examined below.

The false alarm rate performance of this modified receiver in Hall and Gaussian noise, where the statistics are known a priori, is shown in Fig. 42 for N equal to 10. The value for α was determined from the noise mean. At a P_{FA} equal to 1×10^{-2}, the P_D curves of this receiver are shown in Fig. 43. The threshold was determined from Fig. 42. The Gaussian noise performance of this receiver is poorer than that of the square and sum receiver but only by a few percent. However, there is a dramatic improvement in the P_D for the impulsive noise cases. It is interesting to note that for the same noise power, a well designed nonlinear receiver provides better detection performance in impulsive noise than the optimum receiver for Gaussian noise [Ref. 49].

By plotting the empirically determined threshold from Fig. 42 versus the mean of the noise distribution it is seen that the relationship is almost linear. This is shown in Fig. 44 for two false alarm rates. Using this relationship the ZMNL and threshold can be adaptively modified to provide nearly constant false alarm rate (CFAR) performance under varying noise conditions. This is a desirable characteristic for an energy detection receiver.

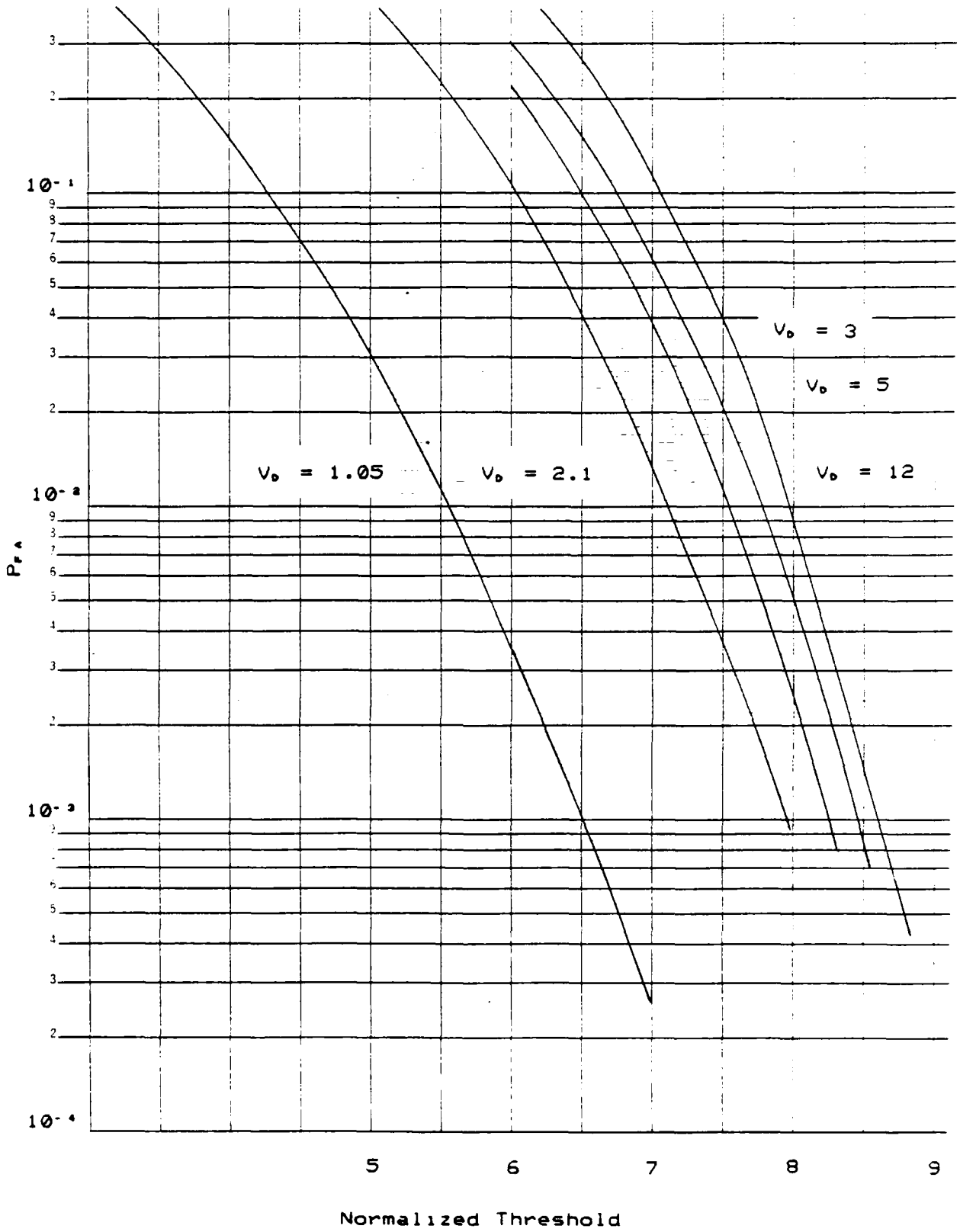

Figure 42. P_{FA} for Limiter Receiver in Gauss and Hall Noise

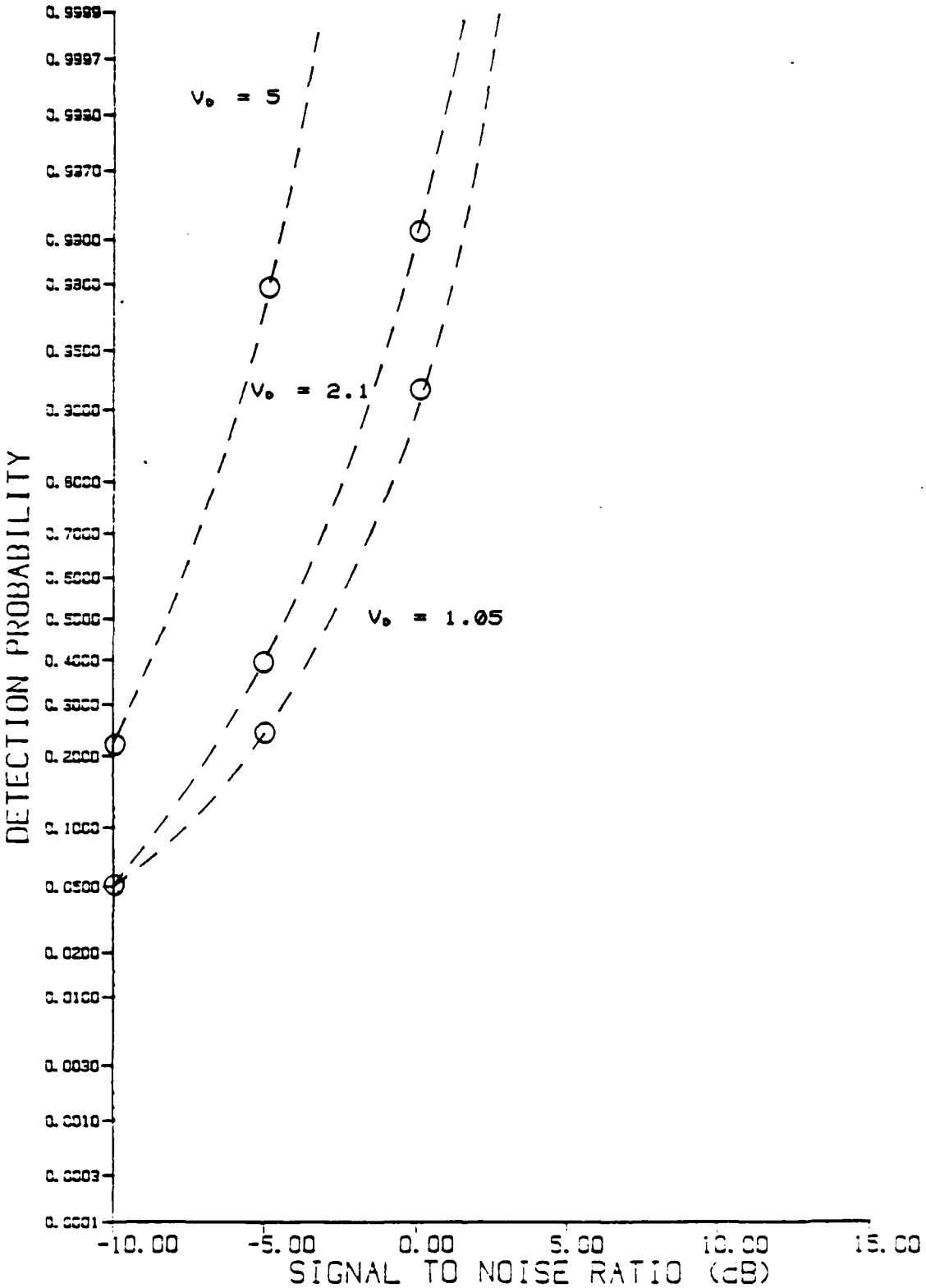

Figure 43. P_D for Limiter Receiver in Gauss and Hall Noise as Function of V_D for $P_{FA} = 1 \times 10^{-2}$

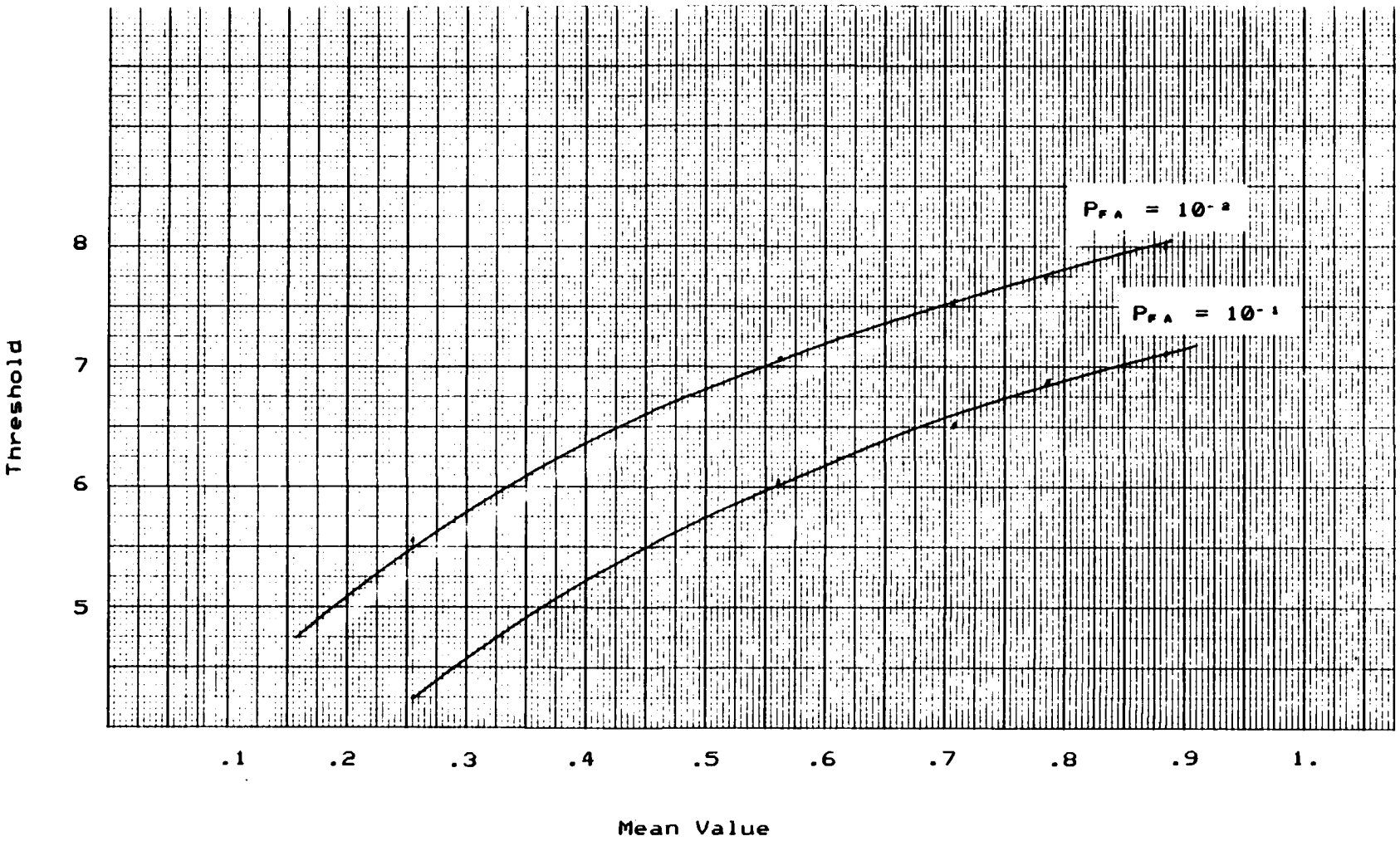

Figure 44. Threshold versus Mean Value of Hall Distributions for Limiter Receiver and $P_{FA} = 1 \times 10^{-1}$ and 1×10^{-2}

A final question to be resolved in implementing the receiver is the real time determination of an estimate of the mean and mean square values of the noise. One approach is to sample the noise in a signal free adjacent channel and another is to form the sample mean of the noise using past sample values with no signal present [Ref. 50]. We will implement the latter approach and test the adaptive receiver on actual signal and noise samples. In sequencing the samples two general approaches may be used. The samples may be processed in blocks with no overlap which is the case corresponding to the hypothesis tests discussed in this Chapter. The other option is sequentially processing each sample with rank two updates of the test statistic, the ZMNL and the threshold. In this case the hypothesis test formulation will provide a lower bound on P_b.

The sequential sampling approach was chosen and two runs of the adaptive receiver are shown in Figs. 45 and 46. The test statistic, shown by the dotted line, was formed from the 10 previous samples using the receiver structure in Fig. 41. The adaptive threshold, shown by the dashed line, was formed from the sample mean and mean square estimates of the previous 20 though 50 samples. The sample mean is shown by the heavy solid line and the individual envelope data points by the light solid line.

This receiver structure requires H_0 to be true at the start of the test and will detect the transition to H_1.

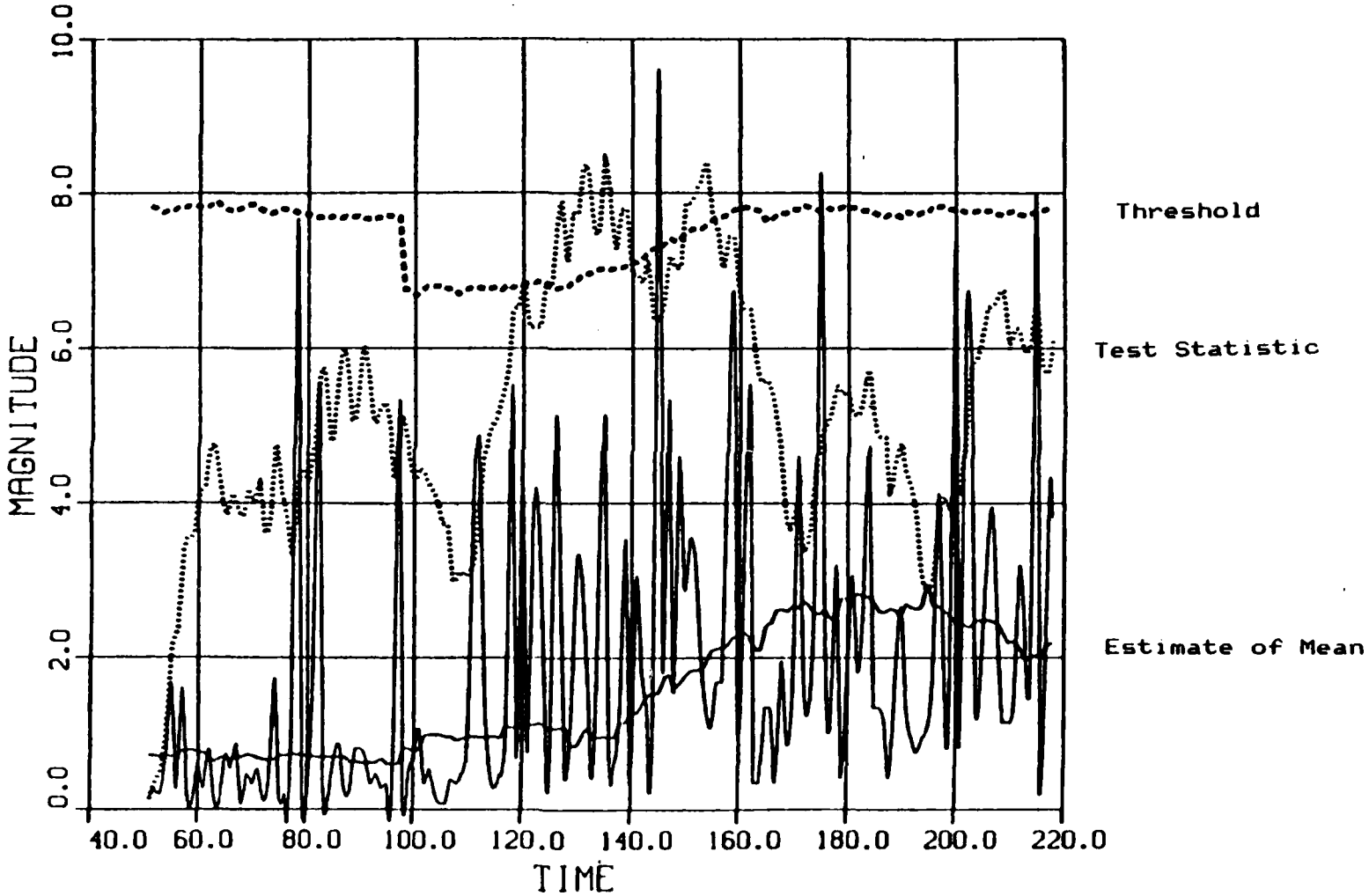

Figure 45. Adaptive Limiter Operation in Atmospheric Noise

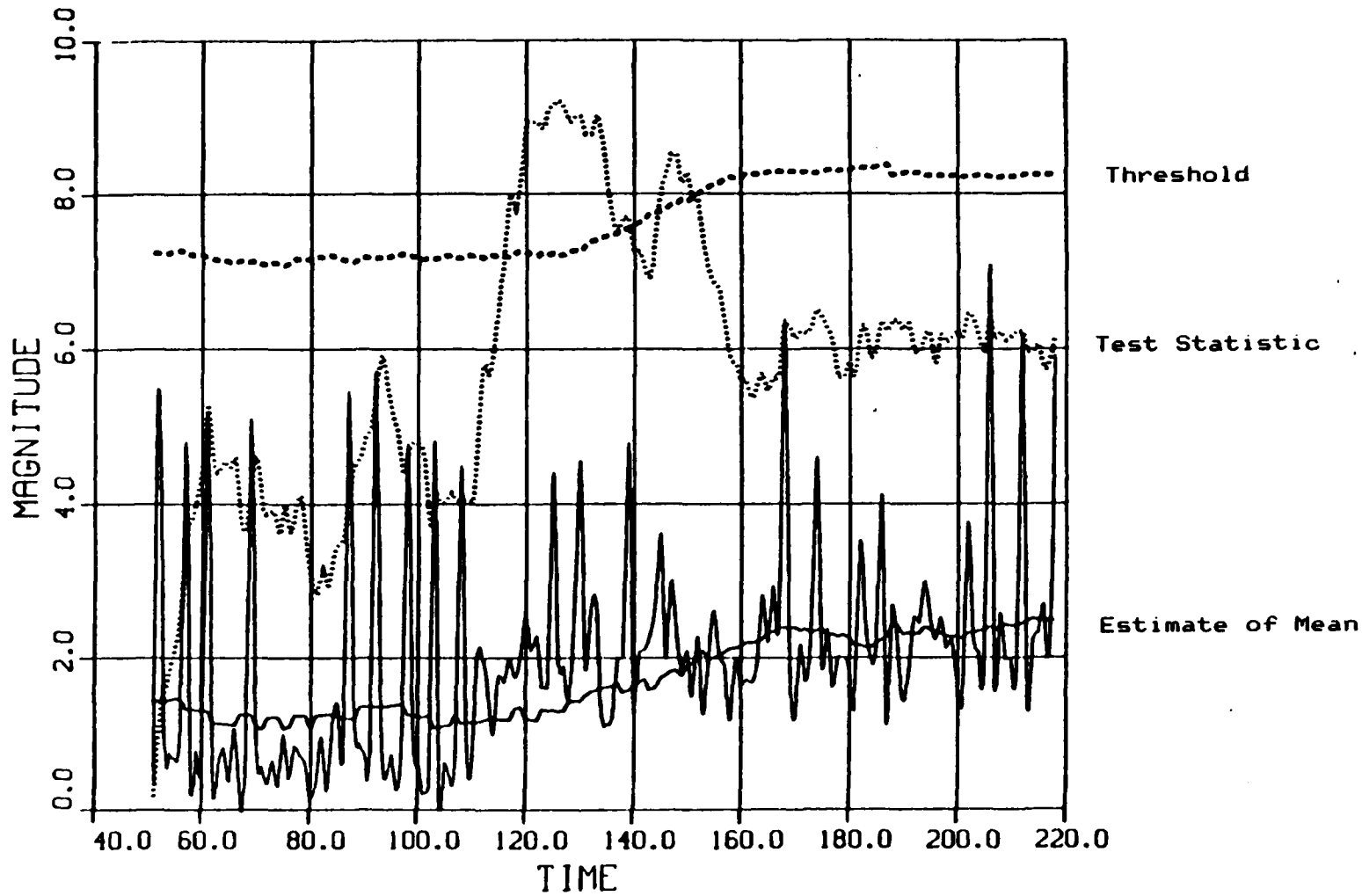

Figure 46. Adaptive Limiter Operation in Gap Noise

Since the adaptive threshold assumes noise only samples, it will be corrupted when signal plus noise samples are used to form it. This will occur 20 samples after H_1 becomes true.

This effect can be seen in Fig. 45 where an actual signal from one filter of a compressive receiver is plotted. The noise is highly impulsive and would be a very difficult detection environment for a receiver optimized for Gaussian noise. Samples 50 to 110 are noise only and samples 110 to 220 are signal plus noise. The test statistic exceeds the threshold at sample 125 and the receiver would declare H_1 true at this point. However, due to the fact that the test statistic and the threshold are both corrupted by the signal plus noise samples, the test statistic later drops below the new threshold.

In Fig. 46, the receiver performance in a simulated gap noise environment is analyzed. The signal commenced at sample 110 and the receiver declared the signal present at sample 117. Again the threshold is later corrupted and the test statistic drops below the threshold.

F. SUMMARY

This Chapter has presented a systematic development of the bandpass energy detection problem in impulsive noise. Starting with a Hall density function for the noise, the locally optimum receiver is derived. This receiver is modified to design a practical receiver with robust

performance in non-Gaussian noise. The design methodology clearly delineates the role of the test statistic, threshold and nonlinearity. This allows independent evaluation of each of these features. One aspect of energy detection receivers not considered is the role of data in filters adjacent to the filter being processed. In an impulsive noise environment, the noise statistics of adjacent filters will be correlated and their use may potentially offer a further performance gain.

VI. CONCLUSION

A. RESULTS

The dissertation has investigated the modeling of atmospheric and man-made radio noise and applied the results to the bandpass energy detection problem.

A generalized means of describing an impulsive noise process in terms of its complex envelope was derived. Previous models of atmospheric noise were surveyed and some extensions to the Hall model for atmospheric noise were developed.

Using the physical characteristics of gap noise, a nine parameter model was constructed that allows arbitrary sources of gap noise to be synthesized. The driving impulses for the gap noise were postulated to be points of a branching renewal process. The application of this type of probabilistic model to power line noise is unique. Additional results include a new proof of the power spectrum of an equilibrium renewal point process and a derivation of the power spectrum of a truncated branching renewal point process. The postulated model was shown to correctly predict all the significant features of the observed spectrum.

In a similar fashion, corona noise was postulated as a filtered impulse process with a periodically modulated rate function. This model was shown to correctly duplicate the

observed time domain behavior of corona noise. A method for estimating the parameters of the model was discussed and an actual example of corona noise simulated.

The energy detection problem was also considered and starting with an assumed density for impulsive noise, a design methodology for a parametric and robust receiver was developed. This receiver was then tested against actual and simulated data and shown to be superior to the Gaussian noise receiver when corrupted with impulsive atmospheric or power line noise.

It has been stated that in engineering design one seeks not so much to be optimum but to avoid crippling non-optimalities [Ref. 51]. It is hoped that this research will allow system designers to test their systems with simulated interference based on the models presented. The robustness of the system in an actual noise environment can then be evaluated, as was done in this research for the locally optimum energy detector. The noise models developed here should be particularly applicable to systems that operate from a fixed site within line of sight of power lines where the chance of having interference from gap or corona noise sources is significant.

B. FURTHER RESEARCH

At the conclusion of this dissertation several problems are worthy of further study. Research should be done to

define the range of values for the power line noise model parameters and to determine the effect of power line construction practices on the parameters. The susceptibility of various types of communication equipment to simulated gap and corona noise should also be examined. The corona noise model needs to be extended so that it can be specified and estimated using a bandpass vice lowpass filter impulse response. The work on energy detection suggests many opportunities for further research. The problem of estimating the unknown noise parameters for the adaptive updates and the inclusion of adjacent filter samples into an algorithm are prime examples.

APPENDIX A

INSTRUMENTATION

The instrumentation configuration employed to provide data on the detailed time- and frequency-domain properties of high frequency (HF) radio noise is shown in Fig. 47. The

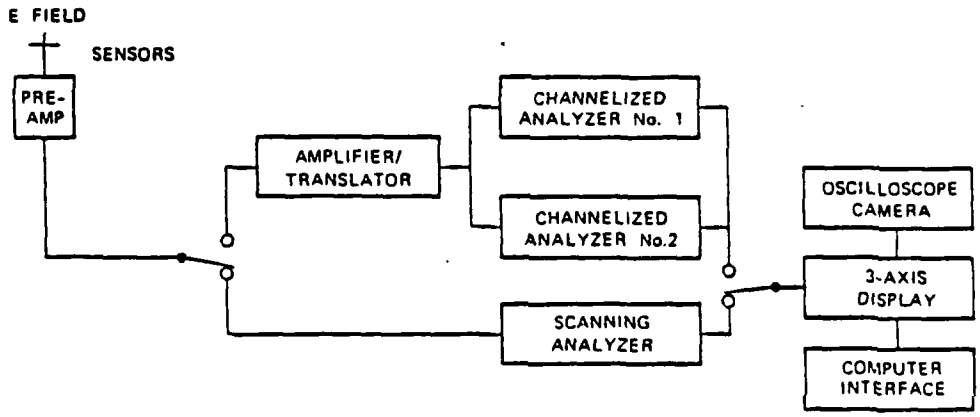

Figure 47. Simplified Block Diagram of Measurement System

radio frequency (RF) input to the instrumentation was either a fixed HF long wire antenna or a whip antenna mounted on a mobile van. One complete measurement system is transportable and may be moved from site to site. The other system is installed in a mobile van for noise measurements directly at the interference source [Ref. 53].

In the lower half of Fig. 47, a Hewlett-Packard 141T Spectrum Analyzer is used as a scanning receiver to drive a Develco 7200B 3- Axis Display. The spectrum analyzer can be

tuned to any desired frequency in the HF band. Its scan rate, scan width, intermediate frequency (IF) bandwidth, IF gain, RF attenuation, and other controls can be adjusted to best describe the noise under observation.

An alternate and complementary part of the system is used to examine the narrowband properties of HF noise and is depicted in the upper half of Fig. 47. An HF receiver is used as an amplifier/translator and tuned to a frequency where the noise is present. The demodulated audio output is then applied to a Wavetek (Nicolet) UA500A spectrum analyzer which subdivides the audio-output spectrum into about 500 frequency segments. When the full audio-output bandwidth of 5 kHz is examined, the UA500A provides a frequency resolution of 10 Hz per segment. The Wavetek analyzer can provide individual transforms or average a selected number of successive transforms. The transforms (either individual or averaged) are then presented on the 3-axis display or an oscilloscope.

The 3-axis display provides a continuous moving real-time visual representation of the analog output from the spectrum analyzers or narrowband receiver audio output. The receiver or analyzer output analog data are digitized in the display and stored in a semiconductor memory. The data in the memory are formatted and shown on a cathode ray tube (CRT) in a convenient frequency-amplitude-time (3-axis)

format. The 3-axis presentation can be frozen at any desired time and photographed with a standard oscilloscope camera.

Fig. 48 illustrates the procedure used to make the 3-axis presentation. The analog input is divided into 512

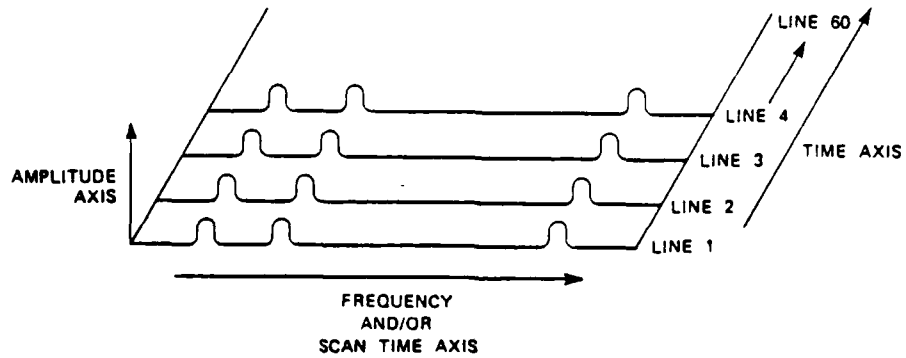

Figure 48. Diagram of Data Format

equally spaced data points (indicated by the horizontal dots of Fig. 48). The signal amplitude at each data point is represented by an 8-bit word. When a scan is completed, its data are also stored in memory. Line 1 in the view moves to line 2, and the new scan appears as line 1. Subsequent scans move earlier data, line by line, upwards along the time axis to create a rising raster type display. When the memory is full (64 scans), each new scan is entered into the bottom line, and the oldest data at the top line is discarded. The resulting animated view provides a visual picture of noise and signals within the block of frequencies if the spectrum analyzer output is being observed. If the

receiver audio output is being observed the display is a stacked series of consecutive time records.

The 3-axis display has a number of controls to aid the observer in analyzing the structure of data presented. Among these controls are: (1) elevation and azimuth geometry controls to vary the viewing aspect, (2) an amplitude compression control, (3) a threshold control to vary background levels, (4) time-axis expansion controls, and (5) a stop-action switch to freeze the data in memory for detailed observation, for observation from various aspects, or for photographing. These controls are used to optimize the presentation of desired signal detail.

Accurate frequency, time and amplitude calibrations are maintained so that the resulting 3-axis photos can be manually scaled for precise signal detail. The digitized data at the display input are available at a digital interface connector for external digital recording or processing. Received data can be processed by computer to obtain conventional noise statistics. This feature permits the comparison of selected 3-axis views of noise with standard statistical descriptors of noise.

APPENDIX B

FILTERED IMPULSE PROCESS

The complex envelope of a noise process can be described by the following equation

$$n(t) = g(t) + \sum_{i=1}^{N(t)} a_i e^{-j\theta_i} h(t-t_i) \qquad \text{(B-1)}$$

where $g(t)$ is a quadrature Gaussian process, $h(t)$ is a linear filter, a_i is an independent, identically distributed random amplitude and θ_i is a random phase uniformly distributed over 0 to 2π. The joint characteristic function of the inphase and quadrature components of the above process is

$$\phi(\omega_1, \omega_2) = E[e^{j(\omega_1 n_c(t) + \omega_2 n_s(t))}]. \qquad \text{(B-2)}$$

If the Gaussian noise is assumed independent of the impulsive noise the characteristic function of the Gaussian term alone can be written

$$\phi_g(\omega_1, \omega_2) = E[e^{j(\omega_1 g_c(t) + \omega_2 g_s(t))}]. \qquad \text{(B-3)}$$

The inphase and quadrature components of bandpass white Gaussian noise are independent so

$$\phi_g(\omega_1, \omega_2) = e^{-N_0 B(\omega_1^2 + \omega_2^2)/2}. \qquad \text{(B-4)}$$

The joint characteristic function of the ith pulse of the inphase and quadrature impulsive noise terms is

$$\phi_i(\omega_1,\omega_2) = E[e^{ja_i(\omega_1(h_c(t-t_i)\cos\theta_i - h_s(t-t_i)\sin\theta_i) + \omega_2(h_c(t-t_i)\sin\theta_i + h_s(t-t_i)\cos\theta_i))}]. \qquad \text{(B-5)}$$

Since the noise process is narrowband, its joint density function is circularly symmetric and the following transformation can be applied

$$\omega_r = (\omega_1^2 + \omega_2^2)^{1/2} \qquad \alpha = \tan^{-1}(\omega_1/\omega_2)$$

$$\omega_1 = \omega_r\cos\alpha \qquad \omega_2 = \omega_r\sin\alpha. \qquad \text{(B-6)}$$

This type of transformation of a 2-D Fourier transform to a one dimensional transform of the envelope is known as a Hankel Transform and the inversion formula is

$$p(r) = \int_0^\infty r\omega_r\phi(\omega_r)J_0(r\omega_r)d\omega_r \qquad \text{(B-7)}$$

where J_0 is the ordinary Bessel function of the first kind, order 0. To simplify the derivation it is assumed that $h_s(t)$ is zero (see comment before Eqn. 2-21). Now transforming Eqn. B-5 and taking the expected value of θ_i and a_i

$$\phi_i(\omega_r) = E[\int_0^\infty \int_0^{2\pi} p(\theta_i)p(a_i)e^{j\omega_r a_i h_c(t-t_i)\cos(\theta_i-\alpha)} d\theta_i da_i] \qquad \text{(B-8)}$$

Since θ_i is uniformly distributed over 0 to 2π,

$$\phi_i(\omega_r) = E\left[\int_0^\infty p(a_i) J_0(\omega_r a_i h_c(\tau)) da_i\right]. \tag{B-9}$$

If N(T) in Eqn. B-1 is a Poisson process with rate λ and observation interval T, the τ_i's are independent and uniform over (0, T) allowing the characteristic function of the impulsive term to be written as

$$\phi_I(\omega_r) = \sum_{k=0}^{\infty} \phi^k(\omega_r) \Pr[N = k]. \tag{B-10}$$

Now using the probability law for k events of a Poisson process

$$\phi_I(\omega_r) = \sum_{k=0}^{\infty} \phi^k(\omega_r) e^{-\lambda T} (\lambda T)^k / k! \tag{B-11}$$

which sums to

$$\phi_I(\omega_r) = e^{\lambda \int_0^\infty p(a) \int_0^T [J_0(\omega_r a h_c(\tau)) - 1] d\tau da} . \tag{B-12}$$

Using the convolution property of zero order Hankel transforms [Ref. 54] and Eqn. B-7 the density function of the envelope for Gaussian plus impulsive noise is

$$p(r) = \int_{-\infty}^{\infty} r\omega_r J_0(r\omega_r) \phi_g(\omega_r) \phi_I(\omega_r) d\omega_r . \tag{B-13}$$

APPENDIX C

SIGNAL PLUS NOISE DENSITY

For the truncated Hall model with $\theta = 3$, the joint density function of the in-phase and quadrature components is given by:

$$p(x,y) = \frac{D^2 2\gamma^2}{2\pi(D^2-1)(x^2+y^2+\gamma^2)^2} \qquad 0 < x^2 + y^2 < T_p^2$$

$$= 0 \qquad x^2 + y^2 > T_p^2 \qquad \text{(C-1)}$$

where

$$D = (1 + T_p^2/\gamma^2)^{1/2} .$$

The sum of a random phase sinusoidal signal of amplitude A and noise can be expressed in terms of its in-phase and quadrature components w and z where:

$$w = A\cos(\psi) + x$$

$$z = A\sin(\psi) + y. \qquad \text{(C-2)}$$

Eqn. C-2 is substituted into Eqn. C-1 and transformed to polar coordinates with

$$w = r\cos(\emptyset)$$

$$z = r\sin(\emptyset) \qquad \text{(C-3)}$$

where r represents the envelope and $\emptyset$ the phase of the signal plus noise. The joint probability density function $p(r,\emptyset)$ conditioned on ψ is

$$p(r,\emptyset|\psi) = \frac{D^2 \qquad r2\gamma^2}{2\pi(D^2-1)(r^2 - 2A\cos(\psi - \emptyset) + A^2 + \gamma^2)^2}$$

$$\emptyset < r^2 - 2A\cos(\psi - \emptyset) + A^2 < T_p^2$$

$$= \emptyset \qquad \text{elsewhere.} \tag{C-4}$$

This expression is valid for all values of r between $\emptyset$ and $T_p - A$. Since our principal interest is the small signal case, $A << T_p$, this will not affect subsequent analysis. By integrating Eqn. C-4 with respect to $\emptyset$, the conditional marginal density function of the envelope, $p(r|\psi)$, is obtained;

$$p(r|\psi) = 2\int_{\emptyset}^{\pi} p(r,\emptyset|\psi)\, d\emptyset. \tag{C-5}$$

The integral is a function only of $\cos(\psi - \emptyset)$, ψ appears nowhere else in the integral. Therefore by setting $\sigma = \psi - \emptyset$ and using Eqn. 2.554-3 in [Ref. 54] gives

$$p(r|\psi) = \frac{(r^2 + A^2 + \gamma^2)\, 2\gamma^2 rD^2}{(r^4 - 2A^2r^2 + 2A^2\gamma^2 + 2\gamma^2r^2 + A^4 + \gamma^4)(D^2 - 1)}. \tag{C-6}$$

Since ψ is assumed independent from sample to sample and uniformly distributed over 2π,

$$p(r) = \int_{\emptyset}^{2\pi} p(r|\psi)p(\psi)\, d\psi \tag{C-7}$$

and

$$p(r) = \frac{(r^2 + A^2 + \gamma^2)\, 2\gamma^2 r D^2}{(r^4 - 2A^2 r^2 + 2A^2\gamma^2 + 2\gamma^2 r^2 + A^4 + \gamma^4)(D^2 - 1)} . \tag{C-8}$$

By a similar argument, the density function for a random phase sinusoidal signal in narrowband noise with a Hall5 distribution is

$$p(r) = \frac{2\gamma^4 r(b^2 + 2a^2)}{(a^2 - b^2)^{5/2}} \tag{C-9}$$

where

$$a = r^2 + A^2 + \gamma^2$$

and

$$b = -2Ar.$$

APPENDIX D

SPECTRUM OF A RENEWAL PROCESS

The complex envelope representation of filtered impulse noise on a finite interval T is given by

$$n(t) = \sum_{i=1}^{N(T)} a_i e^{-j\theta_i} h(t-t_i) \; ; \qquad 0 < t < T. \tag{D-1}$$

N(T) is a random unit counting process denoting the number of impulses in the interval, the $\{t_i\}$ are the random arrival times and θ_i is uniformly distributed over 0 to 2π. The pulse amplitudes $\{a_i\}$ are identically distributed statistically independent random variables with second moment A_2 and fourth moment A_4. The filtering effect on the impulses are accounted for by the time invariant complex envelope impulse response h(t).

The envelope squared of n(t) is

$$E^2(t) = n(t)n^*(t) = \sum_{i=1}^{N(T)} a_i^2 \, h(t-t_i)h^*(t-t_i) \tag{D-2}$$

where we have assumed terms of the form $h(t-t_i)h^*(t-t_k)$ for different i and k are negligible. We estimate the power spectral density (PSD) of the envelope by averaging magnitude squared, length T, Fourier transforms of $E^2(t)$. The mean value of the estimate is

$$\bar{S}(\omega,T) = E[\mathcal{E}_2(\omega)\mathcal{E}_2^*(\omega)]/T \tag{D-3}$$

where

$$\mathcal{E}_s(\omega,T) = \int_0^T E^2(t)e^{-j\omega t}\,dt = \sum_{i=1}^{N(T)} a_i^2 e^{-j\omega t_i} H_s(\omega)$$

and

$$H_s(\omega) = \int_{\infty}^{-\infty} h(t)h^*(t)e^{-j\omega t}\,dt$$

is the Fourier transform of the magnitude squared impulse response. We have assumed the impulse response is much shorter than the observation interval T.

The mean of the estimate becomes

$$\bar{S}(\omega,T) = E[\sum_{k=1}^{N(T)} \sum_{i=1}^{N(T)} a_i^2 a_k^2 e^{-j\omega(t_i-t_k)}]|H_s(\omega)|^2/T. \tag{D-4}$$

This is a compact and general expression for the PSD of a truncated filtered point process. It is in terms of a summation of the characteristic functions of the interarrival time distributions between all combinations of pairs of points. (The term incorporating the frequency response of the filter will be set to one for the rest of the analysis.) Conditioning on N(T)

$$\bar{S}(\omega,T) = \sum_{l=2}^{\infty} E[\sum_{k=1}^{N} \sum_{i=1}^{N} a_i^2 a_k^2 e^{-j\omega(t_i-t_k)}]Pr[N = l]/T. \tag{D-5}$$

Plotting the difference k-j indicates a different summation over m and n shown below.

```
k     N                                          n N
      .                                          .
      .                                          .
-3 -2 -1  0                          -3 -2 -1 | 1  2  3
-2 -1  0  1                             -2 -1 | 1  2
-1  0  1  2 ... N                        -1 | 1
 0  1  2  3        j                                          m
```

Let $m = i - k$ and $n = i + k$ such that $t_m = t_i - t_k$ is the mth interarrival time. Then Eqn. D-5 can be written as

$$\bar{S}(\omega,T) = \sum_{l=2}^{\infty} E\{ \sum_{n=1}^{N-1} \sum_{m=1}^{-n} A_2^2 e^{-j\omega t_m} + NA_4 + \sum_{n=1}^{N-1} \sum_{m=1}^{n} A_2^2 e^{-j\omega t_m} \} Pr[N = l]/T. \tag{D-6}$$

On further rearrangement

$$\bar{S}(\omega,T) = \bar{N}A_4/T + \sum_{l=2}^{\infty} A_2^2 E\{ \sum_{n=1}^{N-1} \sum_{m=1}^{n} e^{j\omega t_m} + e^{-j\omega t_m} \} Pr[N = l]/T \tag{D-7}$$

and conditioning the interarrival time distribution over the number of pulses N in the interval T

$$\bar{S}(\omega,T) = \bar{N}A_4/T + A_2^2 \sum_{l=2}^{\infty} \sum_{n=1}^{l-1} \sum_{m=1}^{n} [\phi_m(j\omega|N=l) + \phi_m^*(j\omega|N=l)] Pr[N = l]/T \tag{D-8}$$

where

$$\phi_m(j\omega|N=l) = E[e^{j\omega t_m}]$$

is the characteristic function of the mth interpulse spacing given exactly l pulses in the interval. The following assumption is now made; that the mth interpulse spacing is

the sum of m statistically independent interpulse separations, and is independent of l, the number of pulses in the interval. This assumption will give an asymptotically correct result for the PSD as the observation interval T, becomes much greater than μ, the mean value of the interarrival times.

With the above assumption

$$\emptyset_{*}(j\omega|N=l) = \emptyset^{m}(j\omega) \tag{D-9}$$

where $\emptyset(j\omega)$ is the characteristic function of the interpulse separations. Eqn. D-8 then sums to

$$\bar{S}(\omega,T) = \bar{N}A_4/T + A_2^2 \sum_{l=2}^{\infty} \sum_{n=1}^{l-1} \left[\frac{\emptyset(j\omega)-\emptyset(j\omega)^{n+1}}{1-\emptyset(j\omega)} + \frac{\emptyset^{*}(j\omega)-\emptyset^{*}(j\omega)^{n+1}}{1-\emptyset^{*}(j\omega)} \right] Pr[N = l]/T \tag{D-10}$$

and summing again

$$\bar{S}(\omega,T) = \bar{N}A_4/T + A_2^2 \sum_{l=2}^{\infty} \left\{ \frac{l\emptyset(j\omega)}{(1-\emptyset(j\omega))} - \frac{\emptyset(j\omega)}{(1-\emptyset(j\omega))^2} + \frac{\emptyset(j\omega)^{l+1}}{(1-\emptyset(j\omega))^2} + \frac{l\emptyset^{*}(j\omega)}{(1-\emptyset^{*}(j\omega))} - \frac{\emptyset^{*}(j\omega)}{(1-\emptyset^{*}(j\omega))^2} + \frac{\emptyset^{*}(j\omega)^{l+1}}{(1-\emptyset^{*}(j\omega))^2} \right\} Pr[N = l]/T. \tag{D-11}$$

Rearranging

$$\bar{S}(\omega,T) = \bar{N}A_4/T + A_2^2/T\{\bar{N} - Pr[N=1]\} \sum_{l=2}^{\infty} \left\{ \frac{\emptyset(j\omega)}{(1-\emptyset(j\omega))} + \frac{\emptyset^{*}(j\omega)}{(1-\emptyset(j\omega))} \right\}$$

$$- A_2^2/T \{1 - Pr[N=0]-Pr[N=1]\} \left\{ \frac{\phi(j\omega)}{(1-\phi(j\omega))^2} + \frac{\phi^*(j\omega)}{(1-\phi^*(j\omega))^2} \right\}$$

$$+ A_2^2/T \sum_{l=2}^{\infty} Pr[N = l] \left\{ \frac{\phi(j\omega)^{l+1}}{(1-\phi(j\omega))^2} + \frac{\phi^*(j\omega)^{l+1}}{(1-\phi^*(j\omega))^2} \right\}. \qquad \text{(D-12)}$$

Since $Pr[N = l]$ is less than 1 and $|\phi(\omega)| < 1$ [Ref. 41:p. 115] for any distribution, then the absolute convergence of the third term is guaranteed. For an equilibrium renewal process

$$\bar{N} = E[N(t)] = T/\mu \qquad \text{(D-12)}$$

where μ is the mean time between renewals [Ref. 32:p. 46]. Now letting T, the observation interval, go to infinity the asymptotic PSD is

$$\bar{S}(\omega) = \lim_{T=>\infty} \bar{S}(\omega,T) = \frac{A_2}{\mu} \left\{ \frac{A_4}{A_2^2} + 2\, Re\left[\frac{\phi(j\omega)}{1-\phi(j\omega)} \right] \right\}. \qquad \text{(D-13)}$$

This is the expression for the PSD of an independent increment point process in terms of the characteristic function of the interarrival distribution. A similar result result was developed by Cox and Miller by considering the renewal intensity function [Ref. 55].

APPENDIX E

SPECTRUM OF A BRANCHING RENEWAL POINT PROCESS

The complex envelope representation of filtered impulse noise arising from a branching renewal process on a finite interval T is given by

$$n(t) = \sum_{m=1}^{M(T)} \sum_{n=1}^{N_m} a_{mn} e^{-j\theta_{mn}} h(t-t_{mn}-T_m) \qquad \text{(E-1)}$$

where T_m is the beginning of the mth main interval, N_m is the number of impulses in the mth interval, arriving at times $\{t_{mn}\}$ after its onset and M(T) is the unit counting process defining the number of main events in the observation interval T. The pulse amplitudes $\{a_{mn}\}$ and phases $\{\theta_{mn}\}$ are statistically independent random variables and the $\{\theta_{mn}\}$ are taken to be uniform on $\{0,2\pi\}$. The net filtering effects on the impulses are accounted for by the time invariant complex envelope impulse response, h(t).

The envelope squared of the process is

$$E^2(t) = n(t)n^*(t) = \sum_{m=1}^{M(T)} \sum_{n=1}^{N_m} a^2_{mn} |h(t-t_{mn}+T_m)|^2 \qquad \text{(E-2)}$$

and using the same assumptions as Appendix D the mean value of the Bartlett estimate of the PSD is

$$\bar{S}(\omega,T) = E[|E_2(\omega,T)|^2]/T \qquad \text{(E-3)}$$

where $E_2(\omega,T)$ is the length T Fourier Transform of $E^2(t)$. Specifically,

$$E_s(\omega,T) = \sum_{m=1}^{M(T)} \sum_{n=1}^{N_m} a_{mn}^2 \, e^{-j\omega t_{mn}} \, e^{-j\omega T_m} H_s(\omega) \qquad \text{(E-4)}$$

with $H_s(\omega) = \int_0^T |h(t)|^2 e^{-j\omega t} dt$, the Fourier transform of the magnitude squared impulse response. To find the mean of the estimate we must evaluate

$$\bar{S}(\omega,T) = E\Big[|H_s(\omega)|^2 \sum_{m=1}^{M(T)} \sum_{n=1}^{N_m} \sum_{l=1}^{M(T)} \sum_{k=1}^{N_l} a_{mn}^2 \, a_{lk}^2 \, e^{-j\omega(t_{mn}-t_{lk})} \, e^{-j\omega(T_m-T_l)} \Big]/T \qquad \text{(E-5)}$$

In order to simplify this expression, we make use of assumptions 1, 2 and 4 from section 3D; (1) $E[a^2_{mn} a^2_{lk}] = a^4$, which will be normalized to one for simplicity, (2) N_m and N_l equal either N1 or N2 alternating between the two values and (3) $f(t_{mn})$ and $f(t_{ln})$, the interarrival time distributions, alternate between the negative and positive phase distribution parameters. Furthermore, let M be an even number of main process points occurring at intervals, $T_o/2$, of a fundamental frequency (in our case $f_o = \omega_o/2\pi = 1/T_o = 60$ Hz, the power-line frequency) and let M2 = M/2. This assumption will greatly simplify the calculations and for M greater than 10, not significantly reduce the accuracy of the result.

Now looking only at the factors involved in the summation in Eqn. E-5, six separate terms can be identified:

Term 1 - The inter-pulse group summations between pulses in pulse groups with N1 pulses

$$= M2 \sum_{n=1}^{N1} \sum_{k=1}^{N1} E[e^{j\omega(t_n - t_k)}] \tag{E-6a}$$

Term 2 - The inter-pulse group summations between pulses in pulse groups with N2 pulses

$$= M2 \sum_{n=1}^{N2} \sum_{k=1}^{N2} E[e^{j\omega(t_n - t_k)}] \tag{E-6b}$$

Term 3 - The intra-pulse group summations between pulses in groups with N1 pulses

$$= \sum_{\substack{m=1 \\ m<>l}}^{M2} \sum_{l=1}^{M2} e^{-j\omega(m-l)T_o} \sum_{n=1}^{N1} \sum_{k=1}^{N1} E[e^{j\omega t_n}]E[e^{-j\omega t_k}] \tag{E-6c}$$

Term 4 - The intra-pulse group summations between pulses in groups with N2 pulses

$$= \sum_{\substack{m=1 \\ m<>l}}^{M2} \sum_{l=1}^{M2} e^{-j\omega(m-l)T_o} \sum_{n=1}^{N2} \sum_{k=1}^{N2} E[e^{j\omega t_n}]E[e^{-j\omega t_k}] \tag{E-6d}$$

Term 5 - The intra-pulse group summations between pulses in groups with N1 pulses per group to pulses in groups with N2 pulses

$$= e^{j\omega(T_o/2-T_b)} \sum_{m=1}^{M2} \sum_{l=1}^{M2} e^{-j\omega(m-l)T_o} \sum_{n=1}^{N1} \sum_{k=1}^{N2} E[e^{j\omega t_n}]E[e^{-j\omega t_k}] \tag{E-6e}$$

Term 6 - The intra-pulse group summations between pulses in groups with N2 pulses per group to pulses in groups with N1 pulses

$$= e^{-j\omega(T_o/2-T_b)} \sum_{m=1}^{M2} \sum_{l=1}^{M2} e^{-j\omega(m-l)T_o} \sum_{n=1}^{N2} \sum_{k=1}^{N1} E[e^{j\omega t_n}]E[e^{-j\omega t_k}] \tag{E-6f}$$

It is important to note the expression for the characteristic function of the interarrival times differs between the inter-pulse and intra-pulse cases. In the inter-pulse case, discussed in Appendix D, the summation is only over a function of the difference in the pulse positions where in the intra-pulse case the summation is over the absolute position of each pulse in its group.

Terms 1 and 2 can be evaluated using the results from Appendix D and assumption 3 from section 3D:

$$\text{Term 1} = M2\ \Xi(\omega,N1) \tag{E-7a}$$

$$\text{Term 2} = M2\ \Xi(\omega,N2) \tag{E-7b}$$

and the remaining terms can be determined by straightforward evaluation of the finite sums

$$\text{Term 3} = \left\{ \frac{\cos(M2\ 2\pi\omega/\omega_o) - 1}{\cos(2\pi\omega/\omega_o) - 1} - M2 \right\} \Omega(\omega,N1) \tag{E-7c}$$

$$\text{Term 4} = \left\{ \frac{\cos(M2\ 2\pi\omega/\omega_o) - 1}{\cos(2\pi\omega/\omega_o) - 1} - M2 \right\} \Omega(\omega,N2) \tag{E-7d}$$

Terms 5 and 6 are complex conjugates and can be combined to form one term

$$\text{Term 5a} = 2\cos(\omega(T_o/2-T_o))\left\{\frac{\cos(M2\ 2\pi\omega/\omega_o) - 1}{\cos(2\pi\omega/\omega_o) - 1}\right\}\psi(\emptyset_1, N1, \emptyset_2, N2) \tag{E-7e}$$

where $\emptyset_1$ and $\emptyset_2$ are the characteristic functions associated with the interarrival times for each phase and N1 and N2 are the number of renewals associated with each phase. The functions Ξ, Ω, and ψ are defined below;

$$\Xi(\emptyset,N) = \frac{N - N|\emptyset(j\omega)|^2}{|1 - \emptyset(j\omega)|^2} - 2\,\mathrm{Re}\left\{\frac{\emptyset(j\omega)\ (1 - \emptyset(j\omega)^N)}{(1 - \emptyset(j\omega))^2}\right\}, \tag{E-8}$$

$$\Omega(\emptyset,N) = \frac{|\emptyset(j\omega) - \emptyset(j\omega)^{N+1}|^2}{|1 - \emptyset(j\omega)|^2} \tag{E-9}$$

and

$$\psi(\emptyset_1, N1, \emptyset_2, N2) = \frac{(\emptyset_1(j\omega) - \emptyset_1(j\omega)^{N1+1})\ (\emptyset_2(-j\omega) - \emptyset_2(-j\omega)^{N2+1})}{(1 - \emptyset_1(j\omega))\ (1 - \emptyset_2(-j\omega))}. \tag{E-10}$$

Thus

$$\bar{S}(\omega,T) = \{E[H_2(\omega)]/T\} \sum_{n=1}^{5} \text{Term}(n). \tag{E-11}$$

APPENDIX F

NON-HOMOGENEOUS POISSON PROCESS

The following derivation is for the mean and variance of a compound periodic non-homogeneous filtered Poisson point process. This proof is a generalization of a proof presented in Papoulis [Ref. 41:pp. 382-383]. The expression for such a process on an interval 0 to T is given by

$$n(t) = \sum_{i=1}^{N(T)} a_i h(t-t_i), \qquad \text{(F-1)}$$

where N(T) is a unit counting process with periodic rate parameter $\lambda(t)$, a_i is the weighting of the ith point and is independent and identically distributed (IID) from point to point and h(t) is the time invariant impulse response of the filter.

The time axis is divided into consecutive intervals I_j of length $\Delta\alpha$ where $\Delta\alpha = \alpha_j - \alpha_{j-1}$. The number of jumps in the counting process in the jth interval I_j is given by Δm_j. If $\Delta\alpha$ is sufficiently small, then the contribution to the total noise process from the jth interval is

$$\Delta n_j = \sum_{i=1}^{\Delta m_j} a_i h(t-\alpha_j), \qquad \text{(F-2)}$$

where Δm_j is a Poisson random variable with its rate parameter approximately equal to

$$\lambda(\alpha_j)\Delta\alpha. \qquad \text{(F-3)}$$

The moment function of the jth interval is then

$$\Delta\phi_j(s) \approx E[e^{s\sum_{i=1}^{\Delta m_j} a_i h(t-\alpha_j)}]. \qquad \text{(F-4)}$$

Conditioning on Δm_j,

$$\Delta\phi_j(s) \approx E[e^{s\sum_{i=1}^{\Delta m_j} a_i h(t-\alpha_j)} \mid \Delta m_j = k]\, Pr[\Delta m_j = k] \qquad \text{(F-5)}$$

and

$$\Delta\phi_j(s) \approx E[\prod_{i=1}^{k} e^{sa_i h(t-\alpha_j)}]\, Pr[\Delta m_j = k]. \qquad \text{(F-6)}$$

Since the a_i's are independent from pulse to pulse

$$\Delta s_j(s) \approx \prod_{i=1}^{k} E[e^{sah(t-\alpha_j)}]\, Pr[\Delta m_j = k], \qquad \text{(F-7)}$$

where the expectation is with respect to the random amplitude a. Using the Poisson probability law and recognizing the series expansion for the exponential gives

$$\Delta\phi_j(s) \approx e^{\lambda(\alpha_j)\Delta\alpha\{E[e^{sah(t-\alpha_j)}] - 1\}}. \qquad \text{(F-8)}$$

Since

$$n(t) = \sum_{i=-\infty}^{\infty} \Delta n_i(t), \qquad \text{(F-9)}$$

a sum of independent random variables, then

$$\phi_n(s) = \prod_{i=-\infty}^{\infty} \Delta\phi_i(s) \qquad \text{(F-10)}$$

using the convolution property of the moment generating function. The cumulant generating function is defined as

$$\psi_n(s) = \ln[\emptyset_n(s)], \tag{F-11}$$

where ln is the natural logarithm and

$$\psi_n(s) = \sum_{i=-\infty}^{\infty} \ln[\Delta\emptyset_i(s)]. \tag{F-12}$$

As $\Delta\alpha \Rightarrow 0$, then

$$\psi_n(s) = \int_{-\infty}^{\infty} p(a) \int_{-\infty}^{\infty} \lambda(\alpha) \left[e^{sah(t-\alpha)} - 1 \right] d\alpha da. \tag{F-13}$$

Using a similar argument the joint cumulant generating function for two random variables, $n(t_1)$ and $n(t_2)$ is

$$\psi_n(s_1, s_2) = \int_{-\infty}^{\infty} p(a) \int_{-\infty}^{\infty} \lambda(\alpha) \left[e^{s_1 ah(t_1-\alpha) + s_2 ah(t_2-\alpha)} - 1 \right] d\alpha da. \tag{F-14}$$

APPENDIX G

AUTOCORRELATION OF CORONA NOISE

The mean value of the cyclostationary process defined by assumptions 1 and 2 in section 4D is given by Eqn. 4-12. Substituting Eqn. 4-20 gives

$$E[e(t)] = E[a] \int_0^{\infty} \sum_{n=0}^{N_T} a_n \cos(\omega_0 n(t-s))(\alpha/\pi)^{1/2} e^{-\alpha s^2} ds. \quad \text{(G-1)}$$

Expanding the cosine and integrating

$$E[e(t)] = (\beta\pi/4)^{1/2} \sum_{n=0}^{N_T} \left[e^{\frac{-\omega_0^2 n^2}{4\alpha}} a_n \cos(\omega_0 nt) + \right.$$

$$\left. + \frac{\omega_0 n}{2(\alpha\pi)^{1/2}} \sum_{k=1}^{\infty} \frac{1}{(2k-1)!!} \left(\frac{-\omega_0^2 n^2}{2\alpha} \right)^{k-1} a_n \sin(\omega_0 nt) \right] \quad \text{(G-2)}$$

where $(\beta\pi/2)^{1/2} = E[a]$ and $(2k-1)!! = 1\ 3\ 5 \ldots 2k-1$ [Ref. 54: Eqn. 3.897]. The sine term is in quadrature with the dominant cosine term of Eqn. G-2 and represents a phase shift in the mean of the process relative to the rate function. This is due to the filtering effect where the impulse response of the filter persists, thus causing a lag in the mean value of the process. For the values of α and ω_0 considered in this work, the sine term in Eqn. G-2 will

be negligible relative to the cosine term. Physically, this means that for filter bandwidths much greater than the fundamental frequency of the corona noise, the phase shift will be insignificant.

Similarly the variance of the envelope when considered as a cyclostationary process is

$$\mathrm{Var}[e(t)] \approx 2B \sum_{n=0}^{N_T} \left[\frac{1}{2} (\alpha/2\pi)^{1/2} e^{\frac{-\omega_0^2 n^2}{8\alpha}} a_n \cos(\omega_0 nt) \right]. \tag{G-3}$$

Using Eqn. 4-14 the covariance of the assumed process is

$$\mathrm{Cov}(t_1, t_2) = 2B \int_{\max(t_1, t_2)}^{\infty} \sum_{n=0}^{N_T} a_n \cos(\omega_0 ns)(\alpha/\pi) e^{-\alpha(t_1 - s)^2} e^{-\alpha(t_2 - s)^2} ds \tag{G-4}$$

where after rearranging and completing the square

$$\mathrm{Cov}(t_1, t_2) = \left(2B(\alpha/\pi) e^{-\alpha(t_1 - t_2)^2/2}\right) \times$$

$$\int_{\max(t_1, t_2)}^{\infty} \sum_{n=0}^{N_T} a_n \cos(\omega_0 ns) e^{-2\alpha(s - (t_1 + t_2)/2)^2} ds. \tag{G-5}$$

Letting

$$u = (s - (t_1 + t_2)/2), \tag{G-6}$$

the covariance is

$$\mathrm{Cov}(t_1, t_2) = \left((\alpha/\pi)2\beta e^{-\alpha(t_1-t_2)^2/2}\right) \times$$

$$\int_{|t_1-t_2|}^{\infty} \sum_{n=0}^{N_T} a_n \cos(\omega_0 n(u+(t_1+t_2)/2)) e^{-2\alpha u^2} du \tag{G-7}$$

which cannot be evaluated in closed form.

The stationary autocorrelation function is found by using Eqns. G-2 and G-7 and the definitions given by Eqns. 4-15 and 4-19. The term due to the covariance in the autocorrelation function is

$$2\beta(\alpha/\pi)e^{-\alpha\tau^2/2}/T_0 \int_0^{T_0} \sum_{n=0}^{N_T} [a_n \cos(\omega_0 n(2t+\tau)) \int_{|\tau|}^{\infty} \cos(\omega_0 nu) e^{-2\alpha u^2} du$$

$$+ a_n \sin(\omega_0 n(t+\tau/2)) \int_{|\tau|}^{\infty} \sin(\omega_0 nu) e^{-2\alpha u^2} du]dt. \tag{G-8}$$

The sinusoidal terms will integrate to zero with the exception of the a_0 cosine term and the expression simplifies to

$$2\beta(\alpha/\pi)e^{-\alpha\tau^2/2} a_0 \int_{|\tau|}^{\infty} e^{-2\alpha u^2} du. \tag{G-9}$$

This term will be dominated by the first exponential and is approximated by

$$2\beta e^{-\alpha\tau^2/2} a_0 \, (\alpha/8\pi)^{1/2} \, . \qquad \text{(G-10)}$$

The stationary autocorrelation function term due to cyclostationary mean value function is

$$\frac{1}{T_0} \int_0^{T_0} E[e(t)]E[e(t+\tau)] \, dt, \qquad \text{(G-11)}$$

which using Eqn. G-2 is equal to

$$2\beta \, (1/8) \sum_{n=1}^{N_T} e^{\frac{-\omega_0^2 n^2}{4\alpha}} a_n^2 \cos\omega_0 n\tau + 2\beta(1/4)a_0^2 \, . \qquad \text{(G-12)}$$

An approximate expression for the stationary autocorrelation function is

$$\bar{R}(\tau) \approx 2\beta[e^{-\alpha\tau^2/2} a_0 (\alpha/8\pi)^{1/2} + (1/4)a_0^2 + (1/8) \sum_{n=1}^{N_T} e^{\frac{-\omega_0^2 n^2}{4\alpha}} a_n^2 \cos(\omega_0 n\tau)] . \qquad \text{(G-13)}$$

APPENDIX H

LOCALLY OPTIMUM ENERGY RECEIVER

The observations consist of a sequence of N complex samples. The hypotheses are:

$$H_0 : x_i = n_i$$

versus

$$H_1 : x_i = n_i + A^{1/2} s_i \qquad i = 1,\ldots,N \qquad \text{(H-1)}$$

where n_i are an independent, identically distributed (IID) complex noise samples with a joint inphase and quadrature density $p(n_c, n_s)$. The sequence s_i is a complex, zero mean signal sequence with a known variance, σ_i, and A is a real, positive number. The 1/2 power of A is chosen to facilitate the derivation.

The generalized likelihood ratio [Ref. 6:p. 585,21] to test the hypotheses described by Eqn. H-1 is

$$\Lambda(\underline{x},A) = \prod_{i=1}^{N} \int_{-\infty}^{\infty} \int_{-\infty}^{\infty} \frac{p(x_{c_i} - A^{1/2} s_{c_i}, x_{s_i} - A^{1/2} s_{s_i})}{p(x_{c_i}, x_{s_i})} p(s_{c_i}, s_{s_i}) ds_{c_i} ds_{s_i} . \qquad \text{(H-2)}$$

Applying Eqn. 5-8, and differentiating with respect to A,

$$t_{LO}(\underline{x},A) = \sum_{i=1}^{N} \int_{-\infty}^{\infty} \int_{-\infty}^{\infty} [\frac{-s_{c_i} \partial p(x_{c_i} - A^{1/2} s_{c_i}, x_{s_i} - A^{1/2} s_{s_i})/2}{\partial x_{c_i} p(x_{c_i}, x_{s_i}) A^{1/2}} +$$

$$\left. \frac{-s_{si}\partial p(x_{ci}-A^{1/2}s_{ci},x_{si}-A^{1/2}s_{si})/2}{\partial x_{si}\,p(x_{ci},x_{si})A^{1/2}} \right] p(s_{ci},s_{si})ds_{ci}ds_{si}\Bigg|_{A=>0}. \tag{H-3}$$

Letting A go to 0 and simultaneously taking the expectation of s_{ci} and s_{si} requires L'hospital's rule to evaluate the expression [Ref. 56]. After taking derivatives the test statistic is

$$t_{Lo}(\underline{x}) = \sum_{i=1}^{N}\int_{-\infty}^{\infty}\int_{-\infty}^{\infty}\Bigg[\frac{s_{ci}^2\,\partial^2 p(x_{ci}-A^{1/2}s_{ci},x_{si}-A^{1/2}s_{si})/2}{\partial x_{ci}^2\,p(x_{ci},x_{si})} +$$

$$\frac{s_{ci}s_{si}\,\partial^2 p(x_{ci}-A^{1/2}s_{ci},x_{si}-A^{1/2}s_{si})}{\partial x_{ci}\partial x_{si}\,p(x_{ci},x_{si})} +$$

$$\left. \frac{s_{si}^2\,\partial^2 p(x_{ci}-A^{1/2}s_{ci},x_{si}-A^{1/2}s_{si})/2}{\partial x_{si}^2\,p(x_{ci},x_{si})} \right] p(s_{ci},s_{si})ds_{ci}ds_{si}\Bigg|_{A=>0}. \tag{H-4}$$

In general, the inphase and quadrature noise components will be circularly symmetric even though not necessarily statistically independent [Ref. 41:p. 133] such that

$$f(r) = p((x_c^2 + x_s^2)^{1/2}) \tag{H-5}$$

with

$$r = (x_c^2 + x_s^2)^{1/2} . \tag{H-6}$$

Now A may be set to 0 and

$$t_{Lo}(\underline{r}) = \sum_{i=1}^{N} \int_{-\infty}^{\infty} \int_{-\infty}^{\infty} \Bigg[\frac{s_{ci}^2 [r_i f''(r_i) x_{ci}^2 - r_i f'(r_i) x_{ci}^2 + r_i^2]/2}{r_i^3 f(r_i)} +$$

$$\frac{s_{ci} s_{si} [r_i f''(r_i) x_{ci} x_{si} - f'(r_i) x_{ci} x_{si}]}{r_i^3 f(r_i)} +$$

$$\frac{s_{si}^2 [r_i f''(r_i) x_{si}^2 - r_i f'(r_i) x_{si}^2 + r_i^2]/2}{r_i^3 f(r_i)} \Bigg] p(s_{ci}, s_{si}) ds_{ci} ds_{si} . \qquad \text{(H-7)}$$

If s_{ci} and s_{si} are assumed to have equal variances and a zero covariance the test statistic is now written as

$$t_{Lo}(\underline{r}) = \sum_{i=1}^{N} \sigma_i^2 g_i(r_i) \qquad \text{(H-8)}$$

where

$$g(r) = \frac{f''(r)}{f(r)} + \frac{f'(r)}{rf(r)} . \qquad \text{(H-9)}$$

If the unknown signal components are assumed to have equal variances from sample to sample then an equivalent test statistic is

$$t'_{Lo}(\underline{r}) = \sum_{i=1}^{N} g(r_i). \qquad \text{(H-10)}$$

LIST OF REFERENCES

1. Cummins, E.J., Jauregui, S., and Vincent, W.R., "Time- and Frequency-Domain Characteristics of Man-Made Radio Noise Affecting HF-Communications Sites," IEEE Trans. on EMC, v. EMC-21, pp. 182-189, August 1979.

2. Herman, J.R., "Survey of Man-Made Radio Noise," Progress in Radio Science, International Union of Radio Scientists, Brussels, Belgium, pp. 315-408, 1970.

3. Stanford Electronics Laboratories Technical Report No. 7050-7H, A New Model for Impulsive Phenomena: Application to Atmospheric-Noise Communication Channels, by H.M. Hall, August 1966.

4. De Reffye, J., General Modelization of Impulsive Noise, Inter. Conf. on Commun., 1982, v. 1. pp. 2H.3/1-5, June 1982.

5. Modestino, J.W., Jung, K.Y. and Matis, K.R., Modeling, Analysis and Simulation of Receiver Performance in Impulsive Noise, GLOBECOM 1983, v. 3, pp. 1598-1605, December 1983.

6. Urkowitz, H., Signal Theory and Random Processes, Artech House, 1983.

7. Brigham, E.O., The Fast Fourier Transform, Prentice-Hall, Inc., p. 230, 1974.

8. Kailath, T., "The Complex Envelope of White Noise," IEEE Trans. on Inf. Theory, v. IT-12, pp. 397-398, July 1966.

9. DiFranco, J.V. and Rubin, W.L., Radar Detection, Prentice-Hall, Inc., 1968.

10. Beckmann, P, "Amplitude Distribution of Atmospheric Radio Noise," Radio Science, v. 68D, p. 726, June 1964.

11. Electric Power Research Institute Report EL/EM -4290, v. 1, Harmonics and Electrical Noise in Distribution Systems, by W.R. Vincent, April 1985.

12. Myers, H.A., "Industrial Equipment Spectrum Signatures," IEEE Trans. on RFI, v. RFI-5, pp. 30-42, March 1963.

13. Crichlow, W. Q., and others, "Determination of the Amplitude-Probability Distribution of Atmospheric Radio Noise From Statistical Moments," J. of Res. of NBS, v. 61D, January-February 1960.

14. Likhter, J. I., "Some Statistical Properties of Atmospherics," Radiotekh i Electron, v. 1, pp. 1295-1302, 1956.

15. Ibukan, O., "Structural Aspects of Atmospheric Radio Noise in the Tropics," Proc. IEEE, v. 54, pp. 361-367, March 1966.

16. Spaulding, A. D., Roubique, C. J., and Crichlow, W.Q., "Conversion of the Amplitude-Probability Distribution Function for Atmospheric Radio Noise from One Bandwidth to Another," J. of Res. of NBS, v. 66D, pp. 713-720, November-December 1962.

17. Horner, F. and Harwood, J., "Investigation of Atmospheric Radio Noise at Very Low Frequencies," Proc. IRE, v. 103, pt B, pp. 743-751, November 1956.

18. Schonhoff, T.A., Giordano, A.A., and Huntoon, Z., Analytical Representation of Atmospheric Noise Distribution Constrained in V_a, Inter. Conf. on Commun., Chicago, Illinois, June 1977.

19. Katz, A.H., Meltz, G., Mullen, J.A., "Probability Density Distribution of Wideband 2-6 MHz Terrestrial Radio Noise," IEEE Trans. on Antennas and Propag., v. AP-27, pp. 107-111, January 1979.

20. Lord, R.D., "The use of the Hankel Transform in Statistics," Biometrika, v. 41, pp. 44-55, 1954.

21. Modestino, J.W., and Ningo, A.Y., "Detection of Weak Signals in Narrowband Non-Gaussian Noise," IEEE Trans. on Inf. Theory, v. IT-25, pp. 592-600, September 1979.

22. Furutsu, K. and Ishida, T. "On the Theory of Amplitude Distribution of Impulsive Random Noise," J. Appl. Phys. (Japan), v. 23, pp. 1206-1221, July 1960.

23. Giordano, A.A. and Haber, F., "Modeling of Atmospheric Noise", Radio Science, v. 7, pp. 1011-1023, November 1972.

24. Middleton, D., "Statistical-Physical Models of Electromagnetic Interference," IEEE Trans. on EMC, v. EMC-19, pp. 106-127, August 1977.

25. C.C.I.R. Report 322, World Distribution and Characteristics of Atmospheric Radio Noise, I.T.U. Geneva, 1964.

26. Huntoon, Z.M. and Giordano, A.A., Energy Detection in Impulsive Noise, Inter. Conf. on Commun., pp. 07.1/1-4, June 1979.

27. Herman, J.R., and others, "Measurement and Statistical Analysis of Wideband MF Atmospheric Radio Noise," Radio Science, v. 21, pp. 25-46, January-February 1986.

28. Skomal, E.N., Man-Made Radio Noise, Van Nostrand Reinhold Company, NY, 1978.

29. Pakala, W.E. and Chartier, V.L., "Radio Wave Measurements on Overhead Power Lines from 2.5 to 800 kV," IEEE Trans. on Power Apparatus and Systems, v. PAS-90, p. 1155, May-June 1971.

30. IBM Technical Report RC-2878, Asymptotic Properties of Branching Renewal Processes, by P.A.W. Lewis, pp. 2-5, May 1970.

31. Moose, P.M., and O'Dwyer, J.M., "A Model for Impulsive Power Line Radio Interference due to Gap Type Discharges," IEEE Trans. on EMC, to appear November, 1986.

32. Cox, D.R., Renewal Theory, Metheun and Co. Ltd., 1962.

33. Larson, H.J., Introduction to Probability Theory and Statistical Inference, John Wiley, Inc., 1974.

34. Arai, K., Janischewskyj, W. and Miguchi, N., "Micro-gap Discharge Phenomena and Television Interference," IEEE Trans. on Power Apparatus and Systems, v. PAS-104, No. 1, pp. 224-224, January 1985.

35. Ross, S.M., Introduction to Probability Models, Academic Press, Inc., p. 448, 1985.

36. Timperley, J.E., "Incipient Fault Identification through Neutral RF Monitoring of Large Rotating Machines," IEEE Trans. on Power Apparatus and Systems, v. PAS 102, March 1983.

37. Loeb, L.B., Electrical Coronas, University of California Press, p. 572, 1965.

38. Olsen, R.G., "Radio Noise Fields Generated by Corona Streamers on a Power Line," Radio Science, v. 18, pp. 399-408, May-June 1983.

39. Weiss, G., "Shot Noise Models for the Generation of Synthetic Streamflow Data," Water Resources Research, v. 13, pp. 101-108, February 1977.

40. Gardner, W.A. and Franks, L.E., "Characterization of Cyclostationary Random Signal Processes," IEEE Trans. on Inf. Theory, v. IT-21, pp. 4-14, January 1975.

41. Papoulis, A., Probability, Random Variables and Stochastic Processes, McGraw-Hill, Inc., 1985.

42. Urkowitz, H. "Energy Detection of Unknown Deterministic Signals," Proc. of IEEE, v. 55, April 1967.

43. Cook, C.E., and Bernfeld, M., Radar Signals, An Introduction to Theory and Applications, Academic Press, p. 164, 1967.

44. Williams, J.R. and Ricker, G.G., "Signal Detectability Performance of Optimum Fourier Receivers," IEEE Trans. on Audio and Electroacoustics, v. AU-20, October 1972.

45. Abramowitz, M., and Stegun, I., Handbook of Mathematical Functions, US Government Printing Office, Washington, DC, 1964.

46. Miller, J.H., and Thomas, J.B., "Detectors for Discrete-Time Signals in Non-Gaussian Noise," IEEE Trans. on Inf. Theory, v. IT-18, pp. 241-250, March 1972.

47. Rudnick, P., "Likelihood Detection of Small Signals in Stationary Noise," J. Appl. Phys., v. 32 pp. 140-143, February 1961.

48. Capon, J. "On the Asymptotic Efficiency of Locally-Optimum Detectors," IRE Trans. on Inf. Theory, v. IT-7, pp. 67-71, April 1961.

49. Evans, J.E. and Griffiths, A.S., "Design of a Sanguine Noise Process Based Upon World-Wide Extremely Low Frequency (ELF) Recordings," IEEE Trans. on Commun., v. COM-22, pp. 528-539, April 1974.

50. Dillard, G.M., "Mean-Level Detection of Non-Fluctuating Signals," IEEE Trans. on Aero. and Elec. Sys., v. AES-10, pp. 795-799, November 1974.

51. Wozencraft, J.M. and Jacobs, I.R., Principles of Communication Engineering, John Wiley, Inc., p. 459, 1965.

52. SRI Technical Memorandum 3564-061583, Description of Instrumentation, by W.R. Vincent, pp. 2-5, June 1983.

53. Papoulis, A., Systems and Transforms with Applications in Optics, p. 143, McGraw-Hill, Inc., 1968.

54. Gradshteyn, I.S. and Ryzhik, I.M., Tables of Integrals, Series and Products, Academic Press, 1965.

55. Cox, D.R. and Miller, H.D., The Theory of Stochastic Processes, John Wiley, Inc., p. 359, 1965.

56. Poor, H.V., and Thomas, J.B. "Locally Optimum Detection of Discrete-Time Stochastic Signals in Non-Gaussian Noise," J. Acoust. Soc. Am., v. 63, pp. 75-80., January 1978.

INITIAL DISTRIBUTION LIST

		No. Copies
1.	Defense Technical Information Center Cameron Station Alexandria, VA 22304-6145	2
2.	Superintendent Attn: Library, Code 1412 Naval Postgraduate School Monterey, CA 93943-5000	2
3.	Department Chairman, Code 62 Department of Electrical and Computer Engineering Naval Postgraduate School Monterey, CA 93943	1
4.	Professor Stephen Jauregui, Code 62Ja Department of Electrical and Computer Engineering Naval Postgraduate School Monterey, CA 93943	10
5.	Commander Naval Space and Warfare Command Naval Space and Warfare Command Headquarters (Attn: Code PDW-107-6F) Washington, DC 20360	50
6.	Commander Naval Space and Warfare Command Naval Space and Warfare Command Headquarters (Attn: Code PDW-107-9) Washington, DC 20360	1
7.	Commander Naval Security Group Command Naval Security Group Command Headquarters 3801 Nebraska Avenue, NW (Attn: Code G81) Washington, DC 20390	2

8. Commander 1
Naval Security Group Command
Naval Security Group Command Headquarters
3801 Nebraska Avenue, NW
(Attn: Code G82)
Washington, DC 20390

9. Professor W. Ray Vincent, Code 62Ja 2
Department of Electrical and Computer
Engineering
Naval Postgraduate School
Monterey, CA 93943

10. Director, Research Administration 1
Code 012
Naval Postgraduate School
Monterey, California 93943-5000

END

1-87

DTIC